Advancing the Capabilities of Numerical Weather Prediction - On the Utility of Individual Tendency Output

Marvin Kähnert

Thesis for the degree of Philosophiae Doctor (PhD)
University of Bergen, Norway
2022

UNIVERSITY OF BERGEN

Advancing the Capabilities of Numerical Weather Prediction - On the Utility of Individual Tendency Output

Marvin Kähnert

Thesis for the degree of Philosophiae Doctor (PhD)
at the University of Bergen

Date of defense: 18.11.2022

Year: 2022

Title: Advancing the Capabilities of Numerical Weather Prediction - On the Utility of Individual Tendency Output

Name: Marvin Kähnert

Print: Skipnes Kommunikasjon / University of Bergen

Scientific environment

This study has been carried out at the Geophysical Institute, University of Bergen and the Bjerknes Centre for Climate Research in collaboration with the Norwegian Meteorological Institute. The work has been supported by the Research Council of Norway through the ALERTNESS project (grant no. 280573). I have been enrolled in the Research School on Changing Climates in the Coupled Earth System (CHESS).

UNIVERSITY OF BERGEN

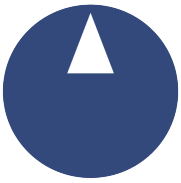

Alertness

Norwegian
Meteorological
Institute

Research school on changing climates in the coupled earth system

Acknowledgements

First and foremost, I want to sincerely thank my supervisor Harald Sodemann for the continued support and vivid discussions during these four years. Thank you for encouraging me to work freely and discover the vast topic that is atmospheric modelling, yet always nudging me back on track when needed. Thank you as well for giving me the possibility to design parts of the modelling course we taught together, which was an elevating experience all-around. Thanks especially for providing me with the possibility to be a part of two fantastic field campaigns.

Thanks to Marius Jonasson for spontaneous, yet long discussions about the status and problems of my work and for providing me with the opportunity to teach at UNIS.

I am deeply thankful to Teresa Remes for the profound help she offered me by sharing her vast experience in working with AROME-Arctic, introducing me to the HARMONIE-AROME community, and discussing ideas and results.

I thoroughly thank Igor Esau, for sharing his deep theoretical wisdom about the stable boundary layer, substantially sharpening the focus of my work. In the same manner, I wish to thank Wim de Rooy, for providing excellent guidance on the treatment of convection in the model.

Many thanks to Stephen Outten for the extensive coding sessions, discussions about scientific work ethic, and numerous gaming nights. Similarly, I would like to thank Aria Outten for the overwhelming hospitality, making these nights all the more greater.

A lot of thanks to Juraj Pálenik for fantastic sailing trips, outstanding galley food, elevating scientific discussions, and spontaneous help with coding.

Furthermore, I am very thankful to Jenny Sjåstad Hagen and Benhood Fathi for introducing and welcoming us to the Norwegian culture (with a touch of Persia), organising spectacular 17th May celebrations, founding our band *The Piggschweins*, and engaging in vivid evening discussions.

Thanks also to my colleagues and office mates Aina Johannessen, Iris Thurnherr, Alena Dekhtyareva, Andrew Seidl, Mika Lanzky, Matilda Hallerstig, and Alexandra Touzeau, for a vibrant atmosphere at the office, feedbacks on drafts and figures, and the uplifting team-work experience during the field campaigns.

I wish to thank Inger-Lise Frogner, Yurii Batrak, Eivind Støylen, Máté Mile, Åsmund Bakketun, Rafale Grote, Andrew Singleton, Jenny Engdahl, Morten Køltzow, Mariken Homleid and Ole Vignes for helping with coding and sharing model scripts and data.

I would also like to thank Sebastian Schiller, Melanie Fugger, Maximilian Schaper, Kathi van de Sand, Maximilian Strunk, Malte Stern, Mark Schindler, and Simon Barthel for numerous online sessions that made the lock-down periods thoroughly more enjoyable.

I am deeply grateful to my parents for supporting and encouraging me in all of my decisions, which eventually led to this thesis. Thank you for always providing guidance, help, and reality-checks, whenever I needed them most.

Finally, thank you Chrissi for moving with me to Norway. Thank you for your unlimited kindness and support during this PhD journey, which became immeasurably important during the lock-down.

"See first, think later, then test. But always see first. Otherwise you will only see what you were expecting."

Douglas Adams, The Hitchhiker's Guide To the Galaxy

Abstract

Parameterisation schemes in numerical weather prediction (NWP) models represent the effects of subgrid-scale processes on the resolved grid. These processes include turbulence, radiation, or droplet formation in clouds. Every parameterisation scheme describes a simplified version of the represented natural process and thereby introduces uncertainty into our models. Driven by the need to provide the most accurate prediction, operational weather centres often adjust parameters associated with parameterisation schemes, sometimes putting them outside the limits implied by theory or observations. Despite the unquestionable success of weather forecasts, this procedure hampers model development and creates the impression of a black box. This thesis explores and disentangles the physical representation of atmospheric processes in the operational NWP model AROME-Arctic, employed by the Norwegian Meteorological Institute for the European Arctic. The central diagnostic of this thesis is the individual tendency output, which provides the contributions of every parameterisation scheme to the prognostic model variables throughout the model integration. The analysis of this output allows to decipher the interplay between different parameterisation schemes and to study the subgrid-scale adaption of the model to changes in the model formulations.

The first paper studies the representation of a marine cold-air outbreak over the Nordic seas. The study reveals the importance of model-internal boundary-layer types for the individual contributions and interplay of different parameterisation schemes. Furthermore, the study demonstrates a pronounced compensation between the individual tendencies from several parameterisations. Sensitivity experiments, including an increase and decrease of parameterised shallow convection, show that this compensation adapts to altered model formulations and can yield unchanged grid scale variables, despite differences in individual tendencies by up to an order of magnitude.

The second paper investigates the representation of the stable boundary layer over snow-covered surfaces. Hereby, the analysis differentiates between two stability regimes: the weakly-stable boundary layer (wSBL) and the very-stable boundary layer (vSBL). The study reveals that both stability regimes occur on small spatial scales of about 5 km in AROME-Arctic. Furthermore, the model captures the different feedback mechanisms between enhanced stratification and turbulent mixing associated with the two regimes. A sophisticated update to the surface scheme, which allows for faster surface cooling, strongly impacts parameterised processes but only changes grid-scale temperatures in the vSBL. In the wSBL, the efficient heat transport by turbulence compensates the enhanced cooling at the surface.

The third paper probes the role of surface-atmosphere coupling and vertical resolution for the representation of the stable boundary layer in AROME-Arctic. The focus is on the long-standing issues of the near-surface warm bias and weak temperature gradients in Arctic forecast products. Again, the study differentiates between the wSBL and vSBL. Operationally, the model enforces neutral stratification in the surface layer, leading to a continuous coupling between the lowermost model level and the surface. By allowing for a stably stratified surface layer, the surface can decouple from the atmosphere in the vSBL. This decoupling results in colder surface temperatures but warmer atmospheric

temperatures and weaker temperature gradients and resembles a runaway cooling effect. Increasing the vertical resolution results in steeper temperature gradients but nearly unchanged surface temperatures as a similarly deep layer remains coupled to the surface.

Abstrakt

Parametrisering i numeriske værmodeller representerer finskalaprosesser i atmosfæren på subgridnivå. Disse atmosfæriske prosessene inkluderer turbulens, stråling og dråpeformasjon i skyer. Enhver parametrisering er en forenkling av den fysiske prosessen den representerer; følgelig leder parametrisering til usikkerhet i modellene. For å få mest mulig nøyaktige værforutsigelser med operasjonelle værmodeller, justeres parameterne i parametriseringene noen ganger slik at enkelte parameterverdier havner utenfor teoretiske grenser basert på observasjoner. Til tross for den åpenbare nytten av nøyaktige værforutsigelser, fører slik bruk av parametrisering til at numeriske værmodeller får elementer av "svart boks"- modellstruktur. Denne avhandlingen utforsker representasjonen av atmosfæriske prosesser i den operasjonelle værmodellen AROME-Arctic – utviklet av Metrologisk Institutt for arktiske områder i Europa – med søkelys på sentralitetsmål som viser de ulike bidragene fra hver parametrisering til de prognostiske variablene i modellen. Analyser av slike sentralitetsmål gjør det mulig å studere interaksjonene mellom ulike parametriseringer og synliggjøre tilpasninger i finskalaprosesser på subgridnivå.

Den første artikkelen i denne avhandlingen omhandler representasjonen av et marint kalduftsutbrudd over de nordiske hav. Studien belyser effekten av ulike typer planetære grenselag på de individuelle bidragene fra de ulike parametriseringene i modellstrukturen. Studien viser også at flere parametriseringer kompenserer hverandre. Sensitivitetsanalyser viser at denne kompensasjonen kan forhindre endringer i gridskalavariabler til tross for svært forskjellige individuelle effekter.

Den andre artikkelen i denne avhandlingen omhandler representasjonen av stabile planetære grenselag over snødekte områder. I denne artikkelen skilles det mellom svakt stabile grenselag og svært stabile greneslag. Studien viser at både svakt stabile og sterkt stabile planetære grenselag forekommer på størrelsesordenen 5 km i AROME-Arctic-modellen. Videre vises det at modellen fanger opp ulike tilbakekoplingsmekanismer assosiert med de to typene stabile grenselag. Når kjøleeffekten av overflaten i modellen økes, påvirkes parametriseringene i både svakt stabile og sterkt stabile grenselag, men endringer i gridskalavariabler observeres kun i sistnevnte. Varmetransport gjennom turbulens kompenserer i stor grad for økt kjøling fra overflaten i svakt stabile grenselag.

Den tredje artikkelen i denne avhandlingen setter søkelys på koplingen mellom overflaten og atmosfæren samt den vertikale oppløsingen i stabile planetære grenselag i AROME-Arctic-modellen, nærmere bestemt systematiske feil (bias) i både temperaturgradienten og temperaturen nær overflaten i arktiske strøk. I denne artikkelen skilles det også mellom svakt stabile og sterkt stabile grenselag. En håndheves, nøytral stratifisering i overflatelag under operasjonell værvarsling fører til kontinuerlig kopling mellom det laveste modellaget og overflaten. Ved å tillate et stabilt stratifisert overflatelag, kan overflaten frakoples atmosfæren under sterkt stabile grenselag. Dette fører til kaldere overflatetemperaturer, men varmere atmosfæriske temperaturer og svakere temperaturgradienter. Denne prosessen likner en positiv tilbakemelding ("runaway cooling"). Ved

å øke den vertikale oppløsningen, øker også temperaturgradientene, mens overflatetemperaturen forblir tilnærmet slik som ved et tilsvarende dypt lag tilkoplet overflaten.

List of Papers

This thesis consists of an introductory part and three scientific papers. Chapter 1 introduces and outlines the work that is presented. A detailed description of the AROME-Arctic numerical weather prediction model is given in Chapter 2. Chapter 3 introduces the core diagnostic used in this work, called the individual tendency output, followed by a description of its usage in Chapter 4. A brief summary of the papers is given in Chapter 5, with a discussion and outlook following in Chapter 6. The papers included in this thesis (Chapter 7) are:

1. Marvin Kähnert, Harald Sodemann, Wim C. de Rooy, and Teresa M. Valkonen (2021) *On the Utility of Individual Tendency Output: Revealing Interactions between Parameterized Processes during a Marine Cold Air Outbreak*, Weather and Forecasting, **36(6):1985 – 2000**, https://doi.org/10.1175/WAF-D-21-0014.1

2. Marvin Kähnert, Harald Sodemann, Teresa M. Remes, Carl Fortelius, Eric Bazile, and Igor Esau (under review in Boundary-Layer Meteorology), *Spatial variability of nocturnal stability regimes in an operational weather prediction model*

3. Marvin Kähnert, Harald Sodemann, Teresa M. Remes, Carl Fortelius, Mariken Homleid, (in preparation) *Probing the stable boundary layer in an operational weather prediction model: Impacts of surface coupling and vertical resolution*, in preparation

Contents

1 Introduction

There exists little doubt that the detailed representation of the Earth's atmosphere, ocean, and land in the form of numerical models is one of the defining milestones of atmospheric sciences within the last century. Over the last 30 years, these models have demonstrated an impressive, perpetual increase in forecast skill as a result of continued development, also famously titled "the quiet revolution of numerical weather prediction" (*Bauer et al.*, 2015). Especially the daily weather forecast, a product of these models, has since become ever-present, influencing the day-to-day decision making of many people.

Forecasts from numerical weather prediction (NWP) models advice citizens about the risk of rainfall, icy roads, or gustiness, and play an integral role for the security of remote settlements, shippings, aviation, or offshore operations. One region that experiences a continued increase of all of these endeavors is the Arctic. Connected to the socio-economic opportunities that come with the retreat of sea-ice, the Arctic regions see rapid developments in urbanization, exploration, transportation, and tourism (*Karlsdottir et al.*, 2011; *Emmerson and Lahn*, 2012). All of these endeavors rely on accurate and tailored weather forecast products to be available.

Yet, our NWP models are still uncertain due to a variety of reasons. Leading causes are the chaotic nature of our atmosphere (*Lorenz*, 1963; *Palmer et al.*, 2005), the sparseness of high-quality observations (*Casati et al.*, 2017), and the representation of small-scale processes by simplified formulations, so called parameterisation schemes (e.g. *Palmer*, 2001; *Stensrud*, 2007). Especially in the Arctic, the availability of high-quality observations is scarce and atmospheric phenomena often exhibit small spatial extents, making them more dependable on parameterisation schemes. Consequently, NWP models suffer from poor accuracy in the Arctic compared to the mid-latitudes (*Jung et al.*, 2016). Some deficits in Arctic weather forecasts can even be traced back to the limitations of individual schemes (*Vihma et al.*, 2014). Thus, it stands to reason that an improvement of the parameterisation schemes goes hand in hand with improved NWP model performance.

Unfortunately, experiences from weather prediction centres often document the opposite (*Sandu et al.*, 2013). Likely culprits for that are model tuning and error compensation. In short, every single component of our models introduces uncertainty into the forecast, whereby parameterisation schemes are a prime example. Yet, the foremost task of an operational NWP model is to deliver a reliable estimate of the future state of the atmosphere. To achieve such an estimate, the internal formulations of the model are 'tweaked', which is called model tuning (*Mauritsen et al.*, 2012). We can think of the model as a clockwork, whereby individual gears represent the different model components. By design, each gear is malfunctioning slightly in some form or another. To still get the correct time (a good forecast), we need to modify the gears (tuning) by e.g. bending them a bit, removing some teeth at one place, and adding some at another place. Thereby, we eventually modify the original function of the gear in the entire clockwork. If we now want to replace one of these modified gears with a new and supposedly better one, we run into the problem that our new gear (new scheme) will not properly fit into the clockwork's work flow as a whole. To improve this procedure we first need to get

an idea about the role that each gear plays in our clockwork. In the model world, this translates to deciphering the specific role that each individual parameterisation scheme plays in our NWP model. This is the focus of my work.

Embedded within the ALERTNESS[1]-project, my work aims at improving numerical weather prediction for high-latitude regions. As the methodological basis, I use AROME[2]-Arctic, the operational weather prediction model employed by the Norwegian Meteorological Institute. Specifically, I focus on the representation of physical processes by the model's parameterisation schemes. In order to investigate these representations, I implemented the output of individual tendencies into AROME-Arctic, which subsequently forms the key diagnostic of my work. A tendency refers to the temporal change of a modeled variable due to e.g. a physical parameterisation scheme. Even though these tendencies have always been an intrinsic part of our model formulations, they are often overlooked by the community (*Lackmann and Thompson*, 2019). This work demonstrates the utility of individual tendencies for the analysis, improvement, and continued development of NWP models and advocates for a more widespread output and usage of these model fields.

1.1 Parameterisation schemes and the scope of this study

Historically, parameterisation schemes have always been an inherent part of NWP models. Following the pioneering work of *Abbe* (1901), *Bjerknes* (1904), and *Richardson* (1922), a weather forecast can be treated as an initial value problem. Starting from a precise estimate of the current state of the atmosphere, its evolution is yielded by integrating the seven primitive equations, including the three hydrodynamic equations of motion, the continuity equation, the ideal gas law, the first law of thermodynamics, and the continuity equation for water species. Yet, there exist no analytical solution for this set of equations and instead numerical methods are needed. These methods require the spatial and temporal discretization of the atmosphere on a model grid, i.e. the representation of atmospheric variables by a set of three-dimensional points. In his remarkable work which introduced many now-familiar concepts of NWP, *Richardson* (1922) used such a discretization to solve the primitive equations by an approximate finite difference method. By discretizing on a grid, Richardson faced the problem of how to treat processes that are not explicitly resolved on the grid, but were already known to have a profound influence on atmospheric flow, such as friction. In fact, *Bjerknes* (1904) was already aware of this problem and proposed to group the to-be-calculated processes into dynamical (large-scale) and physical (small-scale) *problems*, solved respectively by hydrodynamics and thermodynamics.

Richardson, inspired by the work of Osborne Reynolds, decomposed the prognostic variables into a mean and deviation term. The mean was ought to be represented on the grid, while the deviation term represents the impact of a statistical ensemble of sub-grid scale processes on the resolved-scale flow. Bjerknes and Richardson both highlighted that the large difference in spatial scales between the dynamical and physical processes requires the development of empirical formulations that adequately project scientific

[1] Advanced models and weather prediction in the Arctic: Enhanced capacity from observations and polar process representations

[2] Application of Research to Operations at Mesoscale

knowledge, e.g. gained in lab experiments, onto the large-scale flow. Today we call these formulations parameterisation schemes.

Still in today's time, where operational NWP centres employ model grids at kilometre-scale resolution, there exists a multitude of small-scale physical processes that 'fall through the grid' and need to be parameterised (*Stensrud*, 2007). One example is the transfer of radiation through the atmosphere, which strongly modulates the energy balance at the surface and impacts surface temperatures. This process happens on the molecular level, and is not resolved by any atmospheric model. Another example are clouds. Clouds come in various shapes and sizes and are often only a couple of hundred meters across in every direction. Such scales cannot be represented by current NWP models, which employ horizontal resolutions between 10 km to about 2.5 km (Fig. 1.1). If we want our NWP models to know about the *existence* of such clouds and the effects that they can have on the resolved scale variables, we need to represent them by a parameterisation scheme.

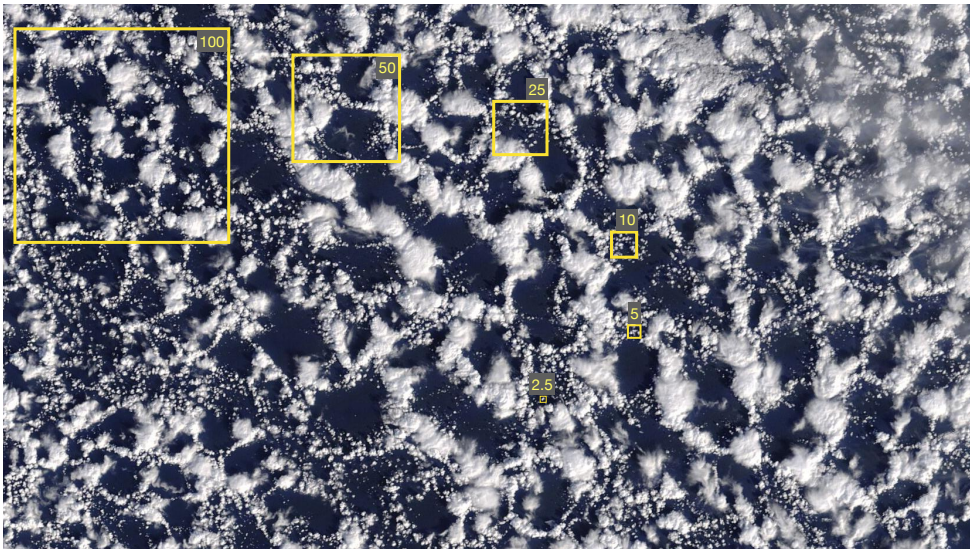

Figure 1.1: Satellite image taken at the 29 March 2022 showing open cellular convection in the Nordic Seas east of Lofoten, Norway. The yellow squares illustrate different model resolutions from 100 km to 2.5 km, commonly used in climate and weather models. Any clouds within the squares would be considered sub-grid scale and require a parameterisation. Adapted from Fig. 1.4 in Stensrud (2007). Imagery taken from the NASA Worldview application (https://worldview.earthdata.nasa.gov), part of the NASA Earth Observing System Data and Information System (EOSDIS).

The essence of a parameterisation scheme is to represent the impact of a small-scale physical process on the resolved scales of a model (*Stensrud*, 2007). The common approach is to use a combination of resolved, grid-scale variables and some adjustable, more or less constrained parameters. These parameters, which give the *parameter*isation its name, are usually derived from field experiments, highly resolved model simulations, or empirical estimates. Despite the steady pursuit towards finer discretization grids and increasingly complex parameterisation schemes, this underlying paradigm remains the

same.

To illustrate the underlying concepts in more detail, let us look at the parameterisation of turbulence, which represents the transport of heat, tracers, and momentum by differently-sized eddies in the atmosphere. One common approach is the so-called K-Theory, depicted here for the vertical turbulent transport of heat (*Stull*, 1988):

$$\overline{w'\theta'} = -K_h \frac{\partial \theta}{\partial z}. \tag{1.1}$$

Here, w denotes vertical wind speed, θ denotes potential temperature, the prime notation refers to the deviation from the mean following Reynolds decomposition, z refers to height, and K_h is called the eddy-diffusivity coefficient.

The left-hand side of Eq. 1.1 describes the mean contribution of small-scale vertical air movements and small-scale temperature variations, in short the vertical transport of heat by turbulence. This term does not disappear when applying the postulates for Reynolds averaging and simultaneously this term cannot be explicitly resolved on the model grid. Thus, it needs to be parameterised, as depicted on the right-hand side of Eq. 1.1. The parameterisation scheme is composed of a grid-scale variable, the vertical gradient of potential temperature $\frac{\partial \theta}{\partial z}$ and the free parameter K_h. While the temperature gradient is known from the model, K_h is not, so we essentially shifted the problem from calculating $\overline{w'\theta'}$ to finding a suitable formulation for K_h.

Evidently, the choice of K_h strongly influences the behavior of the scheme. In case of a positive definite K_h, the equation states that modeled turbulence always acts to reduce the local (vertical) gradient and the magnitude of K_h tells us how fast that reduction will be. Furthermore, K_h needs to be a function of atmospheric stability, as an unstable stratification favors turbulent mixing whereas a stable stratification hinders it. In short, our detailed knowledge about the turbulent exchange of heat in the atmosphere needs to be expressed in *a single value*, that is K_h.

Ideally, a parameterisation scheme is based on physical principles and behaves as nature does (*Mauritsen*, 2007). Both of these ideals can be compromised by factors like the turbulence closure problem (e.g. *Stull*, 1988) or the broad range of situations (night vs day, tropics vs Arctic) that these schemes are used for. Consequently, our parameterisation schemes are uncertain (*Christensen et al.*, 2015) and introduce errors into our NWP models. This has led to the practice of adjusting free parameters such as K_h (Eq. 1.1) in order to maximize the forecast skill of operational NWP models. This adjustment is commonly referred to as model tuning. During this process, the parameters in question can even be put outside the physical range implied by measurements (*Zilitinkevich et al.*, 2013). While indeed improving the forecast skill of NWP models (*Sandu et al.*, 2013), this practice hampers model development. Any new scheme that is based on physical principles might not yield the same 'functionality' as such a tuned scheme and the model performance will most likely decrease. Furthermore, the schemes of a respective model are tuned against each other, which often requires them to be updated in tandem, making stand-alone improvements difficult (*de Rooy et al.*, 2022).

Additionally, many, if not all, weather phenomena are described by a complex interplay between several parameterised and resolved processes. Depending on the phenomena in question, these different processes can interact by partly compensating, complementing or otherwise influencing each other. Such an interplay can lead to so-called

error compensation. When errors compensate, the model arrives at the right conclusion due to the wrong reasons. A systematic overestimation of produced clouds and precipitation in the model could for example be compensated by a systematic underestimation of evaporated water. Such relationships can cause a significant decrease in forecast skill when a new and arguably better parameterisation scheme is introduced to the system (*Sandu et al.*, 2013; *de Rooy et al.*, 2022). Error compensation is difficult to identify in general. However, insight into the model physics can point us to interactions between individual schemes that are especially susceptible or robust towards model changes.

Parameterisations are an inherent part of our NWP models. The analysis of their individual contributions enables the insight into the representation of complex weather phenomena during different atmospheric regimes. The unveiled interactions further help to decipher the model's adaption to e.g. an updated parameterisation scheme and thereby guide model development.

1.2 Investigated atmospheric phenomena

The focus of this work is on phenomena that are long standing issues in high-latitude weather forecasts, namely the convective overturning in marine cold air outbreaks (Paper I) and near-surface temperature developments in the stable boundary layer (Paper II, III). Both phenomena occur frequently in the Arctic and can be hazardous for local communities. A cold-air outbreak can lead to severe icing on ships and aircrafts (*Samuelsen and Graversen*, 2019), and foster the formation of intense mesoscale cyclones, called polar lows (*Kolstad*, 2011). The stable boundary layer can have substantial impacts on air pollution and cause slippery road conditions (*Holtslag et al.*, 2013).

1.2.1 Marine cold-air outbreak

A marine cold-air outbreak (mCAO) is characterized by the advection of cold and dry air over warmer waters. The pronounced contrasts between air-sea temperatures give rise to intense sensible and latent heat fluxes (*Grossman and Betts*, 1990; *Brümmer*, 1996), which in turn transform the formerly cold, dry, and stably stratified air masses into warmer, more humid, and unstable ones. These unstable air masses are associated with vigorous convective mixing and cloud formation (*Etling and Brown*, 1993; *Hartmann et al.*, 1997), that can cause heavy precipitation, especially along coastal regions (Fig. 1.2).

An mCAO is largely influenced by diabatic processes (*Papritz and Pfahl*, 2016; *Papritz and Sodemann*, 2018), that are in turn represented by parameterisation schemes in NWP models. Common model deficits encompass the underrepresentation of supercooled, liquid cloud condensates (*Morrison et al.*, 2012; *Engdahl et al.*, 2020), missed transitions between cloud cover types (*Sandu and Stevens*, 2011), and a misrepresentation of organised, mesoscale convection, often yielding too dense cloud cover or too large convective structures (*Field et al.*, 2017; *Tomassini et al.*, 2017). One of the key problems is the spectrum of convective length scales during an mCAO that ranges from $\mathcal{O}(100\,\mathrm{m})$ to $\mathcal{O}(1\,\mathrm{km})$ (e.g. *Duscha et al.*, 2022). Thereby, the larger convective structures approach the model resolution and it becomes difficult to define a proper partitioning between the amount of resolved and parameterized vertical transport. This partitioning

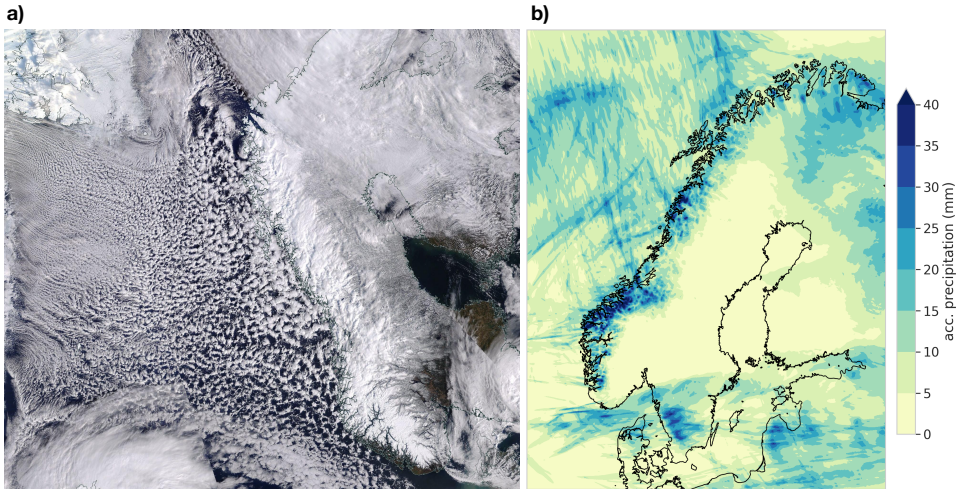

Figure 1.2: a) Satellite from the 13 March 2020 showing mesoscale convection during an mCAO in the Nordic seas. Imagery is taken from the NASA Worldview application (https://worldview.earthdata.nasa.gov). b) Accumulated precipitation during the event in the MetCoOp ensemble prediction system (MEPS, Frogner et al., 2019a).

strongly modulates the development of convection and can lead to considerably different model states (*Honnert et al.*, 2011, Paper I).

1.2.2 Stable boundary layer

The stable boundary layer (SBL) is commonly more shallow compared to its unstable counterpart and is therefore susceptible to shortcomings in parameterisation schemes. These shortcomings encompass ill-representations of surface sensible, radiative, and ground heat fluxes (*Sodemann and Foken*, 2004; *Edwards*, 2009a; *van der Linden et al.*, 2022), crude treatments of surface cover types such as vegetation or snow (*Boone and Etchevers*, 2001; *Boone et al.*, 2017; *Arduini et al.*, 2019), and too vigorous mixing of heat and tracers (*Svensson and Holtslag*, 2009; *Holtslag et al.*, 2013). Modeled representations of the SBL are often too deep, yielding large thermal inertia that prevent efficient cooling of near-surface temperatures (*Esau et al.*, 2018). Consequently, validation studies in high-latitudes document pronounced warm biases in near-surface temperature estimates during stable periods (*Beesley et al.*, 2000; *Haiden et al.*, 2018; *Køltzow et al.*, 2019).

An additional layer of complexity is added by the occurrence of different stability regimes in the form of the weakly-stable boundary layer (wSBL) and the very-stable boundary layer (vSBL, *McNider et al.*, 1995). These two regimes are characterized by different feedbacks between turbulence and radiative surface cooling. In the wSBL, a negative feedback is present, leading to increased turbulent transport as a response to the increased stability due to surface cooling. In the vSBL, a positive feedback is present, leading to a reduction or cessation of turbulence (*Vogelezang and Holtslag*, 1996; *Derbyshire*, 1999). Both regimes exhibit substantially different temperature (Fig. 1.3 a, b) and wind profiles (Fig. 1.3 c, d). The representation of these different stability regimes at the correct time and location can be decisive for meaningful model forecasts.

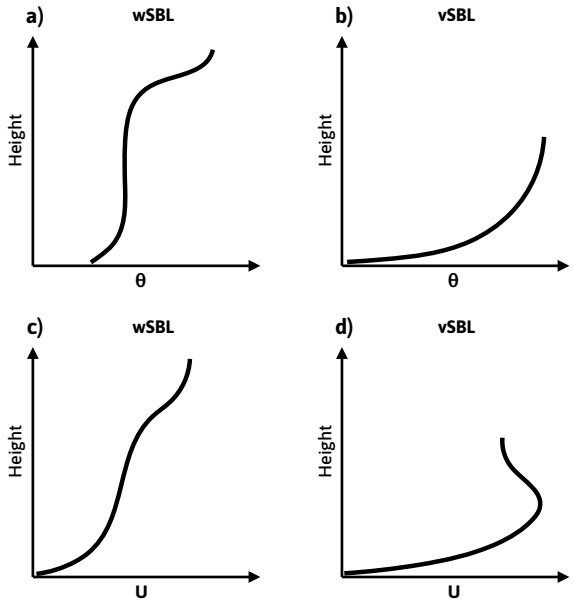

Figure 1.3: Schematic potential temperature profiles for the a) weakly-stable and b) very-stable boundary layer. Schematic wind speed profiles for the c) weakly-stable and d) very-stable boundary layer. In parts adapted from Fig. 1 in Mahrt (2014).

1.3 Objectives and outline

This work demonstrates the utility of individual tendency output (*Niemelä and Fortelius*, 2005; *Savijärvi*, 2006; *Jung et al.*, 2016) for the analysis, verification, and development of NWP models. All conducted studies follow a systematic approach:

1. Investigate the representation of a phenomena (mCAO, SBL) on both the grid and subgrid-scale, utilizing individual tendencies
2. Identify distinct interplays between individual tendencies that require separate analysis (see Chapter 4)
3. Modify and update key physical schemes (sensitivity experiment)
4. Conduct a tailored analysis of the model's adaption to the changes, guided by the factors identified in step 2

In the following chapter, the setup of the AROME-Arctic model is described. Afterwards, the focus is on the individual tendency output and its implementation into the model (Chapter 3), followed by a discussion of factors that elevate the analysis of individual tendencies (Chapter 4). Then, a summary of each Paper is given in Chapter 5, concluded by a discussion and brief outlook in Chapter 6. Finally, the three papers are appended (Chapter 7).

2 The AROME-Arctic model

AROME-Arctic is a regional, convection-permitting forecasting system covering the European Arctic including the northern part of Scandinavia, the Barents sea, and the surrounding islands (Fig. 2.1). AROME-Arctic is based on HARMONIE-AROME, a part of the shared ALADIN[1]-HIRLAM[2] NWP system (*Bengtsson et al.*, 2017). The long-standing idea behind this model consortium is to provide individual members a state-of-the-art weather prediction system that is based on the same model code, yet specifically adheres to regional peculiarities, for example the necessity to represent sea-ice in polar regions (*Müller et al.*, 2017). Thus, even though the results of this thesis focus on AROME-Arctic, the methodological approach is directly applicable to the model configurations operationally used at a total of nine national weather services.

In its current configuration, AROME-Arctic employs a projected grid with 2.5 km horizontal resolution and 65 vertical hybrid sigma-pressure coordinates reaching up to 9 hPa (24 km). Lateral and uppermost boundary conditions are provided by the high-resolution model (HRES) of the European Centre for Medium Range Weather Forecasting (ECMWF) Integrated Forecasting System (IFS) with a horizontal and vertical boundary zone of eight grid points and eight top levels, respectively. Operational forecasts from three and six hours prior to the respective AROME-Arctic run are used as boundary conditions. Upper-air observations from e.g. radiosondes are assimilated into the model via 3DVAR, whereas observed screen level temperature, relative humidity, and snow depth are assimilated by optimal interpolation.

AROME-Arctic employs a wide range of advanced schemes to represent dynamical and physical processes in the atmosphere. All of these processes contribute individually to the evolution of momentum, temperature, and humidity in the model and are described in the following. Hereby, schemes that are of higher importance for the scope of this work, namely the turbulence, shallow convection and surface schemes, are described in more detail.

2.1 Advection and horizontal diffusion

The dynamical core of AROME-Arctic originates from the AROME-France NWP model (*Seity et al.*, 2011), which in turn uses the ALADIN non-hydrostatic dynamical core (*Bénard et al.*, 2010). For the transport on resolved scales, AROME-Arctic employs a semi-Lagrangian (SL), spectral advection scheme paired with a semi-implicit (SI) time discretization, in short a SLSI approach.

The essence of a SL method is the combination of both Eulerian and Lagrangian approaches. An Eulerian advection scheme determines the evolution of environmental variables at a fixed geographical location. A Lagrangian advection scheme, in contrast, determines the evolution of environmental variables while following a fluid parcel. Both approaches come with advantages and disadvantages. An Eulerian scheme is well-suited

[1] Aire Limiteé Adaptation Dynamique Initialisation
[2] High Resolution Limited Area Modelling

for a Cartesian grid, often employed in NWP models, but requires short time steps due to computational stability, which again prolongs computation time (e.g. *Staniforth and Côté*, 1991). A Lagrangian scheme is not constrained by such a short time step, as it is unconditionally stable, but will quickly transform a set of regularly spaced information (grid points) e.g. on a Cartesian grid, to a set of irregularly spaced information, which

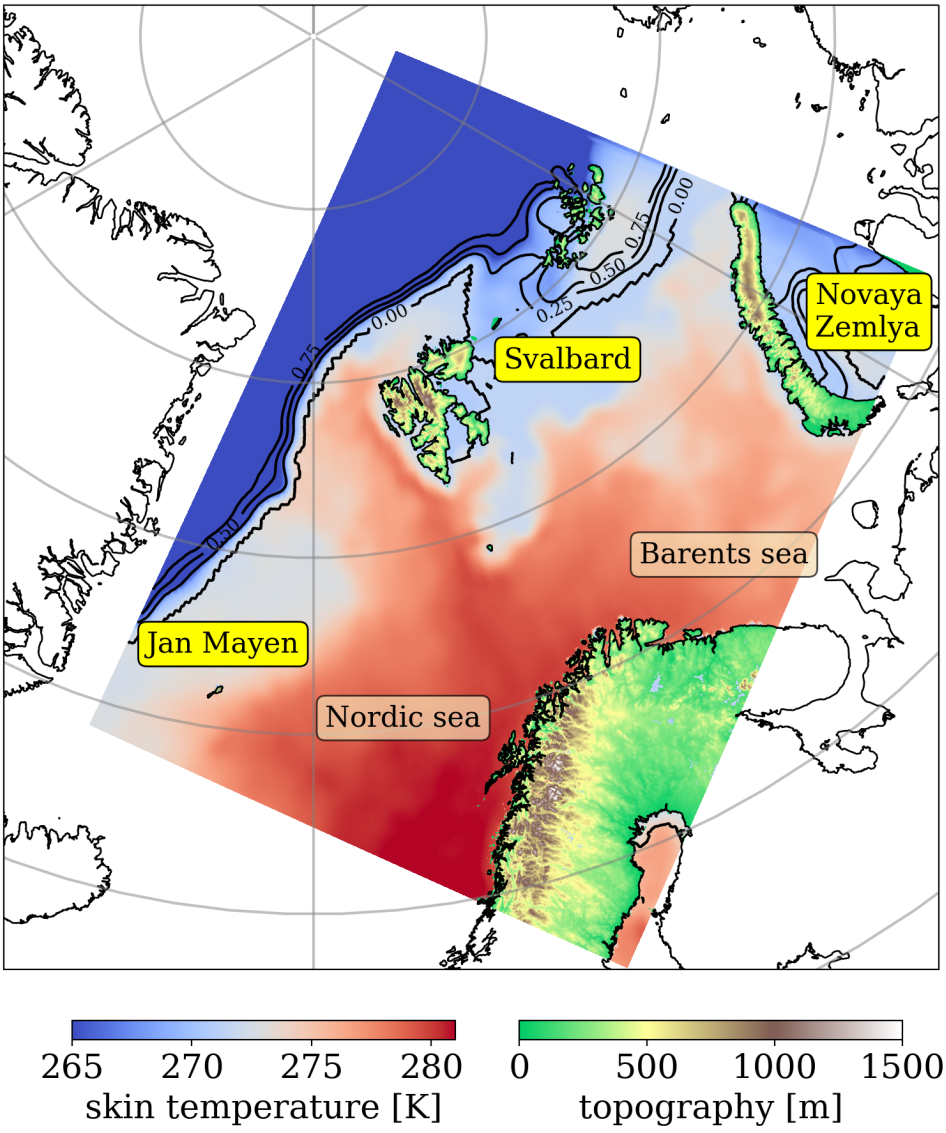

Figure 2.1: The domain of the AROME-Arctic model. The shading over land indicates model topography, and the shading over water indicates skin temperature (K), depicting the situation at 0000 UTC 26 December 2015. The black contours indicate sea ice cover. Adapted from Figure 1 in Paper I.

can lead to strongly reduced accuracy in certain regions of the model domain (*Welander*, 1955).

A SL scheme builds upon the advantages of both approaches. It employs a fixed numerical grid and releases a new set of parcels every model time step at so-called departure points. These points are determined such that the released particles arrive exactly on the regular grid points at the end of the time step (*Staniforth and Côté*, 1991; *Mang and Biros*, 2016). The respective values at the departure points are determined by interpolation, which leads to a certain degree of diffusion done by the SL scheme. This diffusion can be used to account for the effect of horizontal turbulence and molecular dissipation, often not represented by an individual parameterisation scheme in many synoptic-scale NWP models (*Bengtsson et al.*, 2012). Therefore, AROME-Arctic employs a so-called semi-Lagrangian horizontal diffusion scheme (SLHD, *Váňa et al.*, 2008), which locally modulates the 'accurate' SL interpolator I_A by an additional interpolator I_D with specific diffusion properties:

$$I = (1 - \kappa_d) I_A + \kappa_d \, I_D. \tag{2.1}$$

Hereby, I is the final SL interpolator and κ_d can be seen as a diffusion coefficient which is evaluated for every grid point.

The calculations of the dynamical core are performed *after* the calculation of the physical parameterisation schemes (*Seity et al.*, 2011) which has implications for the tendency output (see Chap. 3).

2.2 Microphysics and cloud scheme

The single-moment microphysics scheme (OCND2, *Müller et al.*, 2017) represents the numerous interactions and phase transitions between water vapor and different hydrometeors that occur in the atmosphere. The calculation of OCND2 consist of three parts. First the scheme enforces thermodynamic equilibrium between the microphysical species and the temperature field, called the adjustment step. Then, the scheme calculates six prognostic variables: water vapor, cloud water, rain, ice, snow, and graupel. Finally, a statistical cloud and condensation scheme calculates the three-dimensional cloud fraction (*Bougeault*, 1982; *Bechtold et al.*, 1995). Fig. 2.2 schematically displays the numerous processes between the different hydrometeors considered by OCND2.

2.3 Radiation

Radiation parameterisations provide total radiative fluxes that impact the energy balance at the surface as well as the temperature development at each atmospheric level. A given atmospheric volume, i.e. a model level, for example cools when more energy is radiated out than received. Such cooling is commonly found at cloud tops due to the enhanced emissivity of the water species in the clouds compared to the dry air above. The induced warming or cooling rates are determined by the vertical divergence of radiative fluxes between the model levels:

$$\frac{\partial T}{\partial t}_{rad} = \frac{1}{\rho \, c_p} \frac{\partial}{\partial z} (F^+ - F^-), \tag{2.2}$$

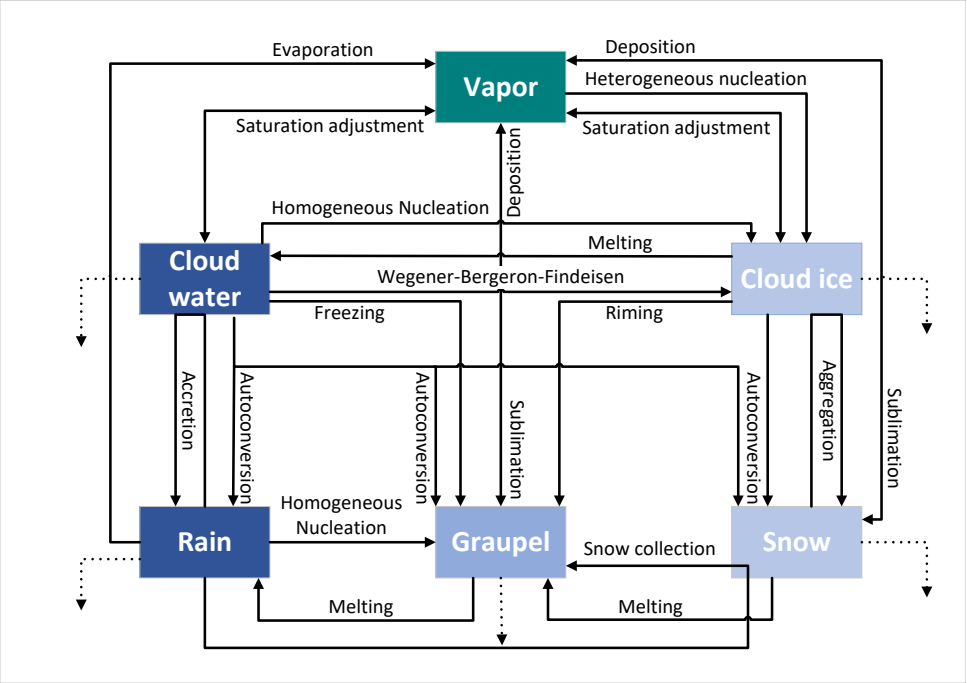

Figure 2.2: Schematic of all processes accounted for by the microphysics scheme in AROME-Arctic. Terminology: Accretion — collection of cloud water by rain droplets; Wegener-Bergeron-Findeisen process — ice grows at the cost of liquid water due to lower saturation pressure over ice; Autoconversion — cloud drops collide and coalesce into drizzle / rain (similar for ice phase); Aggregation — clumping together of snow crystals following collisions; Homogeneous nucleation — pure vapor condenses to form droplets / ice; Heterogeneous nucleation — water condenses (ice freezes) onto existing particles of atmospheric aerosol termed cloud condensation nuclei (CCN); Riming — ice particles aggregating liquid water drops. The stippled arrows depict sedimentation. Adapted from Lac et al. (2008).

where ρ represents the density of air, c_p the heat capacity of air, and $\partial(F^+ - F^-)/\partial z$ the divergence of the net upward radiative flux.

In AROME-Arctic, the radiative fluxes F^+ and F^- are calculated by the rapid radiative transfer model (RRTM, *Fouquart and Bonnel*, 1980; *Mlawer et al.*, 1997). Hereby, the shortwave spectral region is divided into six spectral bands and the longwave spectral region is divided into 16. The choice of spectral bands is based on their homogeneity of contributing species and radiative transfer properties. In addition, the scheme uses climatological distributions of aerosols and ozone.

2.4 Surface

The task of the surface model is to represent processes such as ground and surface heat fluxes, runoff, or snow coverage. In AROME-Arctic, the surface is represented by a separate model called SURFEX (*Le Moigne*, 2009). At the start of its computation, SURFEX divides each grid box into four tiles: sea, lakes, urban areas, nature. This divi-

sion is based on the ECOCLIMAP-II database (*Faroux et al.*, 2013), and some of these tiles are further divided into different patches. The nature tile, for example, contains two vegetation patches, one for low vegetation such as grass and one for high vegetation such as trees. Each tile or patch is represented by individual parameter settings for e.g. roughness length, runoff, or surface conductivity, but also contains tile-specific formulations such as leaf-area-index in the nature tile or building shapes in the urban tile. After all tile-specific calculations are done, the resulting fluxes are summed and weighted by the respective tile fractions of the grid box.

In the following, an excerpt of the calculations in SURFEX is given that deal with the estimation of surface heat fluxes, albedo, and surface temperature. These parameters are later on used as input for other parameterisation schemes. For illustration, I focus on a grid box fully covered by the nature tile. Such a tile can contain four different patches or cover types: low vegetation, high vegetation, bare ground, and snow (Fig. 2.3). Hereby, snow is distinct as it can (partly) cover the other patches and thereby change the respective area fractions.

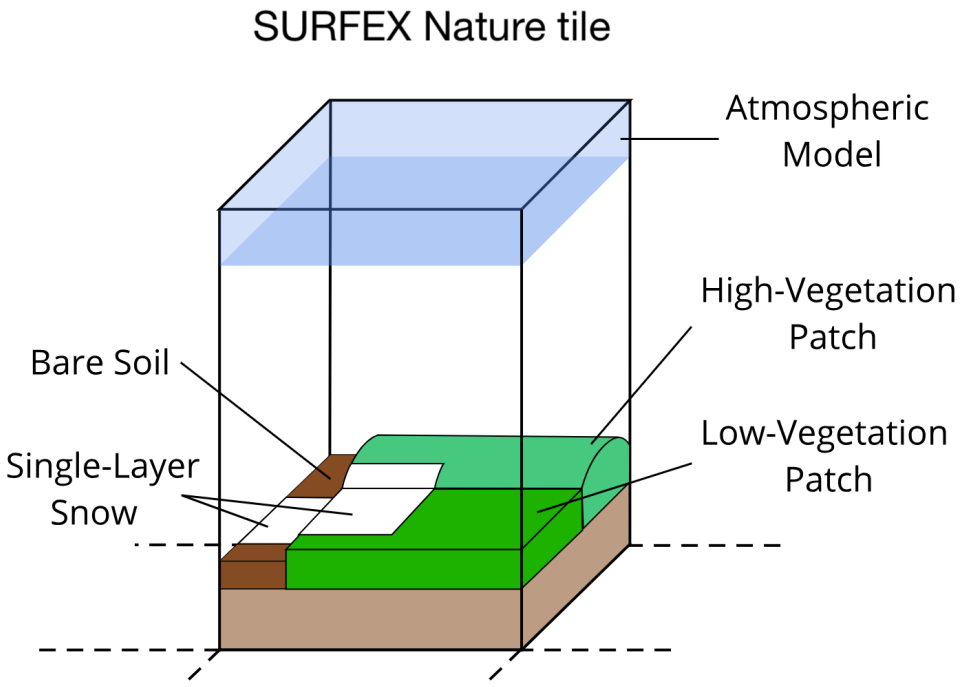

Figure 2.3: Schematic of a nature tile in SURFEX. The elevations of different patches indicate roughness length. Adapted from Figure 1 in Paper II.

Starting with the estimation of snow cover and snow properties, AROME-Arctic employs a single-layer snow scheme (*Douville et al.*, 1995a,b). The total snow cover P_{sc} is computed as a sum of the snow cover fraction over bare ground P_{scg} and the snow cover fraction over the present vegetation P_{scv}, weighted by the vegetation fraction veg:

$$P_{sc} = (1 - \text{veg})\, P_{scg} + \text{veg}\, P_{scv}. \tag{2.3}$$

Over bare ground, the snow cover fraction depends on the snow water equivalent of the snow W_s and an empirical critical value $W_{crit} = 10\,\mathrm{kg\,m^{-2}}$:

$$P_{scg} = \frac{W_s}{W_s + W_{crit}}. \tag{2.4}$$

Over vegetation, the snow cover fraction is a function of snow depth h_s and surface roughness z_0:

$$P_{scv} = \frac{h_s}{h_s + c_{sv}\, z_0} \tag{2.5}$$

whereby $c_{sv} = 5$ is an empirical parameter.

The total snow coverage (Eq. 2.3) modifies the albedo of the surface and with it the radiative balance. Therefore, P_{sc} is subsequently used for estimating the average albedo α_t and emissivity ϵ_t of the grid box:

$$\alpha_t = (1 - P_{sc})\,\alpha + P_{sc}\,\alpha_s, \tag{2.6}$$

$$\epsilon_t = (1 - P_{sc})\,\epsilon + P_{sc}\,\epsilon_s. \tag{2.7}$$

The subscript s refers to the properties of snow. Currently, $\epsilon_s = 1$, whereas α_s is treated as a prognostic variable. In the presence of snow melt and no snow fall, α_s decreases exponentially with time, otherwise the decrease is linear (*Le Moigne*, 2009).

Both α_t and ϵ_t are subsequently used for calculating the net radiation F at the surface:

$$F = F_s\,(1 - \alpha_t) + \epsilon_t\,(F_a - \sigma\,T_s^4) \tag{2.8}$$

where σ is the Stefan-Boltzmann constant, T_s is surface temperature, and F_a and F_s are atmospheric and surface radiative fluxes provided by the radiation scheme (Sect. 2.3).

As evident from Eq. 2.8, a calculation for the surface temperature is required. The prognostic equations for T_s are obtained from a force-restore approach following *Noilhan and Planton* (1989):

$$\frac{\partial T_s}{\partial t} = C_T(F - H - LE) - \frac{2\pi}{\tau}(T_s - T_2) \tag{2.9}$$

$$\frac{\partial T_2}{\partial t} = \frac{1}{\tau}(T_s - T_2) \tag{2.10}$$

where H is the sensible heat flux, LE is the latent heat flux, τ is a relaxation time scale set to one day, and T_2 refers to the mean value of T_s over one day. The parameter C_T depends again on the vegetation and snow cover:

$$C_T = \left[\frac{(1 - \mathrm{veg})(1 - P_{scg})}{C_g} + \frac{\mathrm{veg}\;(1 - P_{scv})}{C_v} + \frac{P_{sc}}{C_s}\right]^{-1} \tag{2.11}$$

where C_g, C_v, and C_s are the heat capacities of the ground, vegetation, and snow respectively.

To close this set of equations, the turbulent fluxes H and LE used in Eq. 2.9 need to be calculated, whereby only the former will be shown in detail here. In both cases, bulk formulas are used which in the case of H yields:

$$H = \rho_a\, c_p\, U_a\, C_H\, (T_s - T_a). \tag{2.12}$$

The subscript a stands for the lowest atmospheric level, U is wind speed and C_H denotes a drag coefficient that depends on the thermal stability of the atmosphere following *Louis* (1979):

$$C_H = C_{DN}\, F_h, \tag{2.13}$$

$$C_{DN} = \frac{\kappa^2}{[ln(z/z_0)]^2}, \tag{2.14}$$

$$F_h = \begin{cases} \left[1 - \dfrac{15\, Ri}{1 + C_h\sqrt{|Ri|}}\right] \times \left[\dfrac{ln(z/z_0)}{ln(z/z_{0h})}\right], & \text{if } Ri \leq 0 \\ \left[\dfrac{1}{1 + 15\, Ri\sqrt{1 + 5\, Ri}}\right] \times \left[\dfrac{ln(z/z_0)}{ln(z/z_{0h})}\right], & \text{if } Ri > 0, \end{cases} \tag{2.15}$$

Here, Ri is the gradient Richardson number in the surface layer, κ is the von Kármán constant, z is height above ground, z_{0h} is the roughness length for heat, and C_h is an empirical parameter depending on C_{DN} and $ln(z/z_{0h})$.

Operationally, AROME-Arctic only uses the first part of Eq. 2.15 due to the setting `XRIMAX=0` (*Donier et al.*, 2012; *Homleid*, 2022). This model parameter sets the maximum Richardson number in the surface layer to 0, implying that calculated surface fluxes during stable stratifications are based on drag coefficients for neutral conditions. The implications and impacts of this settings are evaluated in Paper III.

One should note that SURFEX does not have a direct contribution to the temperature, humidity, or momentum change at any atmospheric level in AROME-Arctic. Instead, the estimated fluxes, emissivities, and roughness lengths are used as input for other parameterisation schemes, first and foremost the radiation and boundary-layer scheme. Consequently, calculations done by SURFEX will not appear as an individual tendency throughout this work.

2.5 Boundary layer turbulence

Lastly, we return to the representation of turbulence in the boundary layer (Sect. 1.1), describing the transport of heat, moisture, momentum, and tracers by differently sized eddies. The defining challenge for such boundary layer schemes lies in the interaction of widely different scales of motion that occur throughout the diurnal cycle. During a sunny, fair-weather day, for example, the vertical extend of turbulent eddies can become as large as the boundary layer (around $\mathcal{O}(1\,\mathrm{km})$), while during stable, nocturnal periods these sizes can shrink considerably ($\mathcal{O}(10\,\mathrm{m})$ to $\mathcal{O}(1\,\mathrm{m})$).

To approach these different scales of motion, the boundary layer scheme in AROME-Arctic adapts its formulation based on model-internal estimates of atmospheric stability, lifting condensation level, and cloud depth. These estimates are grouped into so called *boundary-layer types*. Boundary-layer types (PBL types) play a central role for interpreting the individual tendency output as discussed in detail in Section 4.1.1. However, before introducing the specific changes associated with the PBL types, we first discuss the general treatment of the stable and unstable boundary layer in AROME-Arctic.

2.5.1 The stable PBL

Atmospheric turbulence during stably stratified conditions is represented by the HARATU[3] scheme (*Lenderink and Holtslag*, 2004; *Bengtsson et al.*, 2017). HARATU employs a common eddy-diffusivity approach that follows K-Theory (see Section 1.1):

$$\frac{\partial T}{\partial t}_{turb} = \frac{1}{\rho}\frac{\partial}{\partial z}\left(\rho K_h \frac{\partial \theta}{\partial z}\right). \tag{2.16}$$

To determine K_h, HARATU employs a 1.5 order closure, that combines a prognostic equation for turbulent kinetic energy (TKE, E_k) with a diagnostic length scale l:

$$K_h = \sqrt{E_k} \cdot l. \tag{2.17}$$

The calculation of TKE considers the production due to wind shear and buoyancy, the transport of TKE, and its dissipation (Eq. 2 in *Lenderink and Holtslag*, 2004).

The turbulent length-scale l, which to a large degree determines the amount of mixing done by the scheme, is a function of local stability. Conceptually, l can be understood as the average distance that a parcel moves in the mixing process. For stable conditions, l is expressed as the sum of inverses of a neutral length scale l_n and a stable length scale l_s (*Deardorff*, 1980; *Baas et al.*, 2008):

$$\frac{1}{l} = \frac{1}{l_n} + \frac{1}{l_s} = \frac{1}{c_n \kappa z} + \frac{N}{c_s \sqrt{E_k}}. \tag{2.18}$$

Here, z is height above ground, N is the Brunt–Väisälä frequency, and c_n and c_s are model internal parameters.

On a general note, the turbulence scheme affects atmospheric temperatures by reducing the vertical temperature gradient between adjacent model levels, whereby stability and TKE can affect the amount of mixing. As K_h is positive definite, Eq. 2.16 will always act down the local gradient, omitting any counter-gradient transport. Such behavior can cause problems in the near-neutral to convective boundary layer, where upward heat fluxes can exist despite vanishing or reversed potential temperature gradients (*Deardorff*, 1966). To account for such *counter-gradient* transport, AROME-Arctic adapts its treatment of turbulence in the unstable PBL, described in the following Section.

2.5.2 The unstable PBL

In the unstable PBL, the representation of boundary-layer turbulence experiences two major changes compared to the stable PBL. First, the formulation of the turbulent length-scale l is modified, and secondly the transport due to large eddies is taken into account by the addition of a shallow convection scheme. The shallow convection scheme employs a mass-flux (MF) approach and represents the vertical transport by strong, organized updrafts. Together, the turbulence and shallow convection scheme represent the eddy-diffusivity mass-flux framework (EDMF, *Soares et al.*, 2004; *Siebesma et al.*, 2007) used for the unstable PBL:

$$\overline{w'\theta'} = -K_h \frac{\partial \theta}{\partial z} + M(\theta_u - \overline{\theta}) \tag{2.19}$$

where subscript u denotes properties of the updraft and M denotes the mass-flux.

[3] HARMONIE-AROME with RACMO Turbulence

Turbulent length scale for unstable conditions

The turbulent length-scale l for near-neutral to unstable conditions is now expressed as the sum of inverses of two length scale, l_{up} and l_{dw}:

$$\frac{1}{l} = \frac{1}{l_{up}} + \frac{1}{l_{dw}} \tag{2.20}$$

Hereby, l_{up} and l_{dw} are defined as vertical integrals over stability-dependent functions (*Lenderink and Holtslag*, 2004):

$$\begin{aligned} l_{up} &= \int_{z_{bot}}^{z} F(Ri)\, dz' \\ l_{dw} &= \int_{z}^{z_{top}} F(Ri)\, dz' \end{aligned} \tag{2.21}$$

where $F(Ri)$ describes a function of the local Richardson number, and z_{bot} and z_{top} describe the lower and upper boundaries of the mixing domain, e.g. the surface and the height of a strong, capping inversion, respectively.

By using vertical integrals (Eq. 2.21), both local and non-local atmospheric stability influences the mixing done by the turbulence scheme. The consideration of such non-local properties is important in the convective limit, as considerable mixing is observed in parts of the PBL where near-neutral conditions are present (Fig. 2.4). To fully account for this non-local, advective mixing found in the convective PBL, AROME-Arctic employs a shallow convection scheme.

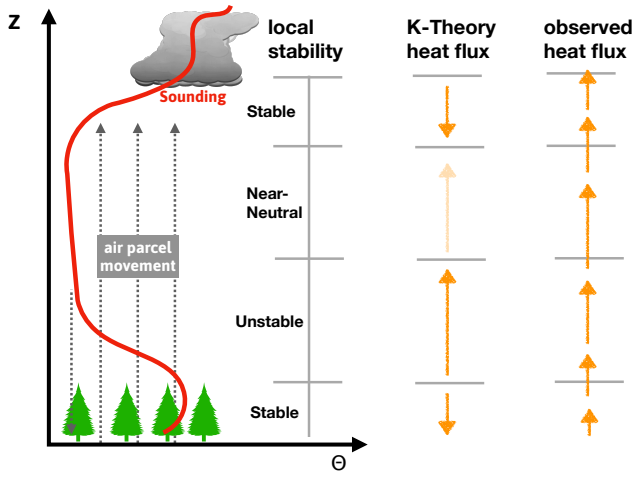

Figure 2.4: Schematic of an unstable boundary layer topped by a cloudy layer. Potential temperature profile is shown in red. Local stability regimes based on the temperature profile are marked by horizontal lines. Orange arrows depict modeled heat flux following K-Theory (local mixing) as well as frequently observed heat fluxes in the convective PBL. Adapted from Stull (1988).

The shallow convection scheme

The convective PBL frequently exhibits pronounced upward heat fluxes in regions with near-neutral or even stable stratification (Fig. 2.4). These heat-fluxes are associated with large eddies that can become as deep as the PBL, and that are mostly controlled by their buoyant production in the lower boundary layer. Despite being relatively large, these eddies still need to be parameterised, which in AROME-Arctic is done by a shallow convection scheme.

First, a fractional area a_u is defined that contains the strongest vertical velocities within the grid box. In AROME-Arctic, a_u is fixed at 10%. The turbulent flux of any quantity ϕ within the area a_u can be described as follows:

$$\overline{w'\phi'}^{\,a_u} = a_u(w_u - \overline{w})(\phi_u - \phi_e) = M(\phi_u - \phi_e) \tag{2.22}$$

whereby subscript u denotes updraft properties, e denotes the complementary environmental part, and $M \equiv a_u(w_u - \overline{w})$ (*Siebesma et al.*, 2007; *de Rooy and Siebesma*, 2008).

The updraft profiles $\phi_{u,i}$ are computed by an entraining plume model (*Neggers et al.*, 2007):

$$\frac{\partial \phi_{u,i}}{\partial z} = -\epsilon_k(\phi_{u,i} - \overline{\phi}) + \mu_\phi \tag{2.23}$$

whereby ϵ_k denotes the fractional entrainment, which describes the mixing of ambient air into the updraft, μ_ϕ denotes microphysical effects within the updraft, such as precipitation generation, and the subscript i denotes the updraft type with $i \in \{\text{dry, moist}\}$. These different updraft types allow for a more refined treatment of subgrid-scale convection in AROME-Arctic (*Neggers et al.*, 2007). The dry updraft stops around the lifting condensation level, whereas the moist updraft can penetrate beyond that level, lead to condensation, and foster cloud formation. These different updrafts play a central role for the aforementioned boundary-layer types, and are therefore also important for the analysis of the individual tendencies (see Sect. 4.1).

When being released, the moist updraft has a fixed updraft area fraction of $a_{u,moist} = 0.03$, which leaves the dry updraft area fraction at $a_{u,dry} = 0.1 - a_{u,moist}$. The subscript k in ϵ_k refers to the different entrainment formulations that are applied respectively in the dry convective case, the moist convective sub-cloud layer, and the cloud layer (*de Rooy et al.*, 2022):

$$\epsilon_{dry} = c_{dry}\left(\frac{1}{z + a1} + \frac{1}{z_{inv,dry} - z + a2}\right), \tag{2.24}$$

$$\epsilon_{sub} = c_{moist,sub}\left(\frac{1}{z + a1} + \frac{1}{z_{lcl} - z + \frac{z_{lcl}}{\epsilon_{lcl} \cdot c_{moist,sub}^{-1} - 1}}\right) \tag{2.25}$$

$$\epsilon_{cloud} = \left(\frac{1}{z + a1} + \frac{1}{z - z_{lcl} + \frac{1}{\epsilon_{lcl}}}\right) \tag{2.26}$$

where c_{dry}, $c_{moist,sub}$, $a1$, $a2$, and ϵ_{lcl} are model internal parameters, $z_{i,dry}$ denotes the inversion height of the dry updraft, and z_{lcl} denotes the height of the lifting condensation level.

At the lowermost model level, the updraft profiles are initialised with a temperature and humidity excess compared to the respective grid-scale mean. Temperature and

humidity are assumed to follow a Gaussian distribution within the grid box with a variance based on the turbulent surface fluxes (*de Rooy et al.*, 2022). The respective excess values are then defined as the 1-a_u percentile. Therefore, stronger turbulent surface fluxes lead to stronger excess values, and vice versa.

As a last step, the profile of the updraft's vertical velocity w_u is estimated, which, among others, yields the depth of the updraft (height where w_u becomes 0):

$$\begin{aligned} \frac{1}{2}\frac{\partial w_{u,i}^2}{\partial z} &= a_k\, B_{u,i} - b_k\, \epsilon_k\, w_{u,i}^2, \\ B_{u,i} &= \frac{g}{\overline{\theta_v}}(\theta_{v,u,i} - \overline{\theta_v}) \end{aligned} \tag{2.27}$$

$B_{u,i}$ describes the updraft's buoyancy, $\theta_{v,u,i}$ the updraft's virtual temperature (with $i \in$ {dry, moist}), and a_k and b_k are model internal parameters (with $k \in$ {dry, sub,moist}).

To summarize, the shallow convection scheme efficiently transports heat, humidity, momentum, and tracers away from the surface into the PBL. Hereby, the fluxes provided by the surface scheme (Sect.2.4) influence the excess of heat and moisture and therefore the initial buoyancy of the updraft, whereas the fractional entrainment determines how quickly the updraft is dispersed in the vertical and mixes with the rest of the grid box. As a summary of this Chapter, Figure 2.5 provides an overview of all parameterisation schemes employed in AROME-Arctic.

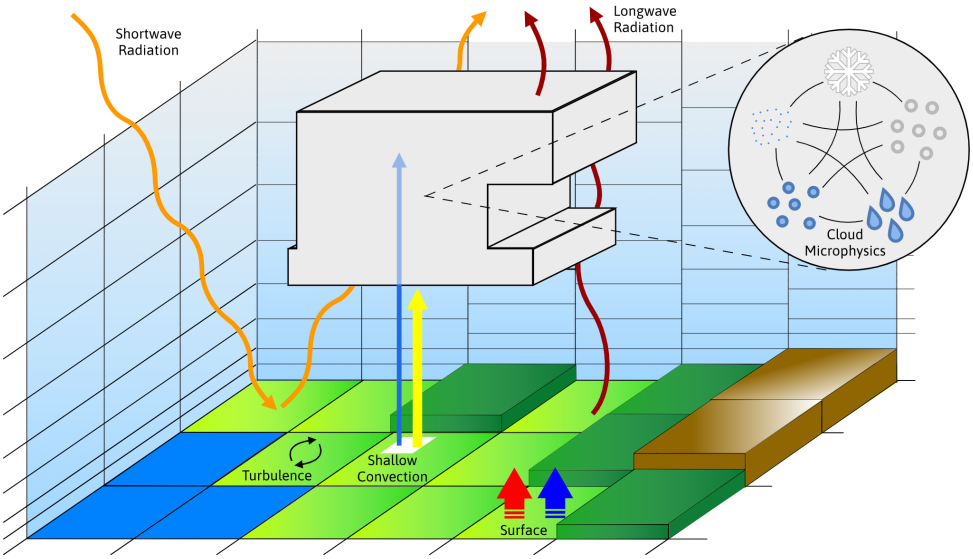

Figure 2.5: Schematic of all parameterisation schemes employed in AROME-Arctic, including radiation, surface processes, microphysics, turbulence, and shallow convection. Shallow convection: white surface indicates the updraft area fraction, yellow and blue arrows the dry and moist updraft, respectively. Surface: red arrow indicates sensible heat flux, blue arrow indicates latent heat flux. Microphysics: shown species are water vapor, cloud droplets, rain, grauple, and snow/cloud ice.

3 The individual tendency output

The previous chapter gave a description of the different parameterisation schemes employed in AROME-Arctic as well as their designated tasks. Noticeably, all of these schemes contain a multitude of model-internal parameters and interdependencies (e.g. the boundary layer schemes are fueled by the surface scheme) that make it difficult to follow the individual contribution of each scheme while a forecast is computed. However, knowledge about these contributions, called *individual tendencies*, is accessible, and has the potential to assist model analysis and development (Paper I,II,III).

In the literature, we find several uses of individual tendencies. *Niemelä and Fortelius* (2005) investigated spatially-averaged, individual tendencies over southern Finland to depict the adaption of the HIRLAM-NWP model towards modifications of the convection scheme. Thereby, they found an efficient compensation between dynamical and physical processes. A similar compensation is documented by *Kim et al.* (2018), who studied diabatic heating and moistening processes associated with the Madden–Julian Oscillation over the Indian Ocean. *Tomassini et al.* (2017) investigated the representation of vertical transport in several NWP models during an mCAO and found the best agreement between modeled and observed atmospheric liquid water and cloud ice content for models that exhibit the largest mixing tendencies (turbulence and shallow convection). For the SBL, *Savijärvi* (2006) and *Edwards* (2009b) depict the coupling between radiative and turbulent processes in an idealized model setup during clear-air nocturnal periods. Both studies find that turbulence dominates the bulk of the SBL, while radiative cooling is important at the top of the SBL and leads to a deepening of the stable layer. Close to the ground, the interplay between radiation and turbulence is found to be variable and is sensitive to the thermal roughness length and ambient wind speed (*Edwards*, 2009b). Studies that investigate tropical and extratropical cyclones often use potential vorticity (PV) which can be modified by diabatic processes (*Hoskins et al.*, 1985; *Haynes and McIntyre*, 1987). By using PV-tendencies, *Wu and Wang* (2000) investigates the role of diabatic heating for the development of tropical cyclones and *Joos and Wernli* (2012) depicts the individual contribution of microphysical processes to the latent heating in a warm-conveyor belt.

A different application of individual tendencies can be found in the so-called initial tendency method (*Rodwell and Palmer*, 2007; *Rodwell and Jung*, 2008). Hereby, the analysis increment of a short-time model forecast is evaluated together with individual tendencies to reveal systematic model errors. The analysis increment results from data assimilation and indicates how the model analysis has adjusted to observations. Following this approach, *Cavallo et al.* (2016) showed that middle-tropospheric warm biases in the WRF[1] model in the Atlantic basin are associated with the convection scheme and *Williams and Brooks* (2008) associated upper-tropospheric cold and moist biases in the UM[2] with an erroneous thickness of extratropical cirrus.

In the following Sections, I first define an individual tendency, then I depict where these tendencies appear during the model computations, and finally I describe how the

[1] Weather Research and Forecasting
[2] Met Office Unified Model

output of these tendencies was implemented in AROME-Arctic.

3.1 What is an individual tendency?

In the context of model computations, a tendency refers to the temporal change of any prognostic model variable X. Hereby, the absolute change $\frac{\Delta X}{\Delta t}$ (between e.g. two succeeding time steps, Fig. 3.1a) is often called the total tendency. This total tendency can be decomposed as follows (Fig. 3.1b):

$$\frac{\Delta X}{\Delta t} = D + K + \sum \Pi_i, \tag{3.1}$$

where D are the changes due to the model dynamics, K changes due to the horizontal diffusion, and $\sum \Pi_i$ denotes the contribution of the model physics, represented by the different parameterisation schemes of the model. $\sum \Pi_i$ is often called the *total physical tendency*. Hereby, Π_i refers to the individual tendency of the ith parameterisation scheme, with $i \in$ {microphysical adjustment, microphysics, radiation, turbulence, shallow convection} in AROME-Arctic (Figure 3.1c). By analyzing these individual tendencies, we can decipher the contributions and interplay of the different parameterisation schemes during the model calculations.

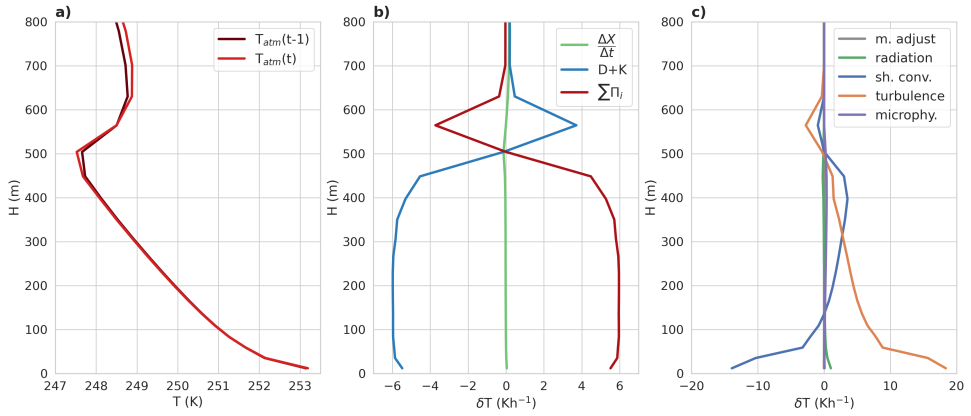

Figure 3.1: a) AROME-Arctic temperature profiles from two succeeding time steps. b) total tendency (green), dynamics plus horizontal diffusion (blue), and total physical tendency (red, compare Eq. 3.1). c) decomposition of the total physical tendency into the individual tendencies of microphysical adjustment, radiation, shallow convection, turbulence, and microphysics.

3.2 Computational organization of AROME-Arctic

I now present the order and role of these individual tendencies during the computation of a model time step. In AROME-Arctic, a model time step starts with collecting the prognostic variables from the end of the previous time step `T9` (*Seity et al.*, 2011, Fig. 3.2, top left). After that, the model's physical package is called. The first scheme to be

addressed is the mircophysical adjustment, which enforces thermodynamic equilibrium between the temperature field and the different microphysical species (Sect. 2.2). The adjusted model fields yielded by this scheme are subsequently used as input for all other parameterisation schemes (yellow arrow, Fig. 3.2). In this regard, the microphysical adjustement is special as the contributions of all other parameterisation schemes on the model fields of temperature, specific humidity, and momentum are not used as input for a subsequent scheme (*Seity et al.*, 2011). However, interdependencies between the schemes still exists as indicated by the black arrows (Fig. 3.2). The radiation scheme, for example, provides longwave and shortwave fluxes as input for the surface scheme, and the surface scheme in turn provides latent and sensible heat fluxes as input to the turbulence and shallow convection schemes.

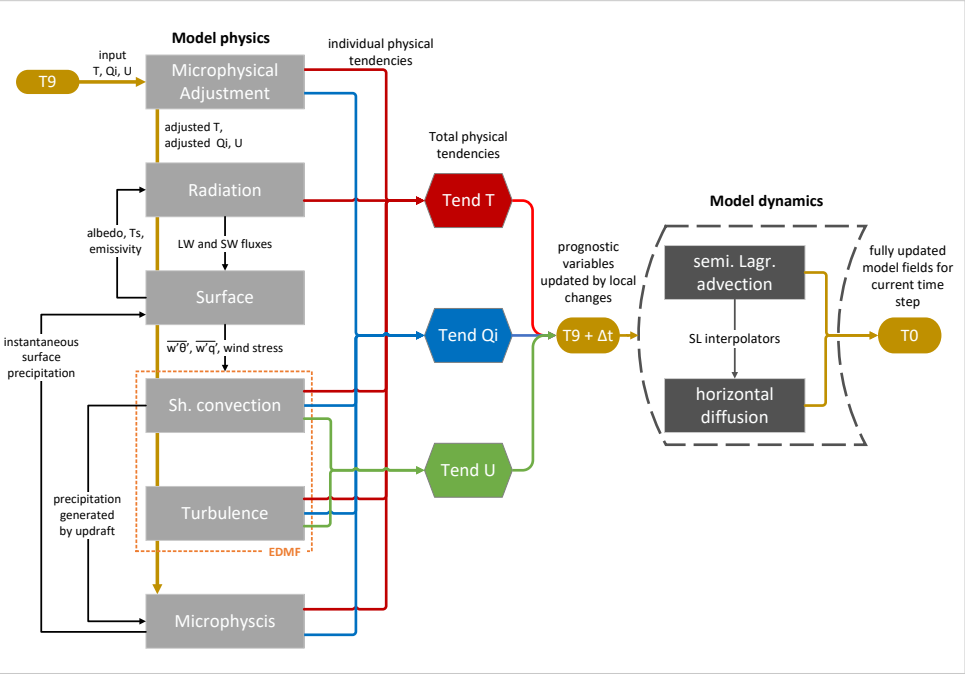

Figure 3.2: Organization of a model time step in AROME-Arctic. T9 refers to the previous time step, T0 to the current time step. T refers to temperature, Qi to respective microphysical species, and U to momentum. Yellow arrows follow the prognostic variables. Black arrows depict interdependencies between physical schemes. Red, blue, and green arrows depict physical tendencies for temperature, microphysical species, and momentum. In parts adapted from Seity et al. (2011).

The individual tendencies computed by each parameterisation scheme are subsequently summed up to the respective total physical tendencies $\sum \Pi_i$, which represents the local change due to all physical processes (Fig. 3.2, red, blue, green arrows). This total physical tendency is then added to the former grid scale variables at `T9`, providing updated model fields `T9` $+ \Delta t$ of temperature (red), microphysical species (blue), and momentum (green, Fig. 3.2). Finally, these updated model fields are given to the

spectral advection and horizontal diffusion scheme (Sect.2.1), yielding the fully updated model fields at `T0`.

3.3 Implementation of the tendency output

The implementation of the individual tendency output in AROME-Arctic (model cycle 40 and 43) can be divided into three major steps: I collect individual physical tendencies from the physics routines, II compute the dynamical tendency via a residuum, and III output of individual tendencies. In the following, I will discuss these three steps with the help of explicit FORTRAN examples from the AROME-Arctic model code.

3.3.1 Collecting the individual tendencies

All parameterisation schemes are called in the model routine `src/arpifs/phys_dnm/apl_arome.F90`. Among the returned variables from each of these schemes, we find the respective tendencies, as they are added to the total physical tendency (`PTENDT` in FORTRAN example below). Thus, we have to track the total physical tendency throughout the routine, then separately store the individual contributions coming from different parameterisation schemes. Below is a FORTRAN example for the temperature tendency due to turbulence:

```
! Individual tendency fields, temperature, MK
REAL(KIND=JPRB), INTENT(OUT) :: PTENDT_TURB(KLON,KLEV)
                                ⋮
PTENDT_TURB = 0.0_JPRB
                                ⋮
! computation of total physical tendency, temperature
! adding contribution from turbulence
DO JLEV = 1,KLEV
  DO JLON = KIDIA,KFDIA
    PTENDT(JLON,JLEV)=PTENDT(JLON,JLEV)+&
&   ZTENDTHL_TURB(JLON,1,JLEV) * ZZI_EXNREFM(JLON,1,JLEV)
! storing individual tendency, turbulence, PTENDT_TURB
    PTENDT_TURB(JLON,JLEV) = PTENDT_TURB(JLON,JLEV)+&
&   ZTENDTHL_TURB(JLON,1,JLEV) * ZZI_EXNREFM(JLON,1,JLEV)
  ENDDO
ENDDO
```

The two dimensions `KLON` and `KLEV` refer to the grid boxes and model levels respectively which are set in `ecf/config_exp.h`. The individual turbulence tendency `ZTENDTHL_TURB` provided by the turbulence scheme refers to potential temperature and is reverted back to temperature by multiplying the reference Exner function:

$$\texttt{ZZI\_EXNREFM} = \left(\frac{p}{p_0}\right)^{\frac{R_d}{c_p}}, \tag{3.2}$$

where p denotes pressure, p_0 a reference pressure of 1000 hPa, R_d refers to the gas constant of dry air, and c_p to the heat capacity of dry air.

All individual tendencies collected this way are returned by the subroutine call of `apl_arome.F90`, as indicated by the `INTENT(OUT)`, into the next higher routine `mf_phys.F90`. Here, steps II and III are carried out.

3.3.2 Computation of the dynamical tendency

While the collection of individual tendencies from the physical parameterisation schemes is mostly straightforward, a problem arises for the contributions coming from the model dynamics and the horizontal diffusion (Eq. 3.1). This problem is twofold. First, the physical parameterisations are all computed in grid-point space, whereas the model dynamics and horizontal diffusion are computed in spectral space (Sect. 2.1). Therefore, it can be difficult to collocate tendencies coming from the dynamics and physics respectively. The second, and more important problem is the order of computations in AROME-Arctic.

In AROME-Arctic, as well as all other HARMONIE-AROME setups, the model physics are called at the beginning of the time step computation, followed by the model dynamics (Fig. 3.2). As a result, it becomes impossible to identify any additional contributions coming from either the dynamics or horizontal diffusion within the same model time step, without risking double-counting contributions coming from the model physics. Therefore, the contribution of the model dynamics and horizontal diffusion are summarized and calculated as a residuum by subtracting the physical tendency from the total tendency (see Eq. 3.1). Evidently, this solution has three drawbacks:

1. the contribution from the model dynamics and horizontal diffusion cannot be evaluated separately
2. when computed for the diagnostic, the dynamical tendencies correspond to the *former* model time step and not to the present one
3. all individual tendencies from the physical schemes need to be stored for one model time step for a consistent output

In order to store variables for one time step, I use the GMV code implementation, also found in other models such as the Integrated Forecasting System (IFS). The GMV arrays (`PGMV` in the code) describe multilevel fields at timestep t and t - dt. The array is dimensioned as follows:

```
PGMV(NPROMA,NFLEVG,NFLDS,NGPBLKS)
```

Hereby, `NPROMA` describes the size of a computational block (coming from the parallel implementation), `NFLEVG` the number of vertical levels, `NFLDS` the number of fields stored within the array, and `NGPBLKS` the number of `NPROMA` blocks that each level is split in to.

Given the large number of fields stored in `PGMV`, a convenient method of addressing these fields was devised in the form of user-defined types, among which the `YT0`-type can be found that refers to the current time step t and the `YT9`-type that refers to the previous time step t - dt. These types point to the index of a desired field, e.g. `YT9%MT` for temperature at t - dt. To make use of this referencing, new pointers to the `YT9`-type have been added. This is done in the modules `src/arpifs/module/gmv_subs_mod.F90` and `type_gmvs.F90`, exemplified here for the turbulence tendency for temperature:

```
MODULE TYPE_GMVS
                                    ⋮
TYPE TYPE_T9
! new field pointer for GMV, MK
INTEGER(KIND=JPIM)  :: TTURB
```

```
MODULE GMV_SUBS_MOD
                                    ⋮
SUBROUTINE SETUP_T9
! getting the current last index of the NFLDS dimension
IPT = YT0%NDIM
! initialise the field, MK
YT9%TTURB = NUNDEFLD
! assigning the next unique index to the new field
IPT = IPT +1
YT9%TTURB = IPT
```

This procedure is required for every new field that is added to the PGMV-array, thus for every individual tendency to be stored.

Back in mf_phys.F90 the dynamical tendency is then computed as follows:

```
DO JLEV=1,NFLEVG
  DO JROF=KST,KEND
! calculating total and dynamical tendency, MK
    ZTTTOT  = (PGMV(JROF,JLEV,YT0%MT) -&
&               PGMV(JROF,JLEV,YT9%MT)) / ZDT
    ZTTDYN  = ZTTTOT  - PGMV(JROF,JLEV,YT9%TPHY)
  ENDDO
ENDDO
! store current tendencies for the next time step
PGMV(KST:KEND,1:NFLEVG,YT9%TPHY) = PTENDT
```

Here, ZDT refers to the model time step in seconds. In the actual code, the same loop contains the computation of all other dynamical tendencies as well as the preparation of the tendency output which I am going to discuss next.

The output of individual tendencies

For the output of individual tendencies, I use the GFL code implementation in combination with the EZDIAG-functionality. As the name suggests, EZDIAG allows for the implementation of model diagnostics which includes the output of model variables. Identical to YT9 in the PGMV-array, EZDIAG acts as a pointer to a field in the PGFL-array, with the additional benefit that these fields are directly forwarded to the model output.

The EZDIAG-fields are defined in the model's namelist nam/harmonie_namelsists.pm as such:

```
%arome=(
```

```
NAMGFL=>{
'NGFL_EZDIAG' => '3',
'YEZDIAG_NL(1)%CNAME' => '\'T_PHY\',',
'YEZDIAG_NL(1)%LREQOUT' => '.TRUE.,',
'YEZDIAG_NL(2)%CNAME' => '\'T_DYN\',',
'YEZDIAG_NL(2)%LREQOUT' => '.TRUE.,',
'YEZDIAG_NL(3)%CNAME' => '\'T_TURB\',',
'YEZDIAG_NL(3)%LREQOUT' => '.TRUE.,',
},
)
```

Hereby, `CNAME` provides the reference for the model output, `LREQOUT` determines whether the respective field is output, and `NGFL_EZDIAG` defines the overall number of fields contained in the diagnostic. An upper limit for that value is defined in `src/arpifs/module/yom_ygfl.F90` and is set to 50 in my experiments:

```
INTEGER(KIND=JPIM),PARAMETER :: JPEZDIAG = 50
```

Back in `mf_phys.F90`, the individual tendencies need to be assigned to the `PGFL`-array and accumulated. The accumulation is important, as tendencies are produced every model time-step (75 s), whereas model output is generated every forecast hour:

```
! Initialise and reset accumulation of tendencies, MK
IF (MOD(NSTEP*INT(ZDT),NDIAG_RESET) == 0) THEN
  PGFL(KST:KEND,1:NFLEVG,YEZDIAG(1)%MP) = 0.
  PGFL(KST:KEND,1:NFLEVG,YEZDIAG(2)%MP) = 0.
  PGFL(KST:KEND,1:NFLEVG,YEZDIAG(3)%MP) = 0.
ENDIF

! for first time step dyn calculation not possible
IF(NSTEP .GT. 0) THEN
  DO JLEV=1,NFLEVG
    DO JROF=KST,KEND
! physical tendency, temperature
      PGFL(JROF,JLEV,YEZDIAG(1)%MP) = &
&     PGFL(JROF,JLEV,YEZDIAG(1)%MP) + &
&    (PGMV(JROF,JLEV,YT9%TPHY  * ZDT)
! dynamical tendency (residuum), temperature
      PGFL(JROF,JLEV,YEZDIAG(2)%MP) = &
&     PGFL(JROF,JLEV,YEZDIAG(2)%MP) + (ZTTDYN   * ZDT)
! turbulence tendency, temperature
      PGFL(JROF,JLEV,YEZDIAG(3)%MP) = &
&     PGFL(JROF,JLEV,YEZDIAG(3)%MP) + &
&    (PGMV(JROF,JLEV,YT9%TTURB   * ZDT)
    ENDDO
  ENDDO
ENDIF ! nstep .GT. 0
```

The value of `NDIAG_RESET` can be controlled in the experiment's configuration file, whereby its default value is set to the output interval. The rather cryptic naming convention `YEZDIAG(1)` etc. simply iterates through the fields provided in the model's namelist, not their assigned names via `CNAME`. To facilitate a better comparison, I use similar names, e.g. `YEZDIAG_NL(1)`, in `nam/harmonie_namelsists.pm` (see above).

To activate all these changes, the switch `ALERTNESSTEND` has been added to the model's namelist. Finally, the new output variables need to be added to a conversion list that is used for converting the FA-output format of AROME-Arctic to a more convenient format, such as GRIB or NetCDF. The final result is the output of Eulerian tendencies, accumulated over the output interval of the model, at every model grid point and level.

4 About the use of individual tendencies in this study

This chapter depicts how individual tendencies are utilized in this study, providing more context to the four systematic steps described in Sect. 1.3. First, I will discuss factors that influence the analysis of individual tendencies. Then, the benefit of sensitivity experiments is illustrated. Finally, the unique combination of the individual tendency output with an other diagnostic, the Diagnostic on Horizontal Domains, is presented.

4.1 Factors that influence the analysis of individual tendencies

Throughout this work, the tendency output is targeted on the analysis of the model physics. Oftentimes, this analysis has to be put into context of influencing factors that need consideration when interpreting individual tendencies. In the following, I present the two factors that are most prominent in this work, namely model-internal boundary layer types and emerging stability regimes.

4.1.1 Boundary-layer types

Pivotal to the analysis of individual tendencies, is knowledge about model-internal statements that influence the calculations of a physical scheme. In AROME-Arctic, as well as other models e.g. IFS, ICON, or ARPEGE, such statements exists in the form of *planetary boundary-layer types* (PBL types). These PBL types strongly impact the shallow convection scheme and, through various interplay, also other parameterisation schemes (Paper I). The idea of PBL types is to adapt the shallow convection scheme to the requirements associated with different atmospheric states.

AROME-Arctic distinguishes between five PBL types (Fig. 4.1): stable PBL (I), dry convective (II), stratocumulus topped (III), shallow cumulus topped (IV), and deep convective(V). Each PBL type is associated with a different combination of updrafts (dry or moist, see Sect. 2.5) that are released by the shallow convection scheme. In the stratocumulus PBL (type III), for example, only a moist updraft is released, whereas in the shallow cumulus PBL (type IV) both dry and moist updrafts are released. As both updrafts are associated with different updraft profiles and entrainment rates (Eqs. 2.23 - 2.26), the vertical transport of heat, moisture, and momentum is very different for the two PBL types. Thus, a strong increase in parameterised heat transport from the shallow convections scheme can simply result from a step-wise transition in PBL type. As such a transition is not necessarily connected to any clear changes in e.g. surface heat fluxes or atmospheric stability, it can be quite puzzling to interpret the resulting individual tendencies without knowing about PBL types.

Usually, model fields such as the PBL types are not part of the standard output of NWP models and are unknown to many end users, yet these fields provide a useful insight for contextualizing the model computations. As advocated by Paper I, PBL types are going to be added to the standard output of AROME-Arctic in an upcoming model cycle (pers. comm. Eivind Støylen, MET-Norway). In the context of this work, PBL types are integral for interpreting the individual tendency output.

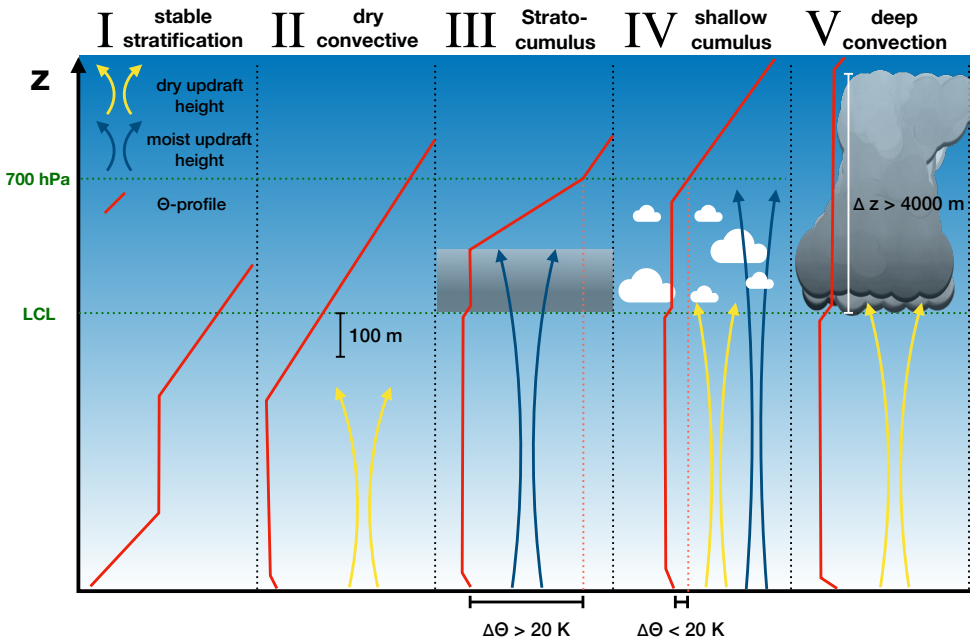

Figure 4.1: Boundary layer types in AROME-Arctic and their implications for the shallow convection scheme. Idealized potential temperature profiles are shown in red. Yellow and blue arrows depict dry and moist updrafts. Green stippled lines indicate LCL and 700 hPa level respectively, red stippled lines indicate the criteria for PBL type III and IV (Klein and Hartmann, 1993). Fig. 2 in Paper I.

4.1.2 Stability regimes

The second factor to take into consideration are different atmospheric regimes that are not predefined in the model code such as the PBL types, but emerge due to the model's physical representation of the atmosphere. In Paper II, and Paper III those come in the form of the two different stability regimes already introduced in Sect. 1.2.2: the weakly-stable boundary layer (wSBL) and the very-stable boundary layer (vSBL). The different feedback mechanisms between increased stratification and turbulent mixing (negative in the wSBL, positive in the vSBL) need to be represented by the respective parameterisation schemes. This representation is reflected by distinctly different individual tendencies of turbulence, radiation, and model dynamics (Paper II). To my surprise, I find that these stability regimes coexist on small spatial scales of about 5 km in AROME-Arctic. Furthermore, the vSBL can cause a decoupling of the lowermost atmospheric model level (Paper II) or the surface (Paper III), shown by the individual tendencies. The two boundary layer regimes also respond differently to changes in the model formulation (Paper II). Thus, any ensuing analysis of the stable boundary layer that focuses on process representation requires differentiation between the wSBL and vSBL.

4.2 Sensitivity experiments

All conducted studies incorporate substantial changes to the physical parameterisation schemes. Guided by the aim of improving weather forecasts for high-latitudes, these changes include a comprehensive update to the shallow convection scheme (Paper I), a refined treatment of the surface (Paper II), and a physically-motivated adjustment to the surface-atmosphere coupling (Paper III). These sensitivity experiments allow me to demonstrate the utility of individual tendency output for model development and provide a reference for the analysis of tendencies.

For all investigated phenomena, the analysis of individual tendencies reveals a complex interplay between multiple processes. This interplay usually appears plausible as our parameterisation schemes, despite tuning, adhere to physical principles. In the sensitivity experiments, this interplay needs to adapt, often revealing strongly compensating terms. In some cases, this compensation fully absorbs the modifications, leading to unchanged grid scale variables, even though the individual tendencies increase or decrease by an order of magnitude. Thereby, sensitivity experiments help to refine an analysis by focusing on regions that are especially affected by the changes on the grid or on the sub-grid scale.

4.3 Model time-step output with DDH

In its default configuration, the tendency output provides accumulated values over the hourly output interval of the model. In some instances, this can be too coarse a resolution, as processes might act intermittently on short time scales, or the heterogeneity of model fields (PBL types, stability regimes) changes abruptly. Examples of such behavior are turbulence in the stable boundary layer (*Zilitinkevich et al.*, 2013; *Vercauteren et al.*, 2019) and the abrupt transitions between stability regimes (*McNider et al.*, 1995; *Derbyshire*, 1999). To capture such model behavior, we require a more frequent output of model fields, ideally at every single model time-step. However, doing so on the entire model domain would impose unmanageable requirements on the analysis.

Fortunately, there exists a tool in the HARMONIE-AROME consortium called *diagnostics par domaines horizontaux* (DDH, *Météo-France*, 2019). DDH enables the output of model variables over user-defined sub-domains at every model integration timestep. The user-defined sub-domains can be grouped into three different types of domains (Fig. 4.2). Type 1 consists of individual points which can either be described by their geographical positions or their model indexes. Each of these individual points provides output for every model level at every time step. Type 2 and Type 3 describe quadrilateral areas that can either be defined by the position of their four corners (Type 2) or the position of two opposite corners (Type 3). These two last area types provide horizontally averaged values of all contained grid boxes for every model level.

For my purposes, I utilize Type 1 to provide detailed information about an area of interest in the model (Paper II, III)[1]. Each grid point located in that area then outputs selected variables, including individual tendencies, at every model time step. This unique

[1] A documentation of my DDH implementation in AROME-Arctic, in form of a recorded presentation can be found here: https://www.youtube.com/watch?v=SOdJyg82d2I

combination of the two diagnostics provides unparalleled insight into the sub-grid scale processes of AROME-Arctic.

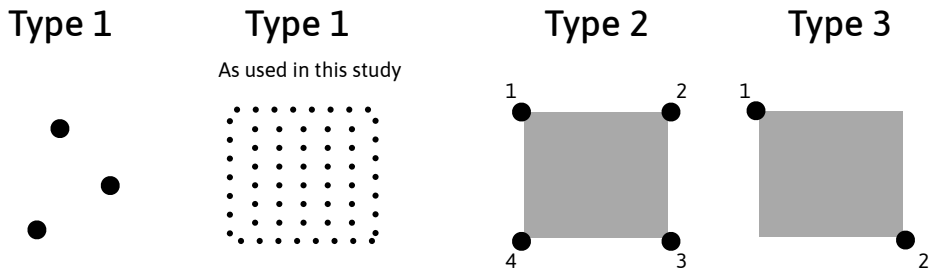

Figure 4.2: Schematic depiction of the three types of output provided by DDH, including the setup of Type 1 used in this study. The anti-cyclic enumeration of the corners in Type 2 and Type 3 reflects the order in the namelist. Grey shadings in Type 2 and Type 3 indicate that horizontal averages of all contained grid points are provided.

5 Summary of scientific results

Paper I: On the Utility of Individual Tendency Output: Revealing Interactions between Parameterized Processes during a Marine Cold Air Outbreak

Marvin Kähnert, Harald Sodemann, Wim C. de Rooy, and Teresa M. Valkonen (2021), Weather and Forecasting, 36(6):1985 – 2000, https://doi.org/10.1175/WAF-D-21-0014.1

Paper I characterises the contributions of parameterised processes during an extensive marine cold-air outbreak (mCAO). We investigate how the interplay between individual physical processes modulates the rapid build-up of the boundary layer and the representation of mesoscale convection in the model. The study demonstrates the central role of model-internal boundary-layer types for the contribution of individual schemes and their interplay. Further, we test the sensitivity of that interplay against an increase or decrease of the parameterised shallow convection, and evaluate the ensuing impact on the representation of the mCAO. We depict a shift between resolved and parameterised convection that leads to more numerous, small-scale cellular clouds when convection is predominately resolved and more broad, areal clouds when convection is predominately parameterised (Fig. 5.1). We reveal pronounced compensation between individual processes that can lead to nearly unchanged residuals, despite significant changes in the individual tendencies by up to an order of magnitude. Further, we are able to trace back grid-scale responses of the model to their underlying causes in either the model dynamics or model physics. We thereby point to a potential caveat for future model development: Modifications that improve the model's performance for subgrid-scale shallow cumulus convection by increasing the parameterised convective transport potentially decrease model performance for cases with partially resolved convection.

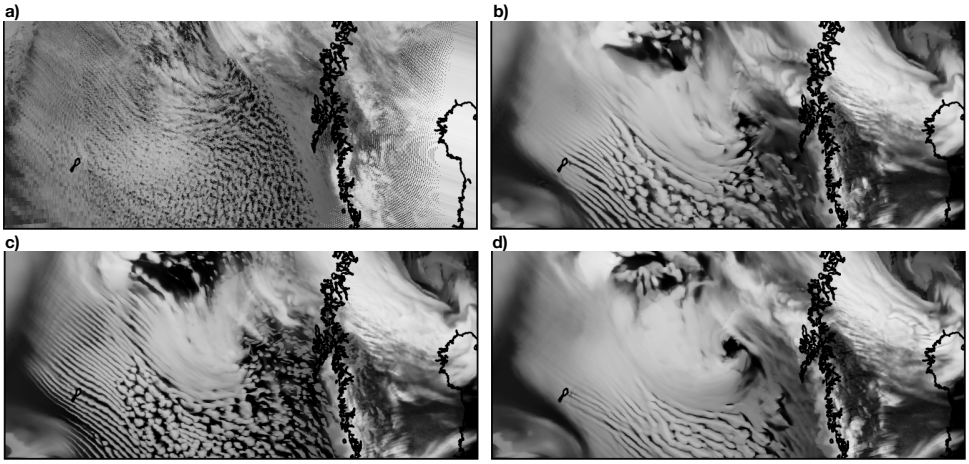

Figure 5.1: a) Satellite image during the studied mCAO. Simulated cloud cover of b) the reference run, c) no shallow convection, d) increased shallow convection. Adapted from Fig. 11, Paper I.

Paper II: Spatial variability of nocturnal stability regimes in an operational weather prediction model

Marvin Kähnert, Harald Sodemann, Teresa M. Remes, Carl Fortelius, Eric Bazile, and Igor Esau, in review at Boundary-Layer Meteorology

Paper II studies the temperature development in the stable boundary layer during cloud-free, snow-covered nights. These periods frequently exhibit pronounced warm biases in near-surface temperature estimates, and constitute a persistent model error for high-latitude weather forecasts. We focus on a case from YOPP SOP1[1] at the Sodankylä supersite, Finland. By combining the individual tendency output with DDH, we utilise high-resolution tendencies for our analysis. Our analysis distinguishes between the two stability regimes: wSBL and vSBL. We depict how the distinct feedback mechanisms of parameterised processes associated with these two regimes lead to considerably different temperature profiles, from near-neutral in the wSBL to pronouncedly stable in the vSBL (Fig. 5.2 a, b). During our case study, both regimes coexists on small spatial scales of about 5 km (Fig. 5.2 c). Further, we demonstrate the sensitivity of the simulated, nocturnal temperature development using an updated treatment of the surface, which allows for a more efficient surface cooling. Even though the sensitivity experiment strongly impacts parameterised processes, only the very-stable regime exhibits changes in near-surface temperatures. In the weakly-stable regime, the more efficient surface cooling is compensated by an increased turbulent transport of heat within the boundary layer. The study highlights the necessity to differentiate between different stability regimes, and emphasises the potential of individual tendencies diagnostic at high-resolution for model analysis and development.

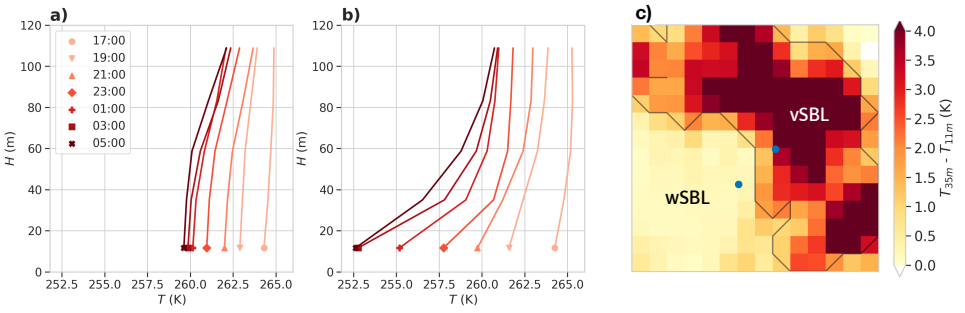

Figure 5.2: Temperature profiles of a) a grid box exhibiting the wSBL, b) a grid box exhibiting the vSBL. The markers indicate time stamps of the profiles in UTC. c) temperature differences between the lowest two model levels in AROME-Arctic for the studied domain of 14x14 grid boxes around Sodankylä, Finland. Black contours depicts the differentiation between the two stability regimes. The blue dots depict the two grid boxes in a) and b). Adapted form Fig. 7 and Fig. 9 in Paper II.

[1] Year of Polar Predeiciton Special Observing Period 1

Paper III: **Probing the stable boundary layer in an operational weather prediction model - Impacts of surface coupling and vertical resolution**

Marvin Kähnert, Harald Sodemann, Teresa M. Remes, Carl Fortelius, and Mariken Homleid, in preparation

Paper III investigates the role of surface-atmosphere coupling and vertical model resolution on the representation of the stable boundary layer in AROME-Arctic. A specific focus is on the different stability regimes. We focus on a 70 km × 70 km domain around the Sodankylä supersite, Finland. Operationally, AROME-Arctic does not allow for stability to occur in the surface layer, leading to a continuous coupling between the surface and the lowermost model level. When allowing for stability to occur in the surface layer, we find an occasional decoupling of the surface in the vSBL, resembling a run-away cooling. Surface temperatures cool pronouncedly while the atmosphere exhibits less cooling due to the missing heat sink and becomes well-coupled (Fig. 5.3 a,b,d,e). Thus, allowing for a stable surface layer reduces the warm bias at the surface, often encountered in the vSBL, but might simultaneously decrease model performance in the near-surface atmosphere. Validation studies thus need to investigate both surface temperatures and near-surface profiles in tandem. Increasing the vertical resolution yields stronger vertical temperature gradients in the SBL, often underestimated in NWP models. However, we find next to no change in surface and near-surface temperatures (Fig. 5.3 c). We identify the underlying reason in an equally deep layer that remains coupled to the surface, and thus needs to be cooled, in both the experiment with coarser and finer vertical resolution. In a few instances we find a decoupling of only the lowermost model level in the high-resolution run (Fig. 5.3 f), accompanied by pronounced surface cooling.

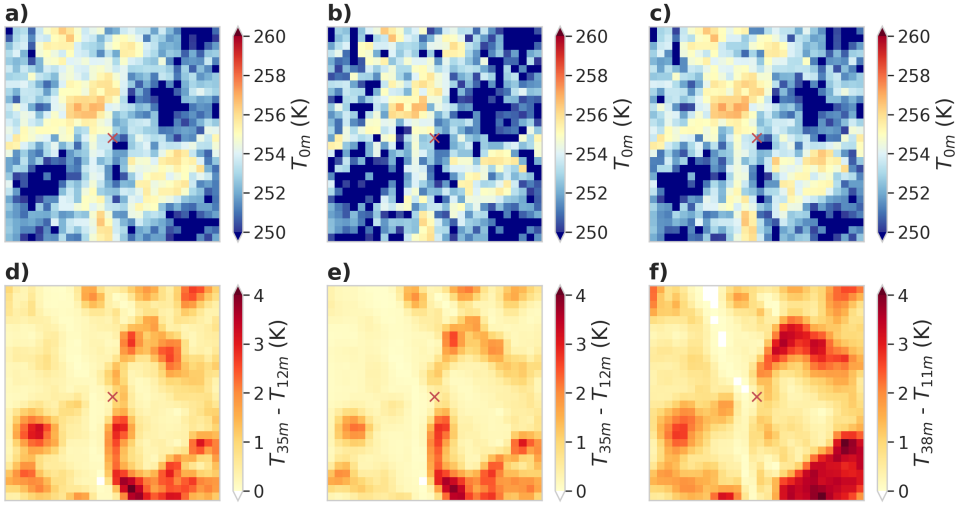

Figure 5.3: Surface temperature (first row) and near-surface temperature inversion strength (second row). Each column depicts a different model run, form left to right: reference, modified surface coupling, enhanced vertical resolution. Adapted from Fig. 4 in Paper III.

6 Discussion and further perspectives

6.1 Why should we use individual tendencies?

The complex inner workings of a numerical model in form of its physical and dynamical schemes can create the impression of a black box. Individual tendencies help to open up this box and allow for a deep insight and analysis of modeled processes. This analysis reveals the effects of "hidden" interactions between different schemes and highlights the role of model internal parameters such as PBL types, unknown to most users, but central for the model computations.

For example, we might initially be confused as to why the model exhibits two different cloud morphologies, in the form of more stratiform cloud cover versus cellular convection, over areas in the model with seemingly similar conditions. The underlying reason, however, becomes clear once we associate these different areas with the shallow cumulus and deep convective PBL type. In the deep convective PBL type, the shallow convection scheme remains idle within the clouds, requiring the model dynamics to resolve most of the atmospheric instabilities. To do that, the model introduces grid-scale vertical up- and downdrafts which subsequently lead to a break-up of clouds in the downdraft regions (Paper I). In the shallow cumulus PBL type, in contrast, the shallow convection scheme is active within the clouds, and removes most of the instabilities. This strongly reduces the formation and strength of downdrafts and leads to the more stratiform cloud cover.

Importantly, the individual tendency output allows for process-oriented studies within a fully developed, three-dimensional model. Often, more simplified setups such as single-column models (SCM) are used to study specific phenomena like the stable PBL (*Steeneveld et al.*, 2006; *Savijärvi*, 2006; *Baas et al.*, 2008; *Edwards*, 2009a), subgrid-scale convection (e.g. *de Rooy et al.*, 2022), or clouds (*Engdahl et al.*, 2020). Such SCM experiments are ideal for testing modifications to the model formulations as they are relatively easy to set-up and only require short run times. However, these studies cannot properly include effects such as surface heterogeneity or advection. The individual tendency output from a full-scale NWP simulation thus complements such SCM studies. Furthermore, the combination with DDH (Paper II, III) even allows to compare 3D-model and SCM experiments, as the high-temporal resolution provided by DDH matches that of a SCM.

6.2 What did we learn about process representation in AROME-Arctic?

The computations of AROME-Arctic are often influenced by regional heterogeneities of model fields, which can appear on very small scales. In particular the role of the aforementioned PBL types as well as the stability regimes constitute important findings of this study. As discussed in Paper II, the stability regimes can appear on scales of two model grid boxes (5 km), and are associated with distinctly different temperature

profiles. Accounting for these regimes is, for example, crucial during validation studies to avoid large representativeness errors (*Kanamitsu and DeHaan*, 2011), especially when using single-point observations (*Køltzow et al.*, 2019).

Regarding the analysis of tendencies, one of the most prominent aspects is the strong compensation between individual processes, also documented by other studies (*Niemelä and Fortelius*, 2005; *Tomassini et al.*, 2017; *Kim et al.*, 2018). This compensation yields comparably small residual terms despite large individual contributions of some tendencies, and can cause unwanted side effects for model development (see next Section).

In some instances, this compensation is reasonable. One example is the strongly compensating interplay between turbulence and shallow convection (Paper I). During unstable conditions, the shallow convection scheme cools the lower atmosphere by efficiently transporting heat upwards to higher model levels. This cooling increases the surface-atmosphere temperature gradient, fueling the turbulence scheme, which, in turn, warms the lower atmosphere and compensates the cooling caused by the shallow convection scheme.

In other instances, this compensation is a bit more obscure. One example is the interaction between the model dynamics and the model physics found in all of our studies. In Paper I, the compensating interplay during the mCAO can be respectively traced back to the horizontal advection of cold air, and the vertical advection (upwelling) of warm air, which has an profound impact on the turbulence scheme. Within the stable boundary layer (Paper II, III), however, the reason for the compensation is not as apparent. We speculate that the compensation is partly attributed to horizontal diffusion that mixes the temperature signals of neighbouring grid cells and causes a cooling of warmer grid cells and vice versa, but more investigations are necessary here.

Apart from the compensation, tendencies allow to decipher the physical representation of different atmospheric regimes in the model. The two stability regimes are a clear example (Paper II). In the wSBL, the simulated turbulence couples the boundary layer, yielding an efficient heat transport between the different model levels, and creates respective slow cooling rates. In the vSBL, in contrast, the coupling between levels is strongly reduced, leading to faster cooling rates and even a decoupling of the lowermost model level.

This decoupling is especially interesting in regards to the "unphysical", maximum Richardson number of 0, applied operationally within the surface layer of the model (Paper III). This setting causes a continuous exchange between the surface and atmosphere. The decoupling of the lowermost model level during the vSBL can thus be regarded as some sort of equivalent to the viscous sublayer in the model, though far deeper compared to reality. This depth also explains the often documented warm bias of surface or 2 m-temperatures in models during stable periods (*Atlaskin and Vihma*, 2012; *Sandu et al.*, 2013; *Holtslag et al.*, 2013; *Køltzow et al.*, 2019), as too deep a layer needs to be cooled during the night (*Esau et al.*, 2018).

Increasing the maximum Richardson number allows for a stably stratified surface layer, and can cause a decoupling of the surface from the atmosphere in the vSBL (Paper III). At these instances, surface and 2 m-temperatures become significantly colder during the night compared to simulations with XRIMAX=0 (sometimes over 8 K). This cooling, however, is not translated to the near-surface atmosphere, which exhibits more neutral and warmer temperature profiles as the turbulent heat loss to the ground is strongly

diminished. As a consequence, near-surface inversions start to disappear even in the vSBL.

This potentially unwanted effect is especially present in valley systems but can also be seen over more flat terrain such as Sodankylä (Paper III). Such an effect would most likely go unnoticed during model validation when one solely relies on 2m-temperature estimates. Therefore, validation studies should include measurements that both correspond to the near-surface temperatures (0 m, 2 m) as well as temperatures at the lower most atmospheric levels, e.g. gained from radiosondes or weather masts.

6.3 How can tendencies help to improve (Arctic) weather prediction?

In a tuned model system, changing existing components of the model, as is necessary during continued development, can cause unwanted interactions that deteriorate model performance (*de Rooy et al.*, 2022). Tendencies can reveal these interactions and allow to trace back changes, or the lack thereof, seen at the grid-scale to the underlying processes.

In Paper I, for example, we identified regions in the model that, despite pronounced changes to the model formulations, exhibit next to no change on the grid scale variables. This absence of change could be explained by the compensation between the turbulence and shallow convection scheme. Hereby, the individual tendencies varied by up to an order of magnitude between different model configurations, but, when summed up, yielded the same heating or moistening contribution to the grid scale variables.

Another example can be found in Paper II. Here, the conducted sensitivity experiment brought sophisticated changes to the surface scheme, aimed at enabling, among others, a more efficient cooling of the surface. However, the conducted changes only came to fruition in the vSBL, and were compensated by the efficient turbulent heat transport in the wSBL. Such an interplay is important to identify as it can prevent tuning into an ill-posed state. In the depicted case of the wSBL, for example, a more efficient cooling of the surface and near-surface levels is unlikely to be achieved by further modifying the updated surface scheme, but rather by adapting the turbulence scheme.

Regarding the cooling of near-surface model levels, the findings of Paper II agree with *Esau et al.* (2018) who attributed the often documented warm bias in NWP models during nocturnal, stable periods to a too deep representation of atmospheric boundary layers. Such deep boundary layers are associated with a large heat capacity, and in case of an efficient coupling (wSBL) cause too much thermal inertia that inhibits a fast nocturnal cooling. An updated length scale formulation accounting for this effect is currently near its completion (pers. comm. Igor Esau) and will soon be tested for AROME-Arctic, including an analysis of individual tendencies.

6.4 Limitations

The individual tendency analysis presented in this thesis requires a thorough preselection of data. In Paper I, a distinction by PBL types had to be made, in Paper II a distinction by stability regimes, and in Paper III, a distinction by different variants of the vSBL. Studies that focus on longer time spawns cannot investigate every single day in such detail. Such studies require a metric or specific visualisation that allows to efficiently

group process representations by the individual tendencies. The output of PBL types benefits such a metric, however, other NWP models might require the consideration of additional (model-internal) factors.

This brings me to the next limitation of this work. Only the individual tendencies of AROME-Arctic are investigated here. Other models employ different dynamical and physical schemes, resulting in distinctly different individual tendencies (*Tomassini et al.*, 2017). Given the strong interactions between the model dynamics and model physics shown in this thesis, already the choice of the dynamical core, e.g. more diffusive or less diffusive, will influence the individual tendencies even when the same parameterisation schemes are used. Thus, it is difficult to formulate general statements about process representation in NWP models due to the lack of a norm or reference.

6.5 Potential ways forward

Validation of model tendencies

One drawback for the analysis of individual tendencies is the lack of a reference. Such a reference can be provided by observations in the form of estimated heating rates due to e.g. turbulence or radiation. Following the setup of *Sun et al.* (2003), observations of sensible and radiative heat fluxes at two different heights yield the heating rates by radiation and turbulence for that atmospheric layer. During stable conditions, these heating rates can be compared to the individual tendencies and would provide novel insights into shortcomings of process representation in the model.

Towards hectometric models and the gray zone

Tendencies can also play a role in the ongoing endeavor seen at many operational weather centers to employ models at hectometric-scale resolution of $O(100m)$. This resolution regime is commonly referred to as the gray zone of turbulence due to the emerging difficulties to distinguish between resolved and parameterised scales of motion, especially in the convective boundary layer (*Wyngaard*, 2004; *Done et al.*, 2004; *Niemelä and Fortelius*, 2005; *Deng and Stauffer*, 2006). These difficulties can lead to an erroneous partitioning between parameterised and resolved vertical transport (*Honnert et al.*, 2011). Resulting model errors include the absence of meso-scale organisation (too much parameterised transport) or the occurrence of too large vertical wind velocities and precipitation intensities (too much resolved transport). In fact, the representation of convective structures in an mCAO is already prone to that problem at meso-scale resolution (*Field et al.*, 2017; *Tomassini et al.*, 2017, Paper I).

In the gray zone, boundary layer schemes cannot assume that turbulent length scales are always much smaller compared to the resolved scales, and therefore their formulation cannot be independent from the model resolution. Parameterisation schemes that do account for this are usually referred to as scale-aware parameterisations (*Honnert et al.*, 2020). Tendencies could be used to quantify how much energy is transported by a scheme at varying model resolutions and thereby test its scale-awareness. Furthermore, the impact that a different partitioning between resolved and parameterised transport has on other parameterisation schemes can be investigated. The scale-aware scheme introduced by *Sakradzija et al.* (2016) might be a promising candidate for AROME-

Arctic, as it builds upon the same EDMF-framework already in use for the boundary layer scheme.

Use in ensemble prediction systems

In an ensemble prediction system it is common to perturb the parameterisation schemes to enhance the model spread. Established approaches are the stochastically perturbed physics tendencies scheme (SPPT, *Buizza et al.*, 1999) or the stochastically perturbed parameterisations scheme (SPP, *Ollinaho et al.*, 2017). In SPPT, the tendencies provided by individual schemes are perturbed, whereas in SPP, free parameters within the schemes are varied stochastically. In most models, the perturbations done by SPPT and SPP are sampled by spatial and temporal correlations (e.g. *Frogner et al.*, 2019b). These correlations are created by a pattern generator and this pattern, while being well-constrained, is mostly random.

As a result, the perturbations might be routinely applied at locations where there is no or only little activity of the respective schemes. Instead of using a random pattern, one idea could be to use the distinct patterns in tendency activity, as was for example shown in Paper I, to constrain the perturbation and investigate whether and how it impacts the ensemble spread.

7 Scientific papers

Paper I

On the Utility of Individual Tendency Output: Revealing Interactions between Parameterized Processes during a Marine Cold Air Outbreak

Marvin Kähnert, Harald Sodemann, Wim C. de Rooy, and Teresa M. Valkonen
Weather and Forecasting, **36(6):1985 – 2000**, https://doi.org/10.1175/WAF-D-21-0014.1 (2021)

On the Utility of Individual Tendency Output: Revealing Interactions between Parameterized Processes during a Marine Cold Air Outbreak

MARVIN KÄHNERT,[a,b] HARALD SODEMANN,[a,b] WIM C. DE ROOY,[c] AND TERESA M. VALKONEN[d]

[a] *University of Bergen, Geophysical Institute, Bergen, Norway*
[b] *Bjerknes Centre for Climate Research, Bergen, Norway*
[c] *Royal Netherlands Meteorological Institute (KNMI), De Bilt, Netherlands*
[d] *Development Centre for Weather Forecasting, Norwegian Meteorological Institute, Oslo, Norway*

(Manuscript received 9 February 2021, in final form 30 August 2021)

ABSTRACT: Forecasts of marine cold air outbreaks critically rely on the interplay of multiple parameterization schemes to represent subgrid-scale processes, including shallow convection, turbulence, and microphysics. Even though such an interplay has been recognized to contribute to forecast uncertainty, a quantification of this interplay is still missing. Here, we investigate the tendencies of temperature and specific humidity contributed by individual parameterization schemes in the operational weather prediction model AROME-Arctic. From a case study of an extensive marine cold air outbreak over the Nordic seas, we find that the type of planetary boundary layer assigned by the model algorithm modulates the contribution of individual schemes and affects the interactions between different schemes. In addition, we demonstrate the sensitivity of these interactions to an increase or decrease in the strength of the parameterized shallow convection. The individual tendencies from several parameterizations can thereby compensate each other, sometimes resulting in a small residual. In some instances this residual remains nearly unchanged between the sensitivity experiments, even though some individual tendencies differ by up to an order of magnitude. Using the individual tendency output, we can characterize the subgrid-scale as well as grid-scale responses of the model and trace them back to their underlying causes. We thereby highlight the utility of individual tendency output for understanding process-related differences between model runs with varying physical configurations and for the continued development of numerical weather prediction models.

SIGNIFICANCE STATEMENT: Accurately capturing the evolution of the lower atmosphere with weather models in use at national forecasting centers requires the representation of processes from millimeter to subkilometer scale. Examples are the formation of water droplets within clouds or the transport of heat by turbulent swirls. All of these processes are represented by simplified formulations that introduce uncertainty into models. In this study, we employ a new diagnostic in the forecast model AROME-Arctic to investigate the contributions of these simplified processes. We identify regimes that foster distinct contributions to the heat and humidity profiles from individual processes, allowing us to explain changes to the modeled temperatures or vertical velocity. Knowledge of these regimes aids in the interpretation of the output from weather models, highlighting the benefit of our diagnostics for researchers and weather forecasters.

KEYWORDS: Diagnostics; Mesoscale models; Numerical weather prediction/forecasting; Parameterization; Subgrid-scale processes

1. Introduction

High-impact weather events in the Arctic, such as maritime icing, severe snow showers, and polar lows, are often linked to marine cold air outbreaks (mCAO; Businger and Reed 1989; Papritz and Pfahl 2016; Samuelsen and Graversen 2019). During an mCAO, cold and dry air is advected over warmer waters. The resulting strong air–sea temperature contrasts give rise to intense sensible and latent heat fluxes that have been observed to exceed 1000 W m^{-2} (Grossman and Betts 1990). Such heat fluxes transform the formerly cold, dry, and stably stratified air masses into warmer, more humid, and unstable air masses, giving rise to pronounced convective mixing and cloud formation (Etling and Brown 1993; Hartmann et al. 1997). Heavy precipitation can therefore result downstream of an mCAO and affect the population and infrastructure in coastal regions. Adequately forecasting mCAOs is thus an important task for operational weather forecasting centers.

Yet, numerical weather prediction (NWP) models often struggle to accurately forecast mCAOs (Field et al. 2017; Abel et al. 2017). Prominent challenges include forecasting the rapid growth of the boundary layer, the development

Denotes content that is immediately available upon publication as open access.

Supplemental information related to this paper is available at the Journals Online website: https://doi.org/10.1175/WAF-D-21-0014.s1.

Corresponding author: Marvin Kähnert, marvin.kahnert@uib.no

DOI: 10.1175/WAF-D-21-0014.1

and composition of boundary layer clouds, and the transition in cloud cover during an mCAO. All of these characteristics involve microscale and mesoscale processes that in turn rely on the accurate calculation of subgrid-scale processes, such as turbulent fluxes and cloud microphysical variables.

Due to the limited resolution in current NWP models, the effect of subgrid-scale processes is represented by parameterization schemes, including the turbulence scheme, shallow convection scheme, and microphysics scheme. At high latitudes, where mCAOs are prevalent, these schemes are often poorly constrained (Morrison et al. 2012; Vihma et al. 2014), while some even reach their limits of applicability, such as the shallow convection scheme (Honnert et al. 2011; Holloway et al. 2014). The spectrum of convective length scales during an mCAO cannot be fully represented by the kilometer-scale grid spacing of current operational NWP models. Therefore, difficulties emerge to define a proper partitioning between the amount of resolved and parameterized vertical transport. These difficulties can lead to an overrepresentation of parameterized vertical transport in the model and therefore to model error (e.g., Honnert et al. 2011).

Thus, the accuracy of an mCAO simulation critically depends on the interplay between resolved scales and the contribution from several physical parameterization schemes that each have specific limitations. Even though this interplay has been recognized to contribute to forecast uncertainty (Vihma et al. 2014; Field et al. 2014; Abel et al. 2017), a quantification of this interplay is so far lacking.

To quantify the interplay of parameterized physical processes, and to assess their contributions to the model state, we implement here the output of the physical tendencies contributed by individual parameterizations, termed *individual tendency output*, in an operational NWP model. We use the operational, limited-area NWP model AROME-Arctic (Müller et al. 2017b) and focus our analysis on physical tendencies for temperature and specific humidity. A major mCAO in 2015, studied by Papritz and Sodemann (2018), which impacted a particularly large fraction of the Nordic seas (and also the model domain) forms our case study. Using the individual tendency output, we study the interplay between resolved and parameterized processes, and assess the sensitivity of this interplay to changes in the model's physical parameterizations.

2. Model description and methods

a. AROME-Arctic

AROME-Arctic is an operational, convection-permitting forecasting system covering the European Arctic (Fig. 1). The base NWP model used for AROME-Arctic, and for the implementation of the individual tendency output is HARMONIE-AROME cycle 40h1.1 (Bengtsson et al. 2017). In the current configuration, the model has a horizontal grid spacing of 2.5 km, 65 vertical hybrid sigma-pressure coordinates reaching up to 9 hPa (24 km), and a semi-Lagrangian spectral advection scheme. The model contains a wide range of advanced physical

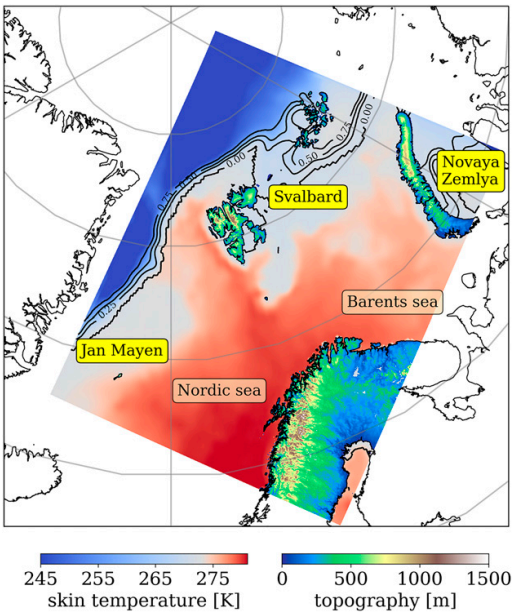

FIG. 1. The domain of the AROME-Arctic model. The shading over land indicates model topography, and the shading over water indicates skin temperature (K) from the control run (REF). Areas colder than 273 K are covered by sea ice. The skin temperature over water remains unchanged throughout the model run. The black contours indicate sea ice cover.

parameterization schemes, including cloud microphysics, radiation, surface processes, shallow convection, and turbulence, as detailed in the following.

The microphysics scheme (OCND2; Müller et al. 2017a) consists of three steps. First, during the microphysical adjustment step, thermodynamic equilibrium is enforced between the microphysical species and the temperature field. In the second step, the scheme calculates six prognostic variables: water vapor, cloud water, rain, ice, snow, and graupel. OCND2 thereby takes sublimation, evaporation, and interactions between species into account. Finally, the three-dimensional cloud fraction is diagnosed by a statistical cloud and condensation scheme (Bougeault 1982; Bechtold et al. 1995). OCND2 provides physical tendencies for water vapor, all hydrometeor species, and temperature.

The radiation scheme (RRTM; Fouquart and Bonnel 1980; Mlawer et al. 1997) provides radiative fluxes as input to the surface scheme and to the column temperatures. Shortwave radiation is computed using six spectral bands, while the longwave radiation is calculated by utilizing climatological distributions of aerosols and ozone. RRTM provides physical tendencies for temperature.

The surface scheme (SURFEX; Le Moigne 2009) provides sensible and latent heat fluxes as well as wind stress which are used by the turbulence and shallow convection scheme. SURFEX separates a grid box into four tiles (sea, lakes,

TABLE 1. Individual tendencies for temperature T and specific humidity R in the AROME-Arctic model utilized in this study.

Tendency	Scheme	Reference(s)
δT^{phys}, δR^{phys}	Total physical tendency, sum of all individual schemes	—
δT^{dyn}, δR^{dyn}	Dynamical tendency comprising the contributions from the model dynamics and the horizontal diffusion scheme	—
δT^{adj}, δR^{adj}	Thermodynamical adjustment step from microphysics	Müller et al. (2017a)
δT^{micro}, δR^{micro}	Cloud microphysics scheme, OCND2	Müller et al. (2017a)
δT^{turb}, δR^{turb}	TKE-turbulence scheme, HARATU	Lenderink and Holtslag (2004), Bengtsson et al. (2017)
δT^{sc}, δR^{sc}	Dual-updraft, shallow convection scheme	de Rooy and Siebesma (2008), Neggers et al. (2009)
δT^{EDMF}, δR^{EDMF}	Eddy-diffusivity mass-flux scheme, sum of turbulence and shallow convection	Soares et al. (2004), Siebesma et al. (2007)
δT^{rad}	Radiation scheme, RRTM	Fouquart and Bonnel (1980), Mlawer et al. (1997)

urban areas, nature), each represented by specific formulations. The total flux in each grid box is summed and weighted by its respective tile fractions. SURFEX further computes quantities like the surface albedo and emissivity which are then used by the radiation scheme. SURFEX does not directly contribute to the tendencies of temperature, moisture, or wind in the atmospheric model, but instead influences the tendencies provided by the boundary layer or the radiation scheme. Consequently, SURFEX does not appear as an individual process in the subsequent tendency analysis.

Finally, the boundary layer scheme is formulated using an eddy-diffusivity mass-flux framework (EDMF; Soares et al. 2004; Siebesma et al. 2007). The EDMF framework consists of two parts. The turbulence (''ED'') part is called HARMONIE-AROME with RACMO Turbulence (HARATU; Lenderink and Holtslag 2004; Bengtsson et al. 2017), and uses a prognostic equation for turbulent kinetic energy (TKE) together with a diagnostic length scale. For stable conditions, a generally accepted form of the length scale depending on the local stability is used (Deardorff 1980; Baas et al. 2008). For near-neutral to unstable conditions, the length scale consists of vertical integrals of stability-dependent functions (Lenderink and Holtslag 2004). The shallow convection part (''MF'') uses a dual updraft framework (Neggers et al. 2009). It distinguishes between dry updrafts that do not experience condensation and stop in close vicinity to the lifting condensation level, and moist updrafts that condense and form clouds. Both updrafts have different entrainment and detrainment rates (de Rooy and Siebesma 2008; Bengtsson et al. 2017; de Rooy et al. 2021, manuscript submitted to *Geosci. Model Dev.*, hereafter DR21). Each part of the EDMF scheme provides a physical tendency for temperature, humidity, and momentum.

The model configuration described above is used in our reference run (REF). REF contains one distinct difference from the operational configuration of AROME-Arctic at the time of this study: snow and rain produced by the shallow convection scheme are treated as resolved precipitation, which serves as input to the microphysics scheme. This setting (named LTOTPREC) is active for every model run discussed in this study. Positive impacts of this setting on mesoscale organization, prominent during an mCAO, have been found in preoperational tests for the model cycle 43 conducted at KNMI. The control run is initialized at 0000 UTC 24 December 2015 and was integrated for 72 h.

b. *Individual tendency output in AROME-Arctic*

We now briefly describe the implementation of individual tendency output as a new diagnostic in AROME-Arctic. A tendency refers to the change of a variable X over time. The absolute change in X between two succeeding time steps dX/dt is often called the total tendency and can be decomposed as follows:

$$\frac{dX}{dt} = D + K + \sum \delta X^i, \tag{1}$$

where D is the tendency due to the model dynamics, K is the tendency due to the horizontal diffusion, and $\sum \delta X^i$ is the sum of all individual physical tendencies, or the *total physical tendency*. The dynamical tendency represents advection, whereas the horizontal diffusion mainly smoothes the model fields to stabilize the dynamical core. In AROME-Arctic, both D and K are spectral computations, whereas the total physical tendency $\sum \delta X^i$ consists of gridpoint computations. Table 1 summarizes all individual tendencies for temperature and specific humidity that are output. In the AROME-Arctic model, the prognostic variables that are provided to the parameterization schemes are not influenced by the tendencies produced in the same time step. Thus, the order in which the schemes are called does not influence the individual tendencies. The only exception is the microphysical adjustment step (see above) that is performed at the very beginning of the physical package (Seity et al. 2011).

While the diagnosis and output of physical tendencies are straightforward, a problem arises for the dynamical and horizontal diffusive tendencies. In HARMONIE-AROME, the respective tendencies of the physical schemes are added to the prognostic variables before the dynamical routines are called (Seity et al. 2011). As a result, identifying the additional contributions coming from either the dynamics or horizontal diffusion within the same model time step, without risking double-counting contributions coming from the model physics, becomes impossible. Therefore, D and K are here obtained as a summed residuum from subtracting the physical tendency from

the total tendency of the previous time step. We call this residuum the *dynamical tendency* throughout this study. All obtained tendencies are Eulerian, accumulated over the hourly output interval of the model and provided at every model grid point and level.

c. *Boundary layer–type diagnostics*

An mCAO is accompanied by remarkable transformations of air masses, from stably stratified over sea ice–covered areas to a convective boundary layer over open water. The parameterization schemes need to be able to represent the varying characteristics of such differing regimes. For this reason, HARMONIE-AROME cy40.1.1 distinguishes between five planetary boundary layer (PBL) types (Fig. 2): stable PBL (I), dry convective (II), stratocumulus topped (III), shallow cumulus topped (IV), and deep convection (V). We now describe how the PBL types I–V are diagnosed, and how they influence the shallow convection scheme.

In the case of stable conditions, characterized by downward surface buoyancy flux as indicated by the idealized temperature profile (Fig. 2, type I), no convective transport can be expected and the PBL is diagnosed as type I (stable). In case of unstable conditions (Fig. 2, type II–V), convective transport becomes important, and dry and moist updrafts are calculated. These calculations require fractional entrainment rates that depend on the "inversion height" (Siebesma et al. 2007; DR21). However, this inversion height is not known a priori. Therefore, a test parcel is released, with an entrainment formulation that does not depend on inversion height, following Neggers et al. (2009) and Neggers (2009). The inversion height is determined as the height where the vertical velocity of a dry test parcel becomes 0, or if condensation occurs, set equal to the lifting condensation level. In the case of condensation, furthermore the cloud layer depth is estimated. These variables are subsequently used to distinguish between different convective PBL types.

If the test parcel does not reach the lifting condensation level (LCL; see Fig. 2, type II), the corresponding PBL type is of type II (dry convective) and only dry updrafts (yellow) occur. If the test parcel reaches the LCL, the PBL type is of type IV (shallow cumulus), and moist updrafts (blue) are possible. A further distinction is made if a strong inversion occurs (Fig. 2, type III) and $\theta_{700\text{hPa}} - \theta_{\text{surf}} > 20$ K (Klein and Hartmann 1993). In this case, the PBL type is set to type III (stratocumulus). With PBL type III, only moist updrafts occur, whereas both moist and dry updrafts occur with type IV. Finally, if the test parcel diagnoses a cloud layer depth that exceeds 4000 m, the PBL type is set to type V (deep convection). PBL type V

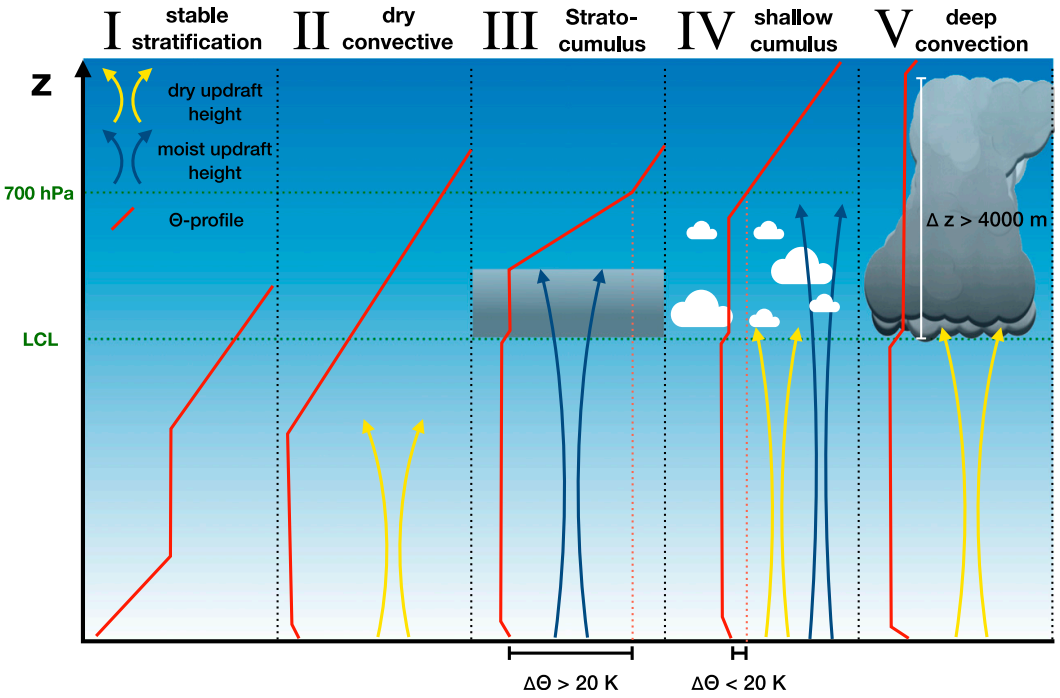

FIG. 2. Schematic showing the boundary layer types in HARMONIE-AROME and their implications for the shallow convection scheme. Idealized potential temperature profiles are shown in red. Yellow and blue arrows depict idealized dry and moist updrafts. The red stippled lines in III and IV indicate the differentiation criteria of Klein and Hartmann (1993). The green stippled lines indicate the lifting condensation level (LCL) and the 700-hPa level, respectively.

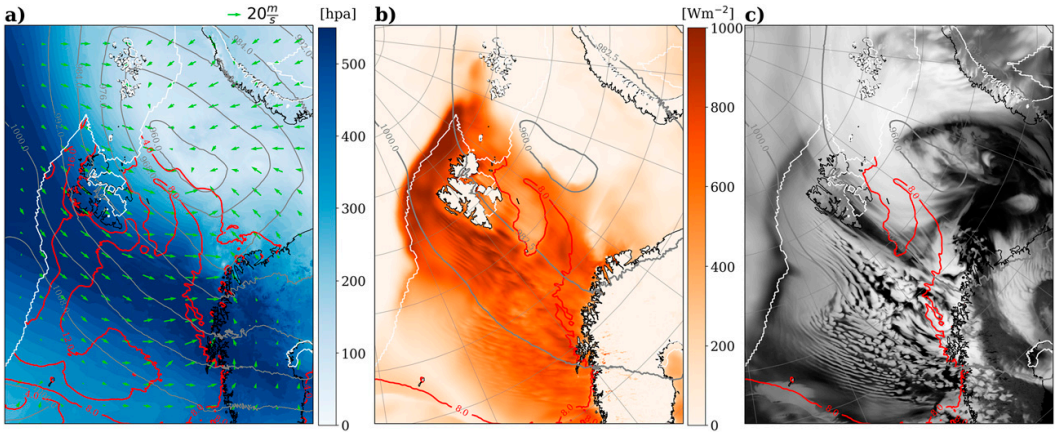

FIG. 3. Synoptic snapshots of the modeled marine cold air outbreak at 1200 UTC 26 Dec 2015 from the control run REF. (a) Thickness of the layer below the 280-K isentropic surface (cold air mass; hPa; blue shading), the CAO index ($\theta_{SST} - \theta_{900}$; K; red contour), the mean sea level pressure (hPa; gray contours), the 10-m winds (m s^{-1}; green arrows). (b) The sum of sensible and latent heat fluxes (W m^{-2}). (c) The top of the atmosphere outgoing longwave radiation as a proxy for cloud cover. Selected pressure contours (gray) in (b) and (c) indicate the prevalent surface trough, while the 8-K contour of the CAO index (red) indicate regions strongly affected by the mCAO. The sea ice edge is depicted in white.

assumes that the model resolves moist convection, and only dry convection remains parameterized.

The diagnosed PBL types directly influence the shallow convection scheme, and can also influence other parameterization schemes through various interplay. In our further analyses, we, therefore, need to consider these PBL types when investigating the behavior of individual tendencies.

d. The sensitivity experiments

To put the observed interplay of different parameterization schemes during the mCAO into perspective, we conduct two sensitivity experiments with altered model physics. Like REF, each experiment has a runtime of 72 h and starts at 0000 UTC 24 December 2015. Throughout this study, these experiments are referred to as NOSH and NEW, with the respective details given below.

For the sensitivity experiment NOSH, the shallow convection scheme is deactivated, impacting the partitioning between resolved and parameterized vertical transport. Changing this partitioning has profound impacts on the development of atmospheric profiles and boundary layer clouds during an mCAO in other model studies (Field et al. 2017; Tomassini et al. 2017).

Sensitivity experiment NEW contains several extensive changes to the physics that are being considered for future model versions (DR21). A thoroughly revised statistical cloud scheme is used. As a result of substantial modifications to the turbulence scheme, atmospheric inversions are better preserved. An additional TKE source term enables more ventilation between subcloud and cloudy layers by the turbulence scheme. This source term is referred to as the "energy cascade" and is driven by the mass flux. In the convection scheme, the susceptibility of the mass flux toward stronger sensible heat fluxes is increased to better capture the onset of diurnal convection by decreasing near-surface entrainment rates. Unlike NOSH, NEW is characterized by increased activity of the shallow convection scheme. In NEW, the stratocumulus PBL type (type III) has been eliminated.

e. The marine cold-air-outbreak case study

For our case study, we select an extensive mCAO event in the Fram Strait that developed on 24 December 2015 and lasted until 27 December 2015. Using water vapor tracers in the Consortium for Small-Scale Modeling (COSMO) model, Papritz and Sodemann (2018) found that this particular mCAO created its own water cycle with local evaporation, pronounced convective overturning in the PBL, and rapid precipitation formation. In addition to this event being exemplary for mCAOs in the Nordic seas, their results indicate a strong influence of the parameterization schemes on the simulation results.

We use two diagnostics to characterize the mCAO: the *CAO index* and the *cold air mass*. The CAO index is defined as the air–sea potential temperature difference between the surface and 900 hPa, allowing for delineation of an mCAO at the surface. The cold air mass describes the volume of air between the ground and a certain isentropic surface [280 K, similar to the average sea surface temperature, Papritz and Sodemann (2018)]. Air masses leaving the sea ice–covered areas while being located below that isentropic surface can contribute to the mCAO (Iwasaki et al. 2014). Provided that the correct isentropic surface is used, the cold air mass captures both the horizontal and vertical extent of the mCAO.

During the event, an extensive surface trough in the Nordic seas (gray contours, Fig. 3a) led to a persistent transport of cold air over the sea ice edge at low levels (green arrows). The CAO index (red contours) frequently exceeds 8 K, indicating a strong event. A dome of cold air (dark blue shading), extending up to 550 hPa, reaches from the sea ice edge (white line) across the Nordic Seas to northern Scandinavia. The emerging

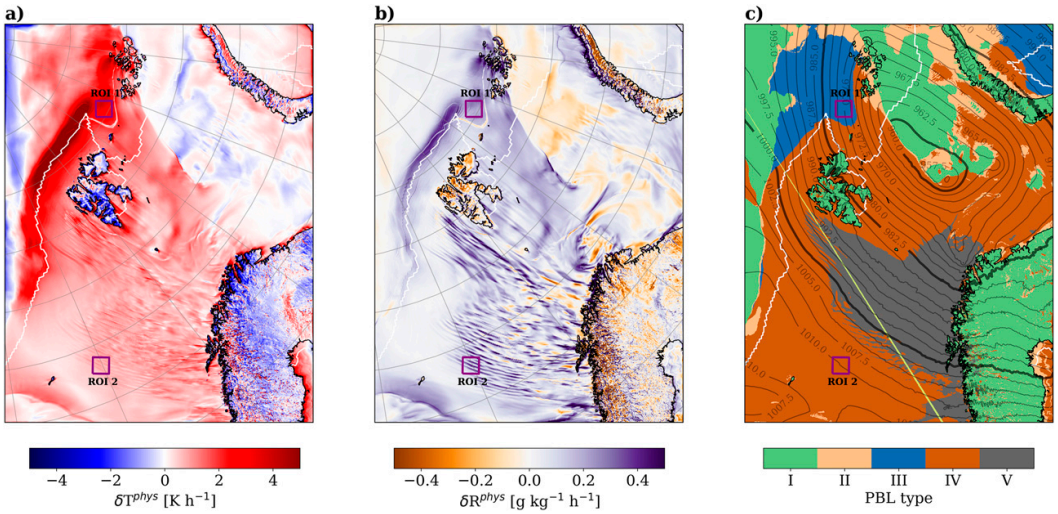

FIG. 4. (a) Physical tendency of temperature δT^{phys} (K h^{-1}) at the lowest model level. (b) Physical tendency of specific humidity δR^{phys} (g kg^{-1} h^{-1}) at the lowest model level. (c) Diagnosed boundary layer types in AROME-Arctic: stable stratification (I), dry convective (II), stratocumulus topped (III), shallow cumulus topped (IV), and deep convection (V). The displayed time is 1200 UTC 25 Dec 2015. Mean sea level pressure (hPa) is in black contours, and the white line indicates the sea ice edge. A north–south cross section (yellow line) is highlighted in (c), as well as two regions of interest (ROI; purple) used in the subsequent analysis in sections 3b and 3c.

gradients of temperature and moisture strongly impact the combined sensible and latent heat fluxes (Fig. 3b; Papritz and Sodemann 2018). Along the sea ice edge, turbulent heat fluxes exceed 1000 W m^{-2}, fueling vertical mixing and leading to extensive growth of the boundary layer (section 3b).

Cloud cover, depicted using outgoing longwave radiation (OLR) at the top of the atmosphere (TOA) as a proxy, shows a dense stratocumulus deck close to the sea ice edge between Svalbard and Jan Mayen (Fig. 3c). The stratocumulus deck breaks into cellular convection farther south over warmer sea surface temperatures, and convective rolls start to appear. We expect that interactions between resolved and subgrid processes are especially active in these regions, making them a focal point in the following investigation.

3. Results

a. The role of boundary layer types

First, we examine the total physical tendencies of temperature δT^{phys} and humidity δR^{phys} at the lowest model level. As the total physical tendency incorporates the contributions of every individual parameterization scheme [Eq. (1)], it helps to identify general patterns in the tendency output that might be linked to different interplays between the schemes. Most of the model domain affected by the mCAO (Fig. 3) exhibits positive values of δT^{phys} and δR^{phys} (Figs. 4a,b). Thus, the lowest model level is warmed and moistened by the model physics. This contribution is not uniform across the domain, and distinct spatial patterns emerge. These patterns align with the location of strong sensible heat fluxes (Fig. 3b) or are collocated to model internal PBL types (Fig. 4c).

Strong contributions from δT^{phys} occur along the sea ice edge (Fig. 4a, white line), collocated with the strong turbulent heat fluxes (cf. Fig. 3b). Here, δT^{phys} is largest with values near 5 K h^{-1}. Notably, large contributions occur ahead of the indicated sea ice edge because leads in the marginal ice zone permit high sensible heat fluxes.

An example of the dependency on PBL types exists both west and southwest of Svalbard, where a striped pattern in the physical tendencies is present, in particular for δR^{phys} (Fig. 4b). This pattern originates from partially resolved, mesoscale convection in the form of convective rolls (shown later). This convection occurs with the deep convective PBL type (Fig. 4c, Type V, gray shading), and farther south, also occurs with the shallow convective PBL type (Fig. 4c, Type IV, brown shading).

Cooling and drying predominately occur where the stable PBL type is present (Fig. 4c, Type I, green shading). These regions include all landmasses, parts of the sea ice covered area, and an area west of the Novaya Zemlya archipelago that is not affected by the mCAO.

Northeast of Svalbard, a pattern that resembles a nose emerges. Here, δT^{phys} neither warms nor cools the atmosphere, while all surrounding grid points display warming contributions. In a similar fashion, δR^{phys} exhibits a drying contribution here, while all surrounding grid points exhibit moistening. This pattern coincides with the transition from the stratocumulus (Type III, blue) to the shallow cumulus topped (Type IV, brown) PBL type (Fig. 4c). Thus, model-internal PBL types are important factors in near-surface temperature and moisture tendencies in the AROME-Arctic model.

b. Tendencies within the mCAO

To facilitate comparison with the sensitivity runs, we first describe the interplay of individual tendencies within the

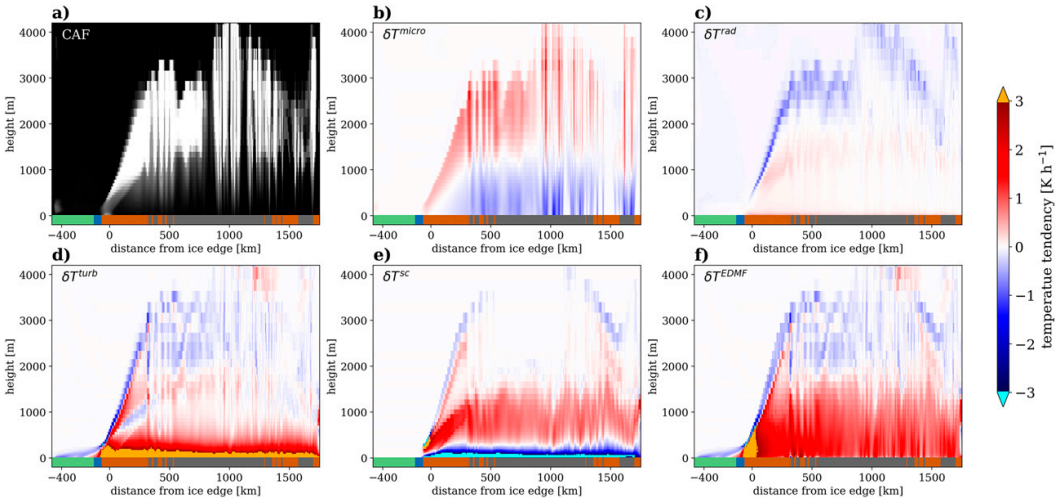

FIG. 5. Cloud area fraction (CAF) and single temperature tendencies along the north–south cross section indicated in Fig. 4c. The abscissa denotes distance from the sea ice edge in km. Ordinate denotes height in m. The panels show (a) CAF (0–1), (b) microphysics tendency δT^{micro} (from -1.5 to $1.8\,\text{K h}^{-1}$), (c) radiation tendency δT^{rad} (from -1.1 to $1.0\,\text{K h}^{-1}$), (d) turbulence tendency δT^{turb} (from -4.6 to $19.0\,\text{K h}^{-1}$), (e) shallow convection tendency δT^{sc} (from -16.5 to $5.6\,\text{K h}^{-1}$), and (f) EDMF-tendency δT^{EDMF} (from -8.6 to $7.1\,\text{K h}^{-1}$). At the bottom of each panel the diagnosed PBL type along the cross section is shown following the shading in Fig. 4c.

mCAO in REF. Throughout the mCAO, the PBL transforms rapidly, as evident from the differences in PBL types. A vertical cross-section, reaching from the stable PBL over sea ice and through the deep convective boundary layer west of Svalbard (Fig. 4c, yellow line) shows the growth of the PBL and individual tendencies within the mCAO (Fig. 5). As depicted by the zero cloud area fraction (CAF), no boundary layer clouds are simulated over most of the sea ice–covered areas (Fig. 5a, negative range of the abscissa). This changes with the onset of the shallow cumulus PBL type close to the sea ice edge. From there southward, boundary layer clouds develop and extend from around 500 to 3500 m. Approximately 400 km away from the sea ice edge, the PBL transitions to deep convective, accompanied by a breakup of cloud cover. This breakup first appears in form of equidistant cloud structures of similar size that emerge from convective rolls (Fig. 3b). Around 1000 km from the sea ice edge, smaller cloud structures emerge due to cellular convection.

The microphysics tendency δT^{micro} is consistently negative, indicating cooling, in all layers below cloud base, while being positive, indicating warming, in the cloud layers (Fig. 5b). The cooling comes from evaporation and sublimation, while the warming comes from condensation, freezing, and deposition (not shown), consistent with Joos and Wernli (2012). The LCL coincides with the transition from negative to positive contributions. The roll clouds and convective cells lead to pronounced warming of up to $3\,\text{K h}^{-1}$, due to increased transport of water vapor into these cloud features and a stronger release of latent heat by condensation and freezing (not shown).

The radiative tendency δT^{rad} displays distinct negative values near the cloud tops (Fig. 5c), caused by the different emissivities present within and above the cloud due to the change in water vapor and hydrometeor content. As the mCAO took place during the polar night, only longwave radiation contributes to δT^{rad}. Consequently, a radiative imbalance forms, locally cooling the atmosphere at about $-2\,\text{K h}^{-1}$. Minor radiative warming contributions exist in the lower half of the clouds and near the surface.

We now turn to the turbulence and shallow convection tendencies, δT^{turb} and δT^{sc}. Due to their strong interplay, these two tendencies should be regarded together. The δT^{turb} and δT^{sc} are substantially larger compared to all other contributing tendencies, especially near the surface (Figs. 5d,e). Over the sea ice, where a mix of stable and stratocumulus-topped PBL types is present, δT^{turb} is the only tendency with a notable contribution. In the stable PBL, δT^{turb} is negative, thus the turbulence parameterization cools the shallow PBL. With the onset of the stratocumulus-topped PBL type, small positive contributions of about $1\,\text{K h}^{-1}$ appear in the lowest 100 m of the atmosphere. Near the sea ice edge, in the marginal ice zone, a gradual increase in boundary layer height from 30 to 200 m occurs. With the onset of the shallow cumulus PBL type beyond the sea ice edge, the rate of boundary layer deepening rapidly increases. Here, δT^{turb} remains positive throughout most of the PBL, with a warming rate that reaches values of up to $19\,\text{K h}^{-1}$ near the surface. At the top of the PBL, this warming diminishes until δT^{turb} becomes negative, and the turbulence parameterization cools the atmosphere because the scheme mixes colder air upward into the inversion layer atop the PBL (Stull 1988).

The shallow convection scheme is inactive in the stable PBL (cf. Fig. 2, type I), and is largely idle in the stratocumulus PBL type (Fig. 5e). With the onset of the shallow cumulus PBL type, δT^{sc} exhibits large negative values up to $-16\,\text{K h}^{-1}$ in the

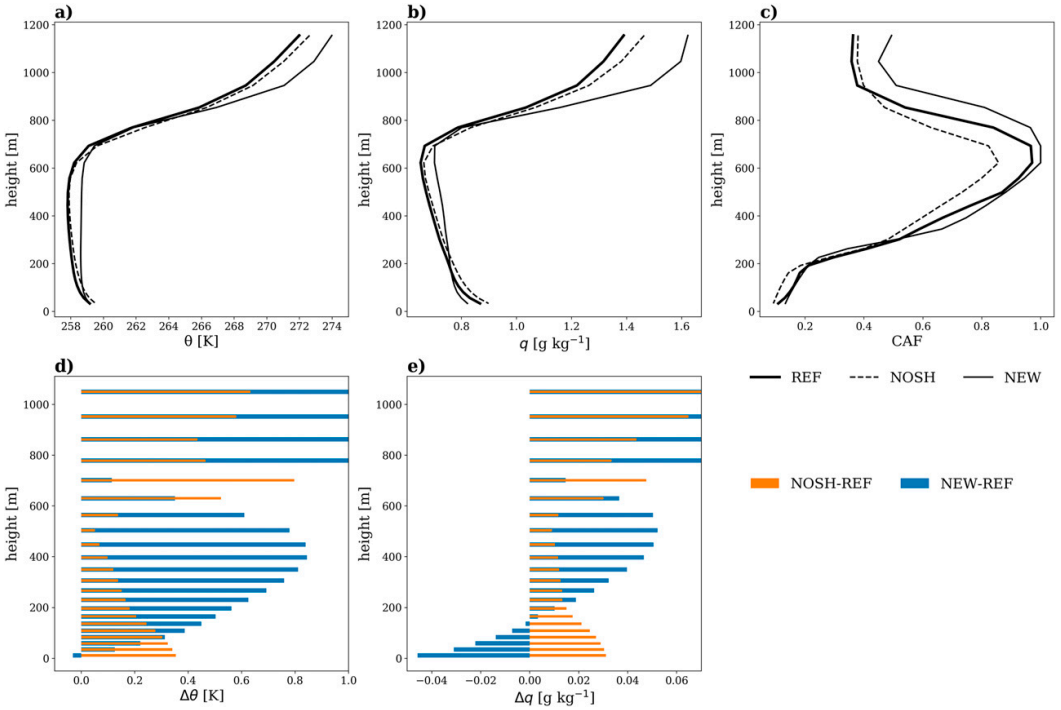

FIG. 6. Spatially averaged profiles within the stratocumulus ROI (ROI 1) of (a) potential temperature (K), (b) specific humidity ($g\,kg^{-1}$), and (c) cloud area fraction (CAF). The line styles refer to different sensitivity runs: REF (solid, thick), NOSH (dashed, thin), and NEW (solid, thin). Differences between the averaged profiles of (d) potential temperature, and (e) specific humidity between NOSH and REF (orange) and NEW and REF (blue).

lowest 200 m of the atmosphere, a significant cooling. At heights of about 200–300 m, a transition from negative to positive values, and thus from cooling to warming contributions of the scheme, occurs. From there upward, the shallow convection scheme warms the PBL at rates up to $3\,K\,h^{-1}$. Both cooling and warming result from the updrafts, which transport heat away from the surface and release it higher in the PBL. In the deep convective PBL type, only dry updrafts occur (Fig. 2, type V) leading to the abrupt cessation of δT^{sc} values around the cloud base height (~1500 m). Occasional values of δT^{sc} that differ from $0\,K\,h^{-1}$ inside the cloud layer within the deep convective PBL indicate a variation of PBL type during the accumulation interval of the tendency output (section 2b).

The two tendencies δT^{turb} and δT^{sc} can be combined into an EDMF tendency δT^{EDMF} (Fig. 5f). Throughout the boundary layer depth, δT^{EDMF} exhibits nearly constant vertical profiles of $1–3\,K\,h^{-1}$ with a maximum of over $5\,K\,h^{-1}$ near the sea ice edge. These constant EDMF profiles imply a compensation between the strong positive and negative contributions of δT^{turb} and δT^{sc} near the surface, while at higher levels, the positive contributions of both tendencies complement each other. For example, the transition from negative to positive values in δT^{sc} (Fig. 5e) between 200 and 300 m is not noticeable in δT^{EDMF}, because δT^{turb} decreases simultaneously (Fig. 5d). This decrease in δT^{turb} originates from the reduced vertical temperature gradients due to the warming of the shallow convection scheme. This interplay leads to a nearly constant δT^{EDMF} with height.

In summary, the individual tendency output reveals that δT^{micro}, δT^{turb}, and δT^{sc} are the most influential tendencies along the mCAO cross-section. The δT^{turb} and δT^{sc} strongly interact by compensating or complementing each other, forming the near-constant δT^{EDMF} with height. Furthermore, the contributions of δT^{EDMF} and δT^{micro} also compensate each other to a certain degree, especially in the deep convective PBL. These compensations between tendencies pose the question of how AROME-Arctic reacts to a change in its model physics configuration.

c. *Sensitivity experiments*

As shown above, tendency output from individual parameterization schemes reveals their compensating interplay within the mCAO, modulated by the diagnosed boundary layer types. Both of these aspects are now modified within the two sensitivity experiments, NOSH and NEW, described in section 2d.

We focus on two regions of interest (ROI, Fig. 4c), each covering an area of 40 × 40 grid points within a specific PBL type. ROI 1 ("stratocumulus" ROI) is located in the stratocumulus PBL type in both REF and NOSH. Large changes are

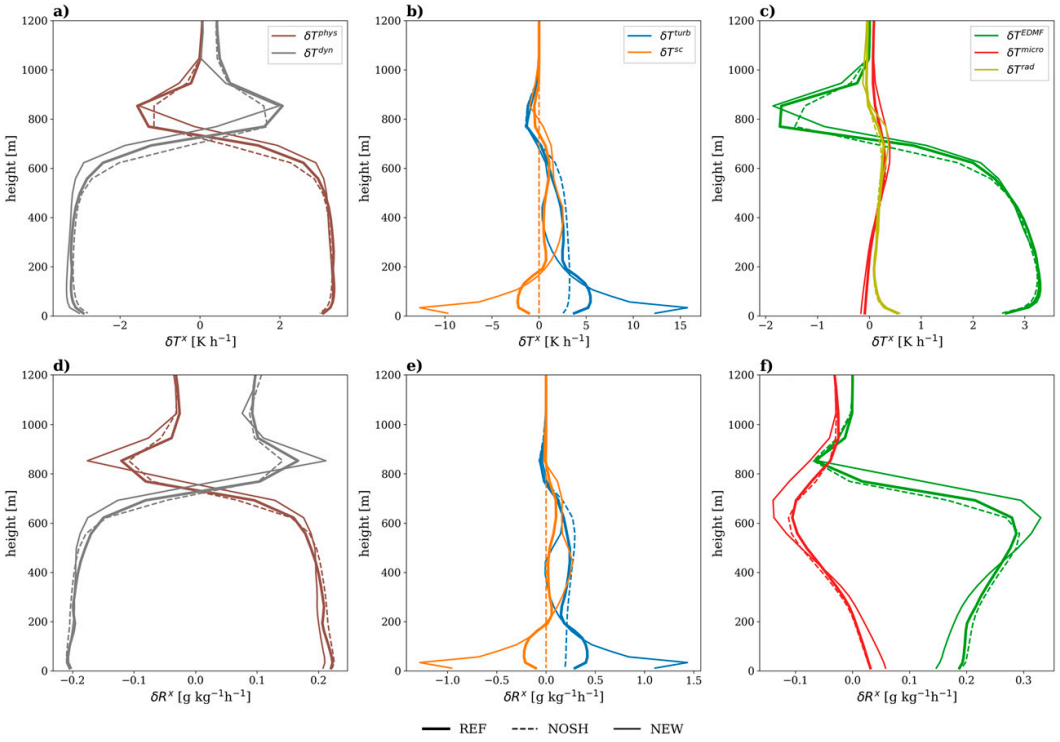

FIG. 7. Spatially averaged tendency profiles for the stratocumulus ROI (ROI 1). (a)–(c) Temperature tendencies (K h^{-1}) and (d)–(f) specific humidity tendencies (g kg^{-1} h^{-1}). The line colors denote different tendencies, physical (brown), dynamical (gray), turbulence (blue), shallow convection (orange), EDMF (green), microphysics (red), and radiation (yellow).

expected in NEW here because the stratocumulus PBL type is replaced by the shallow cumulus type. ROI 2 ("roll cloud" ROI) is located downstream of the mCAO (Fig. 3c). In this ROI, resolved convective motions are active in conjunction with parameterized shallow convection. Thus, the shallow convection scheme, which has been modified in both NOSH and NEW, plays a key role in ROI 2. For the sensitivity analysis within each ROI, averaged vertical profiles of selected variables and all major contributing tendencies for temperature and specific humidity are presented. For completeness, a brief analysis of two other ROIs, located in the stable and deep convective PBL type, can be found in the online supplemental material.

1) IMPACTS WITHIN THE STRATOCUMULUS ROI (ROI 1)

The averaged profiles of potential temperature depict a strong inversion in ROI 1 above 700 m at the same height in all three runs (Fig. 6a). While REF (solid, thick) and NOSH (dashed, thin) exhibit similar temperature and humidity profiles (Fig. 6b), NEW (solid, thin) exhibits more well-mixed atmospheric profiles throughout the PBL and a stronger inversion. Better preservation of atmospheric inversions is an expected result of the modified turbulence scheme in NEW.

The strong inversion in all runs is accompanied by stratocumulus-type clouds that spread from around 400 to 1000 m, with a maximum CAF around 600 m (Fig. 6c). NOSH exhibits the least cloud cover, and the thickest clouds are present in NEW.

The differences between the profiles in potential temperature and specific humidity of REF and NEW (Figs. 6d,e, blue) show a seamless transition from negative to positive differences in the lowest 600 m, confirming a more well-mixed PBL in NEW. The differences between NOSH and REF (orange) indicate a less well-mixed PBL in NOSH compared to REF. The lowest 200 m exhibit the largest differences, approaching 0.4 K (0.03 g kg^{-1}) and are collocated with the differences between shallow convection tendencies (see below).

Next, we investigate the tendencies of temperature and humidity in ROI 1 (Fig. 7). In all model runs, δT^{phys} and δR^{phys} are both positive from the surface through the middle of the cloud layer (600 m), reflecting net warming and moistening by the model physics (Figs. 7a,d). The tendencies δT^{dyn} and δR^{dyn} instead exhibit negative values in that layer. At heights between 700 and 1000 m, this relationship reverses due to cloud-top entrainment. Colder and drier air from within the PBL is

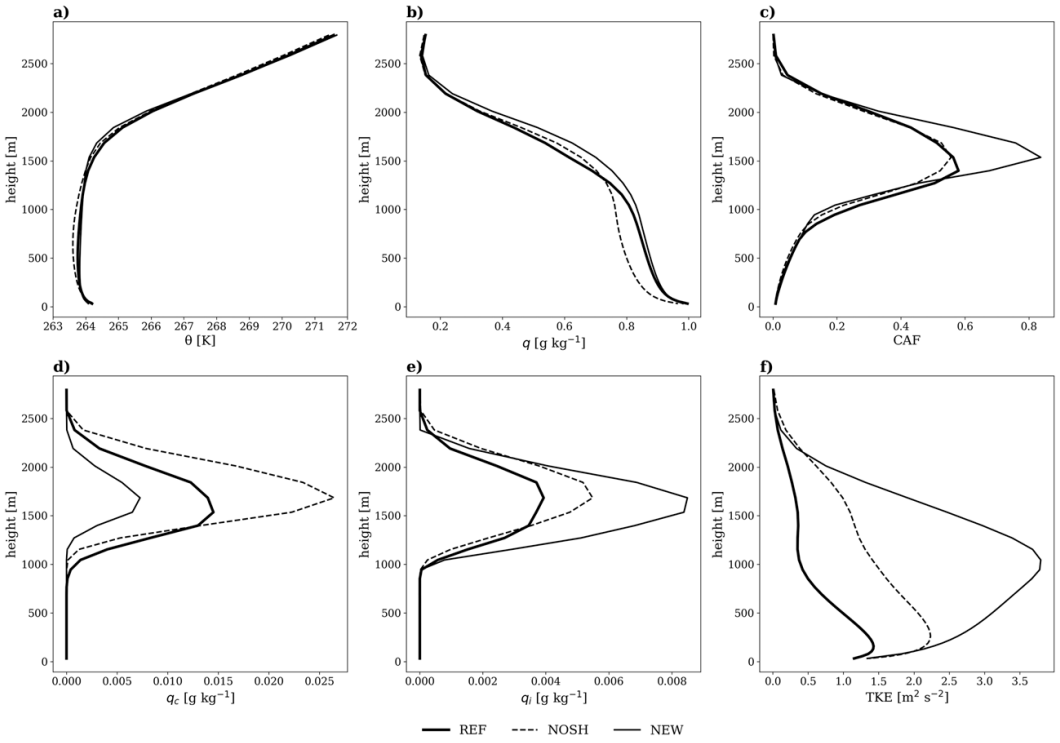

FIG. 8. Spatially averaged profiles within the roll cloud ROI (ROI 2) of (a) potential temperature (K), (b) specific humidity (g kg^{-1}), (c) cloud area fraction (CAF), (d) cloud water (g kg^{-1}), (e) cloud ice (g kg^{-1}), and (f) TKE (m^{-2} s^{-2}). The line styles refer to different sensitivity runs: REF (solid, thick), NOSH (dashed, thin), and NEW (solid, thin).

mixed upward into the inversion, substantiated by the negative contributions of δT^{turb}, δT^{sc}, δR^{turb}, and δR^{sc} (Figs. 7b,e). Meanwhile, warmer and more moist air is advected into the ROI at these heights. It is apparent that the physical and dynamical tendencies closely compensate each other in all runs.

Much larger sensitivities are found for δT^{turb} and δR^{turb}, as well as for δT^{sc} and δR^{sc} (Figs. 7b,e). In REF and NEW, δT^{sc} and δR^{sc} are both negative near the surface, but at varying magnitudes. In REF, these tendencies reach values of $-2\,\text{K}\,\text{h}^{-1}$ and $-0.1\,\text{g}\,\text{kg}^{-1}\,\text{h}^{-1}$, respectively, and exhibit an almost constant contribution below cloud base and within cloud layers (Fig. 6c). In comparison, δT^{turb} and δR^{turb} exhibit a similar shape, but reach higher absolute values of up to $5\,\text{K}\,\text{h}^{-1}$ ($0.4\,\text{g}\,\text{kg}^{-1}\,\text{h}^{-1}$). In NOSH, δT^{turb} and δR^{turb} instead exhibit near constant values of about $3\,\text{K}\,\text{h}^{-1}$ and $0.22\,\text{g}\,\text{kg}^{-1}\,\text{h}^{-1}$, respectively, for the lowest 600 m. Thus, the turbulence scheme consistently warms and moistens the lower PBL.

In NEW, contributions from the shallow convection scheme (δT^{sc} and δR^{sc}) reach values of $-12\,\text{K}\,\text{h}^{-1}$ and $-1\,\text{g}\,\text{kg}^{-1}\,\text{h}^{-1}$ near the surface, exceeding the tendencies in REF and NOSH by up to an order of magnitude. These strongly negative contributions below cloud base transition to positive contributions within the clouds (Fig. 6c). Contributions from the turbulence scheme (δT^{turb} and δR^{turb}, Figs. 7b,e) oppose that from the shallow convection scheme, showing large positive values near the surface that diminish with height. Thus, the shallow convection scheme in NEW contributes most to vertical mixing inside the cloud layer in ROI 1, opposite REF and NOSH, in which the turbulence scheme dominates the mixing process.

While each sensitivity experiment shows a distinct response in the contributions from the turbulence and the shallow convection schemes, the resulting δT^{EDMF} and δR^{EDMF} (Table 1) remain nearly unchanged between the runs (Figs. 7c,f, green). The similar EDMF profiles again underline the compensation between the turbulence and the shallow convection schemes. The biggest change is seen for δR^{EDMF} in NEW, as it exhibits a stronger gradient in the lowest 700 m. This gradient, however, is compensated by δR^{micro}, which is negatively correlated with δR^{EDMF}. In the end, this plethora of compensating tendencies results in the nearly unchanged δT^{phys} and δR^{phys} for ROI 1 between the different model runs (Figs. 7a,d). Furthermore, the unchanging EDMF tendencies in NOSH demonstrate that the role of the shallow convection scheme is taken over by the turbulence scheme in ROI 1.

Thus, neither replacing the stratocumulus with the shallow cumulus PBL type, as in NEW, nor removing the contribution

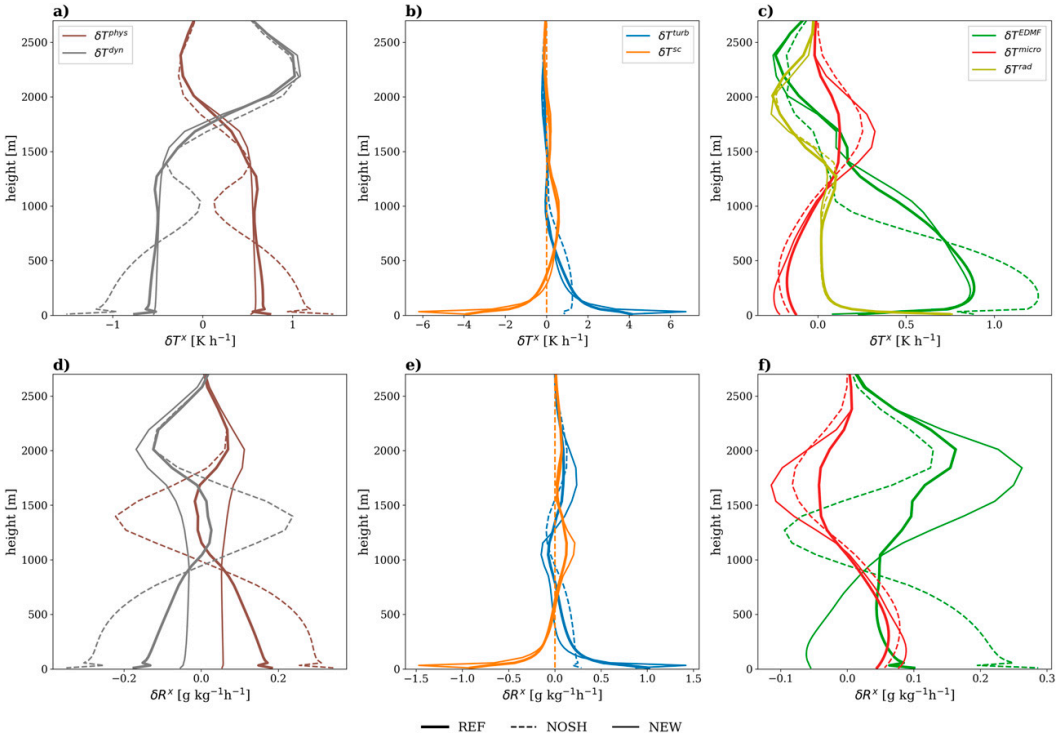

FIG. 9. Spatially averaged tendency profiles for the roll cloud ROI (ROI 2). (a)–(c) Temperature tendencies (K h^{-1}) and (d)–(f) specific humidity tendencies (g kg^{-1} h^{-1}). The line colors denote different tendencies, physical (brown), dynamical (gray), turbulence (blue), shallow convection (orange), EDMF (green), microphysics (red), and radiation (yellow).

from the shallow convection scheme, as in NOSH, results in substantial changes in either the temperature or specific humidity profiles in ROI 1, although the individual tendencies are substantially different in each simulation. One notable impact of the large contribution of the shallow convection scheme in NEW is that it yields the most well-mixed PBL of all runs (Figs. 6a,b). Furthermore, the differences between the temperature and specific humidity profiles (Figs. 6d,e) are collocated with differences between the respective contributions of the shallow convection scheme (Figs. 7b,e). Therefore, the individual tendencies allow us to decipher process-related differences between the model runs.

2) IMPACTS WITHIN THE ROLL CLOUD ROI (ROI 2)

Within the roll cloud ROI (ROI 2), the PBL and the cloud layer extend to about 2000 m. In REF, the temperature and humidity profiles are mostly between the profiles in NOSH and NEW (Figs. 8a,b). NOSH exhibits the least well-mixed profiles, while NEW, again, exhibits the most well-mixed profiles. The boundary layer clouds in all runs are located between 1000 and 2000 m (Fig. 8c). NEW again exhibits the most cloud cover, followed by REF and NOSH.

The modeled cloud condensate is quite sensitive to parameterization changes (Figs. 8d,e). REF shows mixed-phase clouds with a higher cloud water content (0.015 g kg^{-1}) than cloud ice content (0.004 g kg^{-1}). NOSH likewise exhibits mixed-phased clouds with the highest concentration of condensate, despite the lowest cloud fraction. The mass fraction of cloud water is nearly doubled (0.026 g kg^{-1}) in NOSH compared to REF. NEW, in contrast, exhibits the lowest amount of cloud water and the highest amount of cloud ice (0.0085 g kg^{-1}).

Substantial differences in TKE between the runs also occur (Fig. 8f). Both sensitivity runs depict higher values throughout the PBL compared to REF. NOSH has a nearly constant offset from REF above the lowest 150 m throughout the PBL. NEW has the highest TKE values of all runs, which continuously increase through cloud base (Fig. 8c). In NOSH, the less stable PBL causes increased buoyancy and shear production of TKE. In NEW, the increased values of TKE are the result of the addition of the energy cascade term to the TKE budget (DR21). This new source term enhances TKE in the upper half of the subcloud layer, thereby enhancing the turbulent transport between the subcloud and cloud layers.

The clearest impression of the model's response in the different simulations is given by δR^{dyn} (Fig. 9a, gray). In REF (solid, thick), δR^{dyn} is negative near the surface and below cloud base, indicating a drying contribution from the model dynamics. Meanwhile, the cloud layers (Fig. 8c) are moistened by the model dynamics, demonstrated by the positive values of

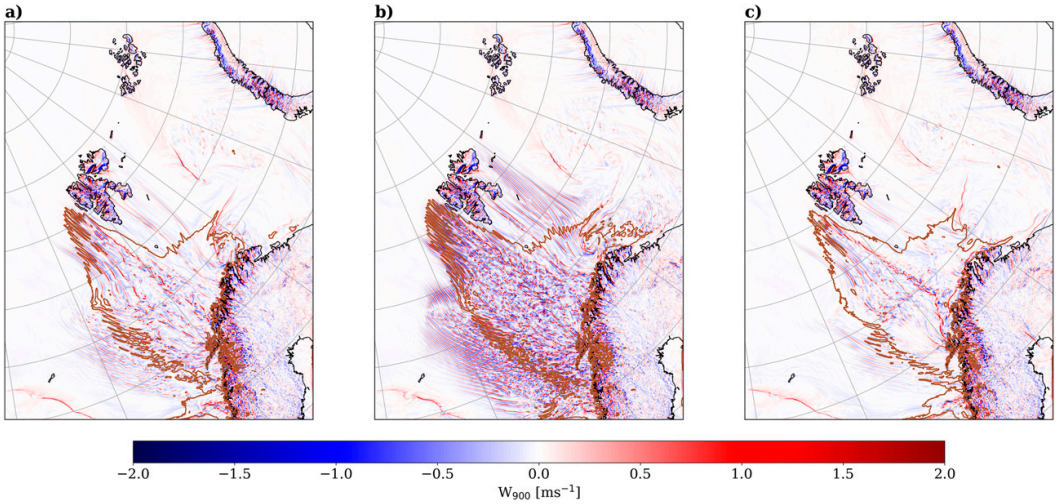

FIG. 10. Instantaneous vertical velocity (m s^{-1}) at 900 hPa valid at 1200 UTC 26 Dec 2015 for (a) REF, (b) NOSH, and (c) NEW. The brown contour depicts the onset of the deep convective PBL type in each experiment.

δR^{dyn}, similar to the shallow convection scheme. In NOSH (dashed), this resemblance is even more distinct. In contrast, such behavior is absent in NEW (solid, thin), in which δR^{dyn} shows a small, nearly constant negative contribution throughout the lowest 1700 m. Thus, the more or less active shallow convection scheme triggers a dynamical response of the model within the roll cloud ROI.

The EDMF tendency shows similar changes regarding the strength of the shallow convection scheme, exemplified here by δR^{EDMF} (Fig. 9f, green). Near the surface, there is a drying in NEW, whereas in REF and NOSH there is moistening. Tendencies in NOSH are more than twice as large as those in REF. In contrast to the other two simulations, NOSH exhibits a local minimum in δR^{EDMF} between 1000 and 1500 m before reaching a maximum around 2000 m. This local minimum coincides with the local maximum of δR^{dyn} in NOSH (Fig. 8d, gray, dashed), indicating that the air mixed upward by the parameterization is drier than the surrounding air. Thus, the vertical transport in NOSH is mostly done by the model dynamics on the grid-scale and not by the EDMF-framework, only represented by the turbulence scheme, on the subgrid-scale.

It thus appears that the turbulence scheme in NOSH is not able to compensate entirely for the missing shallow convection scheme in the roll cloud ROI, in contrast to the stratocumulus ROI (Figs. 7c,f). In turn, we find a strong dynamical response in NOSH that transports heat and moisture from near the surface to the subcloud and cloud layers (Fig. 9a), similar to a shallow convection scheme. With increasing strength of the shallow convection scheme, such a response is smaller in REF, and is largely absent in NEW.

d. Interaction of grid-scale and subgrid-scale processes

The dynamical responses of the model revealed above can be expected to be linked to the ratio between parameterized and resolved vertical transport in the PBL. Shallow convection mainly represents the parameterized transport while the grid-scale vertical velocity represents the resolved transport. We therefore investigate simulated vertical velocities, focusing on the 900-hPa level (Fig. 10).

Apart from orographic effects, only areas affected by the mCAO show strong vertical velocities in all simulations. REF primarily exhibits resolved vertical velocities within the deep convective PBL type (brown contour), but also farther south, including ROI 2. NOSH exhibits much stronger and widespread vertical velocities, which frequently exceed 2 m s^{-1}. Long bands of alternating updrafts and downdrafts can be seen, resembling convective rolls that often occur during an mCAO (Etling and Brown 1993). Farther south, near the Norwegian coast, these organized rolls break into cellular structures. While NEW depicts an overall reduction in vertical velocities, values of up to 2 m s^{-1} are present in the deep convective PBL type. The deep convective PBL appears distinct, as all vertical motions in the cloud layer must be resolved by the model. Nonetheless, the resolved convection in the deep convective PBL type in NEW is weaker than in REF. This indicates that the increased parameterized shallow convection until cloud base (see Fig. 2, type V), accompanied by a more well-mixed subcloud layer (Figs. 8a,b), reduces the buildup of intense resolved convection in NEW, otherwise present in REF. Hence, the response of the dynamical tendencies of NOSH and NEW (Figs. 9a,d) is manifested by the presence or absence of grid-scale updrafts.

Such pronounced changes in resolved vertical velocities can impact several other simulated quantities, regarding boundary layer clouds and their morphology, which enables a comparison with satellite imagery (Fig. 11). The satellite image (Fig. 11a) depicts cloud streets forming immediately downstream of the sea ice edge that transition into cellular convection around the latitude of Jan Mayen (see Fig. 1).

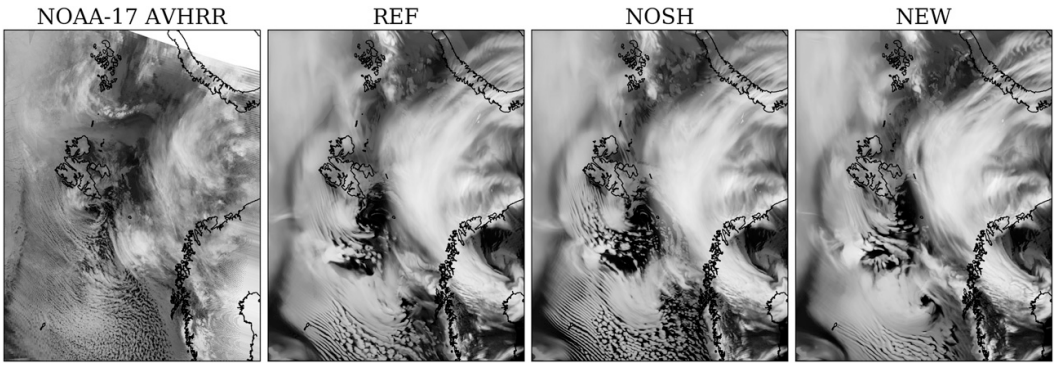

FIG. 11. (a) Infrared (channel 4) satellite image from the *NOAA-17* AVHRR instrument at 1935 UTC 25 Dec 2015. Outgoing longwave radiation (OLR) at the top of the atmosphere (TOA) in (b) REF, (c) NOSH, and (d) NEW at 1900 UTC 25 Dec 2015. Jan Mayen is the island in the bottom left.

In contrast to the satellite image, REF (Fig. 11b) only shows rudimentary cloud streets west of Svalbard and around Jan Mayen, which are often superimposed with stratiform clouds. Farther downstream, in good agreement with the observations, the cloud streets break into closed cells which, however, exceed the spatial extent of the observed convective cells. NOSH (Fig. 11c) depicts distinct cloud streets in close proximity to the sea ice edge, which break into smaller and more numerous individual cells than in REF. NOSH also produces cloud structures larger than those in the satellite image. Finally, NEW (Fig. 11d) displays the greatest cloud cover, with stratocumulus type clouds covering most of the mCAO. Cloud streets are barely visible south of Jan Mayen, and there is no breakup into single cells.

Thus, the changes to the shallow convection scheme in NOSH and NEW lead to a different partitioning of resolved and parameterized convection. As a result, substantial changes in vertical wind velocities emerge (Fig. 10), which in turn affect the representation of cloud condensates (Figs. 8d,e) and cloud morphology (Fig. 11) in AROME-Arctic.

4. Discussion

Individual tendency output has been utilized in this study to identify the governing parameterized processes and their interplay in an Arctic mCAO. Four aspects of the presented findings deserve a more detailed discussion, following below.

a. The role of model-internal boundary layer types

As revealed by ROI 1, PBL types can strongly modulate the interactions of individual parameterization schemes. The consideration of PBL types enables a more robust comparison of individual tendencies between different model runs because they inform about boundary conditions imposed on some schemes. PBL types are also commonly used in other NWP models, as they enable an adjustment of specific schemes to a wide range of different atmospheric situations, such as cloud-free nights, shallow cumulus convection, or, in our case, an mCAO. In the Integrated Forecast System model, for example, PBL types determine the use of the shallow convection or deep convection scheme (ECMWF 2013). It seems advisable that such model-internal PBL types be added as model output and be taken into account when investigating tendencies contributed by individual parameterizations.

b. The interplay of compensating parameterization schemes

The strong anticorrelation between the tendencies contributed by the turbulence and the shallow convection schemes is a central finding in our study (cf. Figs. 5, 7, 9). The turbulence scheme mixes locally down the gradient, whereas the shallow convection scheme acts nonlocally and draws its kinetic energy from buoyant production in the lower boundary layer (Lenderink and Holtslag 2004). Effectively, shallow convection transports heat and moisture away from the surface, thereby cooling and drying near-surface model levels. The turbulence scheme compensates for this effect by mixing heat and moisture from the surface upward down the vertical gradient.

Compensating behavior is also evident between the EDMF and microphysics, and the physical and dynamical tendencies in the convective boundary layer. The corresponding interplay was also found for several other NWP models (Niemelä and Fortelius 2005; Tomassini et al. 2017; Kim et al. 2018). Often only small residual terms remain from the very strong, opposing individual tendencies. This poses the question of whether such strong compensations could induce unwanted side effects. Regarding the common practice of model tuning, one can envision a scenario in which the contribution of parameterization scheme A is artificially enhanced, only because its contribution is constantly counteracted by another parameterization scheme. Such a condition could potentially hamper mid- and long-term model development.

Despite this compensation, the individual tendencies allow us to decipher process-related differences between the model runs. In ROI 1, the modeled profiles of temperature and specific humidity are different between the model runs (Figs. 6d,e). Both the warmer and more moist near-surface layer (200 m) in NOSH, as well as the better ventilation of the lowest 600 m in NEW are owing to differences in the shallow

convection scheme (Figs. 7b,e). Thus, individual tendencies aid in understanding differences between grid-scale atmospheric temperature or humidity profiles. Combining such analyses with observations, the tendency output could help to identify process-related errors within NWP models.

c. *Interacting subgrid- and grid-scale vertical transport*

The sensitivity experiments NOSH and NEW lead to opposite dynamical responses of the model, evidenced by the presence or absence of resolved vertical velocities (Fig. 10). These grid-scale updrafts indicate whether the EDMF framework fully accounts for the vertical mixing in the boundary layer (Figs. 7c,f) or not (Figs. 9c,f). NOSH enhances these grid-scale up- and downdrafts, while NEW largely suppresses them. Similar results were found in an LES study by Honnert et al. (2011), where the authors document an over and underestimation of resolved vertical motion in the respective absence or presence of a mass-flux scheme.

As demonstrated in this study, the relative strength of resolved versus parameterized convective transport depends on the convection scheme. The microphysics and the dynamical core, especially the strength of the horizontal diffusion, can also play a key role, however (Field et al. 2017). Downdrafts and cold pool mesoscale circulations originate from the evaporation of rain or snow and the associated cooling of the atmosphere. The setting LTOTPREC (see section 2a), used in all of our simulations, forwards the precipitation produced in the shallow convection scheme to the grid-scale condensates, used again by the microphysics. Thereby, LTOTPREC might act as a first step to establish a transfer from the parameterized to the resolved scales.

Clearly, the mCAO studied here differs substantially from other convective regimes, such as land-based, subgrid-scale shallow cumulus convection (e.g., Brown et al. 2002). During such regimes, the shallow convection scheme is essential for the convective transport. DR21, for example, note substantial drying of the subcloud layer by convection, captured better by NEW compared to REF. Herein lies a potential caveat for further model development: If one improves the model's performance for subgrid-scale shallow cumulus convection by increasing the parameterized, convective transport, one might simultaneously increase the need to reduce this convective transport during events that include partially resolved convection, such as the mCAO studied here.

d. *Change in cloud condensates*

The shift from liquid to ice condensates in NEW is unwanted (Figs. 8e,d). Arctic forecasts often suffer from an underrepresentation of supercooled liquid and mixed-phase clouds, while introducing ice condensates too frequently (Morrison et al. 2012; Engdahl et al. 2020). In our case study, the increase in ice condensates in NEW is connected to the treatment of resolved versus parameterized vertical motions. In regions over the open ocean and affected by the mCAO, cloud water only occurs in clouds that are directly fed by grid-scale vertical updrafts. In contrast, clouds that are solely fed by subgrid updrafts in REF and NEW consist of ice only. Thus, the absence of grid-scale updrafts in NEW (Fig. 10c) leads to the observed increase in cloud ice. In the same manner, the increase in cloud water in NOSH can be related to the more numerous grid-scale updrafts in that run. The mechanisms behind this shift in condensates together with the impact of the recent advancement in the microphysics scheme of AROME-Arctic, called ICE-T (Engdahl et al. 2020), will be investigated in a further study with the individual tendency output.

5. Conclusions and outlook

The simulation of an mCAO relies on the interplay of many parameterization schemes that contribute to forecast uncertainty, particularly in high latitudes. In this study, we demonstrated the utility of individual tendency output as a diagnostic tool in a regional, convection-permitting NWP model during a strong mCAO. We identify controlling factors for the activity of certain schemes, study the interplay between them, and investigate the model's subgrid adaption to changes in its physics package. We find that

- Analysis of individual tendencies strongly profits from considering modeled PBL types.
- Strong compensation between individual tendencies is prevalent. The same physical tendency for temperature and specific humidity may emerge from individual tendencies that can differ by up to an order of magnitude. Such compensating tendencies could lead to an artificial enhancement of individual schemes by model tuning and hamper model development.
- Despite similar physical tendencies for temperature and specific humidity, differences in atmospheric profiles do still occur. In the case studied here, these differences can be traced back to different individual tendencies. Future work could decipher the temporal development of the individual tendencies and their influence on atmospheric profiles, by enabling output at every single model time step.
- Considerable change in the interplay of individual tendencies and therefore in the resulting physical tendencies for temperature and specific humidity can be found when a dynamical response of the model is triggered by the sensitivity experiments. In our case study such a response can be identified by the presence or absence of grid-scale updrafts and downdrafts.
- In AROME-Arctic, clouds that are fed by resolved, grid-scale updrafts consist of both liquid and ice condensates, whereas clouds that are solely fed by parameterized updrafts consist of ice only. Therefore, the relationship between parameterized vertical transport, cloud morphology, and especially cloud condensates in AROME-Arctic should be more closely investigated.

Individual tendency output provides valuable insights into the workings of NWP models and helps to elaborate process-related changes to the model system. We agree with Lackmann and Thompson (2019) that many useful model fields provided by the physics routines, including individual tendencies, are often overlooked by the model community and advocate for a more widespread output and usage of such fields for continued model development.

Acknowledgments. We are very grateful for the constructive comments and insightful questions from the three anonymous reviewers that helped to substantially improve the manuscript. This work was funded by the Norwegian Research Council through the ALERTNESS project in the POLARPROG program (Project 280573).

Data availability statement. All model data that were created and used for this study are openly available from the THREDDS data server of the Norwegian Meteorological Institute (https://thredds.met.no/thredds/catalog/alertness/users/marvink/AMS_publication/catalog.html.).

REFERENCES

Abel, S. J., and Coauthors, 2017: The role of precipitation in controlling the transition from stratocumulus to cumulus clouds in a Northern Hemisphere cold-air outbreak. *J. Atmos. Sci.*, **74**, 2293–2314, https://doi.org/10.1175/JAS-D-16-0362.1.

Baas, P., S. R. de Roode, and G. Lenderink, 2008: The scaling behaviour of a turbulent kinetic energy closure model for stably stratified conditions. *Bound.-Layer Meteor.*, **127**, 17–36, https://doi.org/10.1007/s10546-007-9253-y.

Bechtold, P., J. W. M. Cuijpers, P. Mascart, and P. Trouilhet, 1995: Modeling of trade wind cumuli with a low-order turbulence model: Toward a unified description of Cu and Se clouds in meteorological models. *J. Atmos. Sci.*, **52**, 455–463, https://doi.org/10.1175/1520-0469(1995)052<0455:MOTWCW>2.0.CO;2.

Bengtsson, L., and Coauthors, 2017: The HARMONIE–AROME model configuration in the ALADIN–HIRLAM NWP system. *Mon. Wea. Rev.*, **145**, 1919–1935, https://doi.org/10.1175/MWR-D-16-0417.1.

Bougeault, P., 1982: Cloud-ensemble relations based on the gamma probability distribution for the higher-order models of the planetary boundary layer. *J. Atmos. Sci.*, **39**, 2691–2700, https://doi.org/10.1175/1520-0469(1982)039<2691:CERBOT>2.0.CO;2.

Brown, A. R., and Coauthors, 2002: Large-eddy simulation of the diurnal cycle of shallow cumulus convection over land. *Quart. J. Roy. Meteor. Soc.*, **128**, 1075–1093, https://doi.org/10.1256/003590002320373210.

Businger, S., and R. J. Reed, 1989: Cyclogenesis in cold air masses. *Wea. Forecasting*, **4**, 133–156, https://doi.org/10.1175/1520-0434(1989)004<0133:CICAM>2.0.CO;2.

de Rooy, W., and A. Siebesma, 2008: A simple parameterization for detrainment in shallow cumulus. *Mon. Wea. Rev.*, **136**, 560–576, https://doi.org/10.1175/2007MWR2201.1.

Deardorff, J. W., 1980: Stratocumulus-capped mixed layers derived from a three-dimensional model. *Bound.-Layer Meteor.*, **18**, 495–527, https://doi.org/10.1007/BF00119502.

ECMWF, 2013: IFS Documentation CY38R1—Part IV: Physical processes. No. 4, IFS Documentation CY38R1, ECMWF, https://doi.org/10.21957/vr0gh9gt9.

Engdahl, B. J. K., B. E. K. Nygaard, V. Losnedal, G. Thompson, and L. Bengtsson, 2020: Effects of the ICE-T microphysics scheme in HARMONIE–AROME on estimated ice loads on transmission lines. *Cold Reg. Sci. Technol.*, **179**, 103139, https://doi.org/10.1016/j.coldregions.2020.103139.

Etling, D., and R. A. Brown, 1993: Roll vortices in the planetary boundary layer: A review. *Bound.-Layer Meteor.*, **65**, 215–248, https://doi.org/10.1007/BF00705527.

Field, P. R., R. J. Cotton, K. McBeath, A. P. Lock, S. Webster, and R. P. Allan, 2014: Improving a convection-permitting model simulation of a cold air outbreak. *Quart. J. Roy. Meteor. Soc.*, **140**, 124–138, https://doi.org/10.1002/qj.2116.

——, and Coauthors, 2017: Exploring the convective grey zone with regional simulations of a cold air outbreak. *Quart. J. Roy. Meteor. Soc.*, **143**, 2537–2555, https://doi.org/10.1002/qj.3105.

Fouquart, Y., and B. Bonnel, 1980: Computations of solar heating of the Earth's atmosphere—A new parameterization. *Beitr. Phys. Atmos.*, **53**, 35–62.

Grossman, R. L., and A. K. Betts, 1990: Air–sea interaction during an extreme cold air outbreak from the eastern coast of the United States. *Mon. Wea. Rev.*, **118**, 324–342, https://doi.org/10.1175/1520-0493(1990)118<0324:AIDAEC>2.0.CO;2.

Hartmann, J., C. Kottmeier, and S. Raasch, 1997: Roll vortices and boundary-layer development during a cold air outbreak. *Bound.-Layer Meteor.*, **84**, 45–65, https://doi.org/10.1023/A:1000392931768.

Holloway, C. E., and Coauthors, 2014: Understanding and representing atmospheric convection across scales: Recommendations from the meeting held at Dartington Hall, Devon, UK, 28–30 January 2013. *Atmos. Sci. Lett.*, **15**, 348–353, https://doi.org/10.1002/asl2.508.

Honnert, R., V. Masson, and F. Couvreux, 2011: A diagnostic for evaluating the representation of turbulence in atmospheric models at the kilometric scale. *J. Atmos. Sci.*, **68**, 3112–3131, https://doi.org/10.1175/JAS-D-11-061.1.

Iwasaki, T., T. Shoji, Y. Kanno, M. Sawada, M. Ujiie, and K. Takaya, 2014: Isentropic analysis of polar cold airmass streams in the Northern Hemispheric winter. *J. Atmos. Sci.*, **71**, 2230–2243, https://doi.org/10.1175/JAS-D-13-058.1.

Joos, H., and H. Wernli, 2012: Influence of microphysical processes on the potential vorticity development in a warm conveyor belt: A case-study with the limited-area model COSMO. *Quart. J. Roy. Meteor. Soc.*, **138**, 407–418, https://doi.org/10.1002/qj.934.

Kim, J.-E.., C. Zhang, G. N. Kiladis, and P. Bechtold, 2018: Heating and moistening of the MJO during DYNAMO in ECMWF reforecasts. *J. Atmos. Sci.*, **75**, 1429–1452, https://doi.org/10.1175/JAS-D-17-0170.1.

Klein, S. A., and D. L. Hartmann, 1993: The seasonal cycle of low stratiform clouds. *J. Climate*, **6**, 1587–1606, https://doi.org/10.1175/1520-0442(1993)006<1587:TSCOLS>2.0.CO;2.

Lackmann, G. M., and G. Thompson, 2019: Hydrometeor lofting and mesoscale snowbands. *Mon. Wea. Rev.*, **147**, 3879–3899, https://doi.org/10.1175/MWR-D-19-0036.1.

Le Moigne, P., 2009: SURFEX scientific documentation. CNRM Tech. Rep., 211 pp.

Lenderink, G., and A. A. M. Holtslag, 2004: An updated length-scale formulation for turbulent mixing in clear and cloudy boundary layers. *Quart. J. Roy. Meteor. Soc.*, **130**, 3405–3427, https://doi.org/10.1256/qj.03.117.

Mlawer, E. J., S. J. Taubman, P. D. Brown, M. J. Iacono, and S. A. Clough, 1997: Radiative transfer for inhomogeneous atmospheres: RRTM, a validated correlated-k model for the longwave. *J. Geophys. Res.*, **102**, 16 663–16 682, https://doi.org/10.1029/97JD00237.

Morrison, H., G. de Boer, G. Feingold, J. Harrington, M. D. Shupe, and K. Sulia, 2012: Resilience of persistent Arctic mixed-phase clouds. *Nat. Geosci.*, **5**, 11–17, https://doi.org/10.1038/ngeo1332.

Müller, M., Y. Batrak, J. Kristiansen, M. Køltzow, G. Noer, and A. Korosov, 2017a: Characteristics of a convective-scale weather forecasting system for the European Arctic. *Mon. Wea. Rev.*, **145**, 4771–4787, https://doi.org/10.1175/MWR-D-17-0194.1.

——, and Coauthors, 2017b: AROME-MetCoOp: A Nordic convective-scale operational weather prediction model. *Wea. Forecasting*, **32**, 609–627, https://doi.org/10.1175/WAF-D-16-0099.1.

Neggers, R., 2009: A dual mass flux framework for boundary layer convection. Part II: Clouds., *J. Atmos. Sci.*, **66**, 1489–1506, https://doi.org/10.1175/2008JAS2636.1.

——, M. Köhler, and A. Beljaars, 2009: A dual mass flux framework for boundary layer convection. Part I: Transport. *J. Atmos. Sci.*, **66**, 1465–1487, https://doi.org/10.1175/2008JAS2635.1.

Niemelä, S., and C. Fortelius, 2005: Applicability of large-scale convection and condensation parameterization to meso-*y*-scale HIRLAM: A case study of a convective event. *Mon. Wea. Rev.*, **133**, 2422–2435, https://doi.org/10.1175/MWR2981.1.

Papritz, L., and S. Pfahl, 2016: Importance of latent heating in mesocyclones for the decay of cold air outbreaks: A numerical process study from the Pacific sector of the Southern Ocean. *Mon. Wea. Rev.*, **144**, 315–336, https://doi.org/10.1175/MWR-D-15-0268.1.

——, and H. Sodemann, 2018: Characterizing the local and intense water cycle during a cold air outbreak in the Nordic Seas. *Mon. Wea. Rev.*, **146**, 3567–3588, https://doi.org/10.1175/MWR-D-18-0172.1.

Samuelsen, E. M., and R. G. Graversen, 2019: Weather situation during observed ship-icing events off the coast of northern Norway and the Svalbard archipelago. *Wea. Climate Extremes*, **24**, 100200, https://doi.org/10.1016/j.wace.2019.100200.

Seity, Y., P. Brousseau, S. Malardel, G. Hello, P. Bénard, F. Bouttier, C. Lac, and V. Masson, 2011: The AROME-France convective-scale operational model. *Mon. Wea. Rev.*, **139**, 976–991, https://doi.org/10.1175/2010MWR3425.1.

Siebesma, A., P. Soares, and J. Teixeira, 2007: A combined eddy-diffusivity mass-flux approach for the convective boundary layer. *J. Atmos. Sci.*, **64**, 1230–1248, https://doi.org/10.1175/JAS3888.1.

Soares, P. M. M., P. M. A. Miranda, A. P. Siebesma, and J. Teixeira, 2004: An eddy-diffusivity/mass-flux parametrization for dry and shallow cumulus convection. *Quart. J. Roy. Meteor. Soc.*, **130**, 3365–3383, https://doi.org/10.1256/qj.03.223.

Stull, R. B., 1988: *An Introduction to Boundary Layer Meteorology*. Springer, 670 pp.

Tomassini, L., P. R. Field, R. Honnert, S. Malardel, R. McTaggart-Cowan, K. Saitou, A. T. Noda, and A. Seifert, 2017: The ''grey zone'' cold air outbreak global model intercomparison: A cross evaluation using large-eddy simulations. *J. Adv. Model. Earth Syst.*, **9**, 39–64, https://doi.org/10.1002/2016MS000822.

Vihma, T., and Coauthors, 2014: Advances in understanding and parameterization of small-scale physical processes in the marine Arctic climate system: A review. *Atmos. Chem. Phys.*, **14**, 9403–9450, https://doi.org/10.5194/acp-14-9403-2014.

Bibliography

Abbe, C. (1901), The Physical Basis of Long-Range Weather Forecasts, *Monthly Weather Review*, *29*(12), 551 – 561, doi:10.1175/1520-0493(1901)29[551c:TPBOLW]2.0.CO;2. 2

Arduini, G., G. Balsamo, E. Dutra, J. J. Day, I. Sandu, S. Boussetta, and T. Haiden (2019), Impact of a multi-layer snow scheme on near-surface weather forecasts, *Journal of Advances in Modeling Earth Systems*, *11*(12), 4687–4710, doi:https://doi.org/10.1029/2019MS001725. 6

Atlaskin, E., and T. Vihma (2012), Evaluation of NWP results for wintertime nocturnal boundary-layer temperatures over Europe and Finland, *Quarterly Journal of the Royal Meteorological Society*, *138*(667), 1440–1451, doi:https://doi.org/10.1002/qj.1885. 38

Baas, P., S. R. de Roode, and G. Lenderink (2008), The scaling behaviour of a turbulent kinetic energy closure model for stably stratified conditions, *Boundary-Layer Meteorology*, *127*(1), 17–36, doi:10.1007/s10546-007-9253-y. 16, 37

Bauer, P., A. Thorpe, and G. Brunet (2015), The quiet revolution of numerical weather prediction, *Nature*, *525*(7567), 47–55, doi:10.1038/nature14956. 1

Bechtold, P., J. W. M. Cuijpers, P. Mascart, and P. Trouilhet (1995), Modeling of Trade Wind Cumuli with a Low-Order Turbulence Model: Toward a Unified Description of Cu and Se Clouds in Meteorological Models, *Journal of the Atmospheric Sciences*, *52*(4), 455–463, doi:10.1175/1520-0469(1995)052<0455:MOTWCW>2.0.CO;2. 11

Beesley, J. A., C. S. Bretherton, C. Jakob, E. L. Andreas, J. M. Intrieri, and T. A. Uttal (2000), A comparison of cloud and boundary layer variables in the ECMWF forecast model with observations at Surface Heat Budget of the Arctic Ocean (SHEBA) ice camp, *Journal of Geophysical Research: Atmospheres*, *105*(D10), 12,337–12,349, doi:https://doi.org/10.1029/2000JD900079. 6

Bengtsson, L., S. Tijm, F. Váňa, and G. Svensson (2012), Impact of flow-dependent horizontal diffusion on resolved convection in arome, *Journal of Applied Meteorology and Climatology*, *51*(1), 54 – 67, doi:10.1175/JAMC-D-11-032.1. 11

Bengtsson, L., U. Andrae, T. Aspelien, Y. Batrak, J. Calvo, W. de Rooy, E. Gleeson, B. Hansen-Sass, M. Homleid, M. Hortal, K.-I. Ivarsson, G. Lenderink, S. Niemelä, K. P. Nielsen, J. Onvlee, L. Rontu, P. Samuelsson, D. S. Muñoz, A. Subias, S. Tijm, V. Toll, X. Yang, and M. O. Koltzow (2017), The HARMONIE–AROME Model Configuration in the ALADIN–HIRLAM NWP System, *Mon. Wea. Rev.*, *145*(5), 1919–1935, doi:10.1175/MWR-D-16-0417.1. 9, 16

Bjerknes, V. (1904), Das Problem der Wettervorhersage, betrachtet vom Standpunkt der Mechanik und Physik, *Meteorologische Zeitschrift*, *21*, 1–7. 2

Boone, A., and P. Etchevers (2001), An intercomparison of three snow schemes of varying complexity coupled to the same land surface model: Local-scale evaluation at an alpine site, *Journal of Hydrometeorology*, *2*(4), 374 – 394, doi:10.1175/1525-7541(2001)002<0374:AIOTSS>2.0.CO;2. 6

Boone, A., P. Samuelsson, S. Gollvik, A. Napoly, L. Jarlan, E. Brun, and B. Decharme (2017), The interactions between soil–biosphere–atmosphere land surface model with a multi-energy balance (ISBA-MEB) option in SURFEXv8 – Part 1: Model description, *Geoscientific Model Development*, *10*(2), 843–872, doi:10.5194/gmd-10-843-2017. 6

Bougeault, P. (1982), Cloud-Ensemble Relations Based on the Gamma Probability Distribution for the Higher-Order Models of the Planetary Boundary Layer, *Journal of the Atmospheric Sciences*, *39*(12), 2691–2700, doi:10.1175/1520-0469(1982)039<2691:CERBOT>2.0.CO;2. 11

Brümmer, B. (1996), Boundary-layer modification in wintertime cold-air outbreaks from the Arctic sea ice, *Boundary-Layer Meteorology*, *80*(1), 109–125, doi:10.1007/BF00119014. 5

Buizza, R., M. Milleer, and T. N. Palmer (1999), Stochastic representation of model uncertainties in the ECMWF ensemble prediction system, *Quarterly Journal of the Royal Meteorological Society*, *125*(560), 2887–2908, doi:https://doi.org/10.1002/qj.49712556006. 41

Bénard, P., J. Vivoda, J. Mašek, P. Smolíková, K. Yessad, C. Smith, R. Brožková, and J.-F. Geleyn (2010), Dynamical kernel of the Aladin–NH spectral limited-area model: Revised formulation and sensitivity experiments, *Quarterly Journal of the Royal Meteorological Society*, *136*(646), 155–169, doi:https://doi.org/10.1002/qj.522. 9

Casati, B., T. Haiden, B. Brown, P. Nurmi, and J.-F. Lemieux (2017), Verification of Environmental Prediction in Polar Regions: Recommendations for the Year of Polar Prediction, *WWRP 2017 – 1.* 1

Cavallo, S. M., J. Berner, and C. Snyder (2016), Diagnosing Model Errors from Time-Averaged Tendencies in the Weather Research and Forecasting (WRF) Model, *Monthly Weather Review*, *144*(2), 759 – 779, doi:10.1175/MWR-D-15-0120.1. 21

Christensen, H. M., I. M. Moroz, and T. N. Palmer (2015), Stochastic and Perturbed Parameter Representations of Model Uncertainty in Convection Parameterization, *Journal of the Atmospheric Sciences*, *72*(6), 2525–2544, doi:10.1175/JAS-D-14-0250.1. 4

de Rooy, W., and A. Siebesma (2008), A Simple Parameterization for Detrainment in Shallow Cumulus, *Mon. Wea. Rev*, *136*, 560–576, doi:10.1175/2007MWR2201.1. 18

de Rooy, W. C., P. Siebesma, P. Baas, G. Lenderink, S. R. de Roode, H. de Vries, E. van Meijgaard, J. F. Meirink, S. Tijm, and B. van 't Veen (2022), Model development in practice: a comprehensive update to the boundary layer schemes in HARMONIE-AROME cycle 40, *Geoscientific Model Development*, *15*(4), 1513–1543, doi:10.5194/gmd-15-1513-2022. 4, 5, 18, 19, 37, 39

Deardorff, J. W. (1966), The Counter-Gradient Heat Flux in the Lower Atmosphere and in the Laboratory, *Journal of Atmospheric Sciences*, *23*(5), 503 – 506, doi:10.1175/1520-0469(1966)023<0503:TCGHFI>2.0.CO;2. 16

Deardorff, J. W. (1980), Stratocumulus-Capped Mixed Layers Derived from a Three-Dimensional Model, *Boundary-Layer Meteorology*, *18*(4), 495–527, doi:10.1007/BF00119502. 16

Deng, A., and D. R. Stauffer (2006), On Improving 4-km Mesoscale Model Simulations, *Journal of Applied Meteorology and Climatology*, *45*(3), 361–381, doi:10.1175/JAM2341.1. 40

Derbyshire, S. H. (1999), Boundary-Layer Decoupling over Cold Surfaces as a Physical Boundary-Instability, *Boundary-Layer Meteorology*, *90*(2), 297–325, doi:10.1023/A:1001710014316. 6, 31

Done, J., C. A. Davis, and M. Weisman (2004), The next generation of NWP: explicit forecasts of convection using the weather research and forecasting (WRF) model, *Atmospheric Science Letters*, *5*(6), 110–117, doi:10.1002/asl.72. 40

Donier, S. Y., S. Faroux, and V. Masson (2012), Evaluation of the impact of the use of the ECOCLIMAP2 database on AROME operational forecasts, *Météo-France Tech. Rep*, p. 89. 15

Douville, H., J. F. Royer, and J. F. Mahfouf (1995a), A new snow parameterization for the Météo-France climate model, *Climate Dynamics*, *12*(1), 21–35, doi:10.1007/BF00208760. 13

Douville, H., J. F. Royer, and J. F. Mahfouf (1995b), A new snow parameterization for the Météo-France climate model, *Climate Dynamics*, *12*(1), 37–52, doi:10.1007/BF00208761. 13

Duscha, C., C. Barrell, I. A. Renfrew, I. M. Brooks, H. Sodemann, and J. Reuder (2022), A Ship-Based Characterization of Coherent Boundary-Layer Structures Over the Lifecycle of a Marine Cold-Air Outbreak, *Boundary-Layer Meteorology*, *183*(3), 355–380, doi:10.1007/s10546-022-00692-y. 5

Edwards, J. M. (2009a), Radiative Processes in the Stable Boundary Layer: Part I. Radiative Aspects, *Boundary-Layer Meteorology*, *131*(2), 105, doi:10.1007/s10546-009-9364-8. 6, 37

Edwards, J. M. (2009b), Radiative Processes in the Stable Boundary Layer: Part II. The Development of the Nocturnal Boundary Layer, *Boundary-Layer Meteorology*, *131*(2), 127–146, doi:10.1007/s10546-009-9363-9. 21

Emmerson, C., and G. Lahn (2012), Arctic opening: Opportunity and risk in the high north, *Chatham House-Lloyd's Risk Insight Rep.*, p. 59 pp. 1

Engdahl, B. J. K., G. Thompson, and L. Bengtsson (2020), Improving the Representation of Supercooled Liquid Water in the HARMONIE-AROME Weather Forecast Model, *Tellus A: Dynamic Meteorology and Oceanography*, *72*(1), 1–18, doi:10.1080/16000870.2019.1697603. 5, 37

Esau, I., M. Tolstykh, R. Fadeev, V. Shashkin, S. Makhnorylova, V. Miles, and V. Melnikov (2018), Systematic errors in northern Eurasian short-term weather forecasts induced by atmospheric boundary layer thickness, *Environmental Research Letters*, *13*(12), 125,009, doi:10.1088/1748-9326/aaecfb. 6, 38, 39

Etling, D., and R. A. Brown (1993), Roll Vortices in the Planetary Boundary Layer: A Review, *Boundary-Layer Meteorology*, *65*(3), 215–248, doi:10.1007/BF00705527. 5

Faroux, S., A. T. Kaptué Tchuenté, J.-L. Roujean, V. Masson, E. Martin, and P. Le Moigne (2013), ECOCLIMAP-II/Europe: a twofold database of ecosystems and surface parameters at 1 km resolution based on satellite information for use in land surface, meteorological and climate models, *Geoscientific Model Development*, *6*(2), 563–582, doi:10.5194/gmd-6-563-2013. 13

Field, P. R., R. Brozková, M. Chen, J. Dudhia, C. Lac, T. Hara, R. Honnert, J. Olson, P. Siebesma, S. de Roode, L. Tomassini, A. Hill, and R. McTaggart-Cowan (2017), Exploring the convective grey zone with regional simulations of a cold air outbreak, *Quarterly Journal of the Royal Meteorological Society*, *143*(707), 2537–2555. 5, 40

Fouquart, Y., and B. Bonnel (1980), Computations of Solar Heating of the Earth's Atmosphere - A New Parameterization, *Beitr. Phys. Atmos.*, *53*, 35–62. 12

Frogner, I.-L., A. Singleton, M. Køltzow, and U. Andrae (2019a), Convection-permitting ensembles: Challenges related to their design and use, *Quarterly Journal of the Royal Meteorological Society*, *145*(S1), 90–106, doi:https://doi.org/10.1002/qj.3525. 6

Frogner, I.-L., U. Andrae, J. Bojarova, A. Callado, P. Escribà, H. Feddersen, A. Hally, J. Kauhanen, R. Randriamampianina, A. Singleton, G. Smet, S. van der Veen, and O. Vignes (2019b), HarmonEPS—The HARMONIE Ensemble Prediction System, *Weather and Forecasting*, *34*(6), 1909 – 1937, doi:10.1175/WAF-D-19-0030.1. 41

Grossman, R. L., and A. K. Betts (1990), Air–Sea Interaction during an Extreme Cold Air Outbreak from the Eastern Coast of the United States, *Monthly Weather Review*, *118*(2), 324–342, doi:10.1175/1520-0493(1990)118<0324:AIDAEC>2.0.CO;2. 5

Haiden, T., I. Sandu, B. Gianpaolo, A. Gabriele, and B. Anton (2018), Addressing biases in near-surface forecasts, *ECMWF Newsletter*, (157), 20–25, doi:https://doi.org/10.1002/jame.20013. 6

Hartmann, J., C. Kottmeier, and S. Raasch (1997), Roll Vortices and Boundary-Layer Development during a Cold Air Outbreak, *Boundary-Layer Meteorology*, *84*(1), 45–65, doi:10.1023/A:1000392931768. 5

Haynes, P. H., and M. E. McIntyre (1987), On the evolution of vorticity and potential vorticity in the presence of diabatic heating and frictional or other forces, *J. Atmos. Sci.*, *44*, 828–841. 21

Holtslag, A. A. M., G. Svensson, P. Baas, S. Basu, B. Beare, A. C. M. Beljaars, F. C. Bosveld, J. Cuxart, J. Lindvall, G. J. Steeneveld, M. Tjernström, and B. J. H. V. D. Wiel (2013), Stable Atmospheric Boundary Layers and Diurnal Cycles: Challenges for

Weather and Climate Models, *Bulletin of the American Meteorological Society*, *94*(11), 1691 – 1706, doi:10.1175/BAMS-D-11-00187.1. 5, 6, 38

Homleid, M. (2022), Improving model performance in stable situations by using a pragmatic shift in the drag calculations - XRISHIFT, *ACCORD Newsletter 2*, pp. 96–108. 15

Honnert, R., V. Masson, and F. Couvreux (2011), A diagnostic for evaluating the representation of turbulence in atmospheric models at the kilometric scale, *Journal of the Atmospheric Sciences*, *68*(12), 3112–3131, doi:10.1175/JAS-D-11-061.1. 6, 40

Honnert, R., G. A. Efstathiou, R. J. Beare, J. Ito, A. Lock, R. Neggers, R. S. Plant, H. H. Shin, L. Tomassini, and B. Zhou (2020), The atmospheric boundary layer and the "gray zone" of turbulence: A critical review, *Journal of Geophysical Research: Atmospheres*, *125*(13), e2019JD030,317, doi:https://doi.org/10.1029/2019JD030317, e2019JD030317 10.1029/2019JD030317. 40

Hoskins, B. J., M. E. McIntyre, and A. W. Robertson (1985), On the use and significance of isentropic potential vorticity maps, *Quarterly Journal of the Royal Meteorological Society*, *111*(470), 877–946, doi:https://doi.org/10.1002/qj.49711147002. 21

Joos, H., and H. Wernli (2012), Influence of microphysical processes on the potential vorticity development in a warm conveyor belt: a case-study with the limited-area model COSMO, *Quarterly Journal of the Royal Meteorological Society*, *138*(663), 407–418, doi:10.1002/qj.934. 21

Jung, T., N. D. Gordon, P. Bauer, D. H. Bromwich, M. Chevallier, J. J. Day, J. Dawson, F. Doblas-Reyes, C. Fairall, H. F. Goessling, M. Holland, J. Inoue, T. Iversen, S. Klebe, P. Lemke, M. Losch, A. Makshtas, B. Mills, P. Nurmi, D. Perovich, P. Reid, I. A. Renfrew, G. Smith, G. Svensson, M. Tolstykh, and Q. Yang (2016), Advancing Polar Prediction Capabilities on Daily to Seasonal Time Scales, *Bulletin of the American Meteorological Society*, *97*(9), 1631 – 1647, doi:10.1175/BAMS-D-14-00246.1. 1, 7

Kanamitsu, M., and L. DeHaan (2011), The Added Value Index: A new metric to quantify the added value of regional models, *Journal of Geophysical Research: Atmospheres*, *116*(D11), doi:https://doi.org/10.1029/2011JD015597. 38

Karlsdottir, A., C. Pellegatta, E. Toropushina, J. Riseth, K. G. Hansen, L. C. Hamilton, L. Huskey, L. Zahlkind, N. Loukacheva, P. Nielsen, R. Rasmussen, and S. Johansen (2011), Nordic arctic strategies and implications for regional development, *MEGATRENDS NORDREGIO Report*, doi:10.6027/TN2011-527. 1

Kim, J.-E., Z. Chidong, G. N. Kiladis, and P. Bechtold (2018), Heating and Moistening of the MJO during DYNAMO in ECMWF Reforecasts, *Journal of the Atmospheric Sciences*, *75*(5), 1429–1452. 21, 38

Klein, S. A., and D. L. Hartmann (1993), The Seasonal Cycle of Low Stratiform Clouds, *Journal of Climate*, *6*(8), 1587–1606, doi:10.1175/1520-0442(1993)006<1587:TSCOLS>2.0.CO;2. 30

Kolstad, E. (2011), A global climatology of favourable conditions for polar lows, *Quarterly Journal of the Royal Meteorological Society*, *137*, 1749 – 1761, doi:10.1002/qj.888. 5

Køltzow, M., B. Casati, E. Bazile, T. Haiden, and T. Valkonen (2019), A NWP model inter-comparison of surface weather parameters in the European Arctic during the Year of Polar Prediction Special Observing Period Northern Hemisphere 1, *Weather and Forecasting*, *0*(0), null, doi:10.1175/WAF-D-19-0003.1. 6, 38

Lac, C., S. Maladrel, and J. Pinty (2008), Microphysics in AROME (presentation, March 2008). 12

Lackmann, G. M., and G. Thompson (2019), Hydrometeor Lofting and Mesoscale Snowbands, *Monthly Weather Review*, *147*(11), 3879 – 3899, doi:10.1175/MWR-D-19-0036.1. 2

Le Moigne, P. (2009), SURFEX scientific documentation, *CNRM Tech. Rep.*, p. 211 pp. 12, 14

Lenderink, G., and A. A. M. Holtslag (2004), An updated length-scale formulation for turbulent mixing in clear and cloudy boundary layers, *Quarterly Journal of the Royal Meteorological Society*, *130*(604), 3405–3427, doi:10.1256/qj.03.117. 16, 17

Lorenz, E. N. (1963), Deterministic nonperiodic flow, *Journal of Atmospheric Sciences*, *20*(2), 130 – 141, doi:10.1175/1520-0469(1963)020<0130:DNF>2.0.CO;2. 1

Louis, J.-F. (1979), A parametric model of vertical eddy fluxes in the atmosphere, *Boundary-Layer Meteorology*, *17*(2), 187–202, doi:10.1007/BF00117978. 15

Mahrt, L. (2014), Stably Stratified Atmospheric Boundary Layers, *Annual Review of Fluid Mechanics*, *46*(1), 23–45, doi:10.1146/annurev-fluid-010313-141354. 7

Mang, A., and G. Biros (2016), A Semi-Lagrangian Two-Level Preconditioned Newton–Krylov Solver for Constrained Diffeomorphic Image Registration, *SIAM Journal on Scientific Computing*, *39*, doi:10.1137/16M1070475. 11

Mauritsen, T. (2007), On the Arctic Boundary Layer: From Turbulence to Climate, (PHD Dissertation, Meteorologiska Institutionen (MISU)), Available from: http://urn.kb.se/resolve?urn=urn:nbn:se:su:diva-6585. 4

Mauritsen, T., B. Stevens, E. Roeckner, T. Crueger, M. Esch, M. Giorgetta, H. Haak, J. Jungclaus, D. Klocke, D. Matei, U. Mikolajewicz, D. Notz, R. Pincus, H. Schmidt, and L. Tomassini (2012), Tuning the climate of a global model, *Journal of Advances in Modeling Earth Systems*, *4*(3), doi:https://doi.org/10.1029/2012MS000154. 1

McNider, R. T., D. E. England, M. J. Friedman, and X. Shi (1995), Predictability of the stable atmospheric boundary layer, *Journal of Atmospheric Sciences*, *52*(10), 1602 – 1614, doi:10.1175/1520-0469(1995)052<1602:POTSAB>2.0.CO;2. 6, 31

Mlawer, E. J., S. J. Taubman, P. D. Brown, M. J. Iacono, and S. A. Clough (1997), Radiative transfer for inhomogeneous atmospheres: RRTM, a validated correlated-k model for the longwave, *J. Geophys. Res.: Atmospheres*, *102*(D14), 16,663–16,682, doi:10.1029/97JD00237. 12

Morrison, H., G. de Boer, G. Feingold, J. Harrington, M. D. Shupe, and K. Sulia (2012), Resilience of persistent Arctic mixed-phase clouds, *Nature Geoscience*, *5*(1), 11–17, doi:10.1038/ngeo1332. 5

Müller, M., Y. Batrak, J. Kristiansen, M. Køltzow, G. Noer, and A. Korosov (2017), Characteristics of a Convective-Scale Weather Forecasting System for the European Arctic, *Mon. Wea. Rev.*, *145*(12), 4771–4787, doi:10.1175/MWR-D-17-0194.1. 9, 11

Météo-France (2019), *Diagnostics in Horizontal Domains (DDH) - Variables and budget equations, in horizontal mean ARPEGE, ALADIN and AROME models*, Specific Documentation, Météo-France. 31

Neggers, R., M. Köhler, and A. Beljaars (2007), A dual mass flux framework for boundary layer convection. Part I: Transport, *ECMWF-ARM Report Series*, (2), 25. 18

Niemelä, S., and C. Fortelius (2005), Applicability of Large-Scale Convection and Condensation Parameterization to Meso-y-Scale HIRLAM: A Case Study of a Convective Event, *Monthly Weather Review*, *133*(8), 2422–2435, doi:10.1175/MWR2981.1. 7, 21, 38, 40

Noilhan, J., and S. Planton (1989), A Simple Parameterization of Land Surface Processes for Meteorological Models, *Monthly Weather Review*, *117*(3), 536 – 549, doi:10.1175/1520-0493(1989)117<0536:ASPOLS>2.0.CO;2. 14

Ollinaho, P., S.-J. Lock, M. Leutbecher, P. Bechtold, A. Beljaars, A. Bozzo, R. M. Forbes, T. Haiden, R. J. Hogan, and I. Sandu (2017), Towards process-level representation of model uncertainties: stochastically perturbed parametrizations in the ECMWF ensemble, *Quarterly Journal of the Royal Meteorological Society*, *143*(702), 408–422, doi:https://doi.org/10.1002/qj.2931. 41

Palmer, T., G. Shutts, R. Hagedorn, F. Doblas-Reyes, T. Jung, and M. Leutbecher (2005), Representing Model Uncertainty in Weather and Climate Prediction, *Annual Review of Earth and Planetary Sciences*, *33*(1), 163–193, doi:10.1146/annurev.earth.33.092203.122552. 1

Palmer, T. N. (2001), A nonlinear dynamical perspective on model error: A proposal for non-local stochastic-dynamic parametrization in weather and climate prediction models, *Quarterly Journal of the Royal Meteorological Society*, *127*(572), 279–304, doi:10.1002/qj.49712757202. 1

Papritz, L., and S. Pfahl (2016), Importance of Latent Heating in Mesocyclones for the Decay of Cold Air Outbreaks: A Numerical Process Study from the Pacific Sector of the Southern Ocean, *Monthly Weather Review*, *144*(1), 315–336, doi:10.1175/MWR-D-15-0268.1. 5

Papritz, L., and H. Sodemann (2018), Characterizing the Local and Intense Water Cycle during a Cold Air Outbreak in the Nordic Seas, *Monthly Weather Review*, *146*(11), 3567–3588, doi:10.1175/MWR-D-18-0172.1. 5

Richardson, L. F. (1922), Weather prediction by numerical process. cambridge (university press), *Quarterly Journal of the Royal Meteorological Society*, *48*(203), 282–284, doi:10.1002/qj.49704820311. 2

Rodwell, M. J., and T. Jung (2008), Understanding the local and global impacts of model physics changes: an aerosol example, *Quarterly Journal of the Royal Meteorological Society*, *134*(635), 1479–1497, doi:https://doi.org/10.1002/qj.298. 21

Rodwell, M. J., and T. N. Palmer (2007), Using numerical weather prediction to assess climate models, *Quarterly Journal of the Royal Meteorological Society*, *133*(622), 129–146, doi:https://doi.org/10.1002/qj.23. 21

Sakradzija, M., A. Seifert, and A. Dipankar (2016), A stochastic scale-aware parameterization of shallow cumulus convection across the convective gray zone, *Journal of Advances in Modeling Earth Systems*, *8*(2), 786–812, doi:https://doi.org/10.1002/2016MS000634. 40

Samuelsen, E. M., and R. G. Graversen (2019), Weather situation during observed shipicing events off the coast of Northern Norway and the Svalbard archipelago, *Weather and Climate Extremes*, *24*, 100,200, doi:https://doi.org/10.1016/j.wace.2019.100200. 5

Sandu, I., and B. Stevens (2011), On the Factors Modulating the Stratocumulus to Cumulus Transitions, *Journal of the Atmospheric Sciences*, *68*(9), 1865–1881, doi:10.1175/2011JAS3614.1. 5

Sandu, I., A. Beljaars, P. Bechtold, T. Mauritsen, and G. Balsamo (2013), Why is it so difficult to represent stably stratified conditions in numerical weather prediction (NWP) models?, *Journal of Advances in Modeling Earth Systems*, *5*(2), 117–133, doi:https://doi.org/10.1002/jame.20013. 1, 4, 5, 38

Savijärvi, H. (2006), Radiative and turbulent heating rates in the clear-air boundary layer, *Quarterly Journal of the Royal Meteorological Society*, *132*(614), 147–161, doi:https://doi.org/10.1256/qj.05.61. 7, 21, 37

Seity, Y., P. Brousseau, S. Malardel, G. Hello, P. Bénard, F. Bouttier, C. Lac, and V. Masson (2011), The AROME-France Convective-Scale Operational Model, *Mon. Wea. Rev.*, *139*(3), 976–991, doi:10.1175/2010MWR3425.1. 9, 11, 22, 23

Siebesma, A., P. Soares, and J. Teixeira (2007), A Combined Eddy-Diffusivity Mass-Flux Approach for the Convective Boundary Layer, *J. Atmos. Sci.*, *64*(4), 1230–1248, doi:10.1175/JAS3888.1. 16, 18

Soares, P. M. M., P. M. A. Miranda, A. P. Siebesma, and J. Teixeira (2004), An eddy-diffusivity/mass-flux parametrization for dry and shallow cumulus convection, *Quarterly Journal of the Royal Meteorological Society*, *130*(604), 3365–3383, doi:10.1256/qj.03.223. 16

Sodemann, H., and T. Foken (2004), Empirical evaluation of an extended similarity theory for the stably stratified atmospheric surface layer, *Quarterly Journal of the Royal Meteorological Society*, *130*(602), 2665–2671, doi:https://doi.org/10.1256/qj.03.88. 6

Staniforth, A., and J. Côté (1991), Semi-Lagrangian Integration Schemes for Atmospheric Models—A Review, *Monthly Weather Review*, *119*(9), 2206 – 2223, doi:10.1175/1520-0493(1991)119<2206:SLISFA>2.0.CO;2. 10, 11

Steeneveld, G. J., B. J. H. Van De Wiel, and A. A. M. Holtslag (2006), Modelling the Arctic Stable Boundary Layer and its Coupling to the Surface, *Boundary-Layer Meteorology*, *118*(2), 357–378, doi:10.1007/s10546-005-7771-z. 37

Stensrud, D. J. (2007), *Parameterization Schemes: Keys to Understanding Numerical Weather Prediction Models*, Cambridge University Press, doi:10.1017/CBO9780511812590. 1, 3

Stull, R. B. (1988), *An Introduction to Boundary Layer Meteorology*, vol. 13, Springer Science and Business Media. 4, 17

Sun, J., S. P. Burns, A. C. Delany, S. P. Oncley, T. W. Horst, and D. H. Lenschow (2003), Heat Balance in the Nocturnal Boundary Layer during CASES-99, *Journal of Applied Meteorology*, *42*(11), 1649 – 1666, doi:10.1175/1520-0450(2003)042<1649:HBITNB>2.0.CO;2. 40

Svensson, G., and A. A. M. Holtslag (2009), Analysis of Model Results for the Turning of the Wind and Related Momentum Fluxes in the Stable Boundary Layer, *Boundary-Layer Meteorology*, *132*(2), 261–277, doi:10.1007/s10546-009-9395-1. 6

Tomassini, L., P. R. Field, R. Honnert, S. Malardel, R. McTaggart-Cowan, K. Saitou, A. T. Noda, and A. Seifert (2017), The "Grey Zone" cold air outbreak global model intercomparison: A cross evaluation using large-eddy simulations, *Journal of Advances in Modeling Earth Systems*, *9*(1), 39–64, doi:10.1002/2016MS000822. 5, 21, 38, 40

van der Linden, S. J. A., M. T. Kruis, O. K. Hartogensis, A. F. Moene, F. C. Bosveld, and B. J. H. van de Wiel (2022), Heat transfer through grass: A diffusive approach, *Boundary-Layer Meteorology*, doi:10.1007/s10546-022-00708-7. 6

Vercauteren, N., V. Boyko, A. Kaiser, and D. Belušić (2019), Statistical Investigation of Flow Structures in Different Regimes of the Stable Boundary Layer, *Boundary-Layer Meteorology*, *173*(2), 143–164, doi:10.1007/s10546-019-00464-1. 31

Vihma, T., R. Pirazzini, I. Fer, I. A. Renfrew, J. Sedlar, M. Tjernström, C. Lüpkes, T. Nygård, D. Notz, J. Weiss, D. Marsan, B. Cheng, G. Birnbaum, S. Gerland, D. Chechin, and J. C. Gascard (2014), Advances in understanding and parameterization of small-scale physical processes in the marine Arctic climate system: a review, *Atmospheric Chemistry and Physics*, *14*(17), 9403–9450, doi:10.5194/acp-14-9403-2014. 1

Vogelezang, D. H. P., and A. A. M. Holtslag (1996), Evaluation and model impacts of alternative boundary-layer height formulations, *Boundary-Layer Meteorology*, *81*(3), 245–269, doi:10.1007/BF02430331. 6

Váňa, F., P. Bénard, J.-F. Geleyn, A. Simon, and Y. Seity (2008), Semi-lagrangian advection scheme with controlled damping: An alternative to nonlinear horizontal diffusion in a numerical weather prediction model, *Quarterly Journal of the Royal Meteorological Society*, *134*(631), 523–537, doi:https://doi.org/10.1002/qj.220. 11

Welander, P. (1955), Studies on the General Development of Motion in a Two-Dimensional, Ideal Fluid, *Tellus*, *7*(2), 141–156, doi:10.3402/tellusa.v7i2.8797. 11

Williams, K. D., and M. E. Brooks (2008), Initial Tendencies of Cloud Regimes in the Met Office Unified Model, *Journal of Climate*, *21*(4), 833 – 840, doi:10.1175/2007JCLI1900.1. 21

Wu, L., and B. Wang (2000), A Potential Vorticity Tendency Diagnostic Approach for Tropical Cyclone Motion, *Monthly Weather Review*, *128*(6), 1899 – 1911, doi:10.1175/1520-0493(2000)128<1899:APVTDA>2.0.CO;2. 21

Wyngaard, J. C. (2004), Toward Numerical Modeling in the "Terra Incognita", *Journal of the Atmospheric Sciences*, *61*(14), 1816 – 1826, doi:10.1175/1520-0469(2004)061<1816:TNMITT>2.0.CO;2. 40

Zilitinkevich, S. S., T. Elperin, N. Kleeorin, I. Rogachevskii, and I. Esau (2013), A Hierarchy of Energy- and Flux-Budget (EFB) Turbulence Closure Models for Stably-Stratified Geophysical Flows, *Boundary-Layer Meteorology*, *146*(3), 341–373, doi:10.1007/s10546-012-9768-8. 4, 31

Graphic design: Communication Division, UiB / Print: Skipnes Kommunikasjon AS

uib.no

ISBN: 9788230843529 (print)
9788230845776 (PDF)